Bachelor Thesis

Marina Höschele

April 23, 2019

Orbital evolution of the BepiColombo Mercury Planetary Orbiter (MPO) in the gravity field of Mercury

Supervisors:

Prof. Dr.-Ing. Klaus Brieß, TUB

Dr. -Ing. Sebastian Grau, TUB

Dipl.-Ing. Kai Wickhusen, DLR

Chair of Space Technology

Department of Aeronautics and Astronautics

Technische Universität Berlin

Eidesstattliche Erklärung

Hiermit erkläre ich, dass ich die vorliegende Arbeit selbständig und eigenhändig sowie ohne unerlaubte fremde Hilfe und ausschließlich unter Verwendung der aufgeführten Quellen und Hilfsmittel angefertigt habe.

Berlin, den

…….

Unterschrift

Abstract

This bachelor thesis analyses the influence of Mercury's gravity field on the orbit of the Mercury Planetary Orbiter (MPO) which is the part of the European-Japanese mission BepiColombo launched in October 2018. The gravity field of Mercury was determined from radio tracking data of the NASA's spacecraft MESSENGER which was orbiting the planet until 2015. Due to the highly eccentric orbit of MESSENGER, the calculated gravitational harmonic coefficients are afflicted with uncertainties. Therefore, the orbital evolution of MPO is predictable but with some inaccuracy. For this reason, different plausible gravity fields were generated using a Monte Carlo Method. The generation of the random gravity fields was performed using the gravitational coefficients up to degree and order of 100 and their uncertainties, which were determined by MESSENGER. For that, a function, based on Gaussian distribution, was used. This function was implemented in a numerical orbit integrator developed by DLR, Berlin. Furthermore, scale factors 1, 3, 5 and 10 were used for generating the gravity fields.

Before performing the simulations for orbital prediction of MPO, the boundary conditions were determined. The number of the simulations was set to 10,000 per scale factor, the degree and order of the gravity field was limited to 50. The time frame of the mission was set to 2 Earth years, which covers the nominal and the extended mission phases. The distribution of some important harmonic coefficients was checked and the impact of the gravitational and non-gravitational forces affecting the motion of MPO was determined. As expected, the main accelerations are caused by the gravity field of Mercury, followed by the gravity force of the Sun. The third and fourth disturbing forces are the solar radiation pressure and indirect radiation pressure. The smallest perturbations are caused by the remaining solar system bodies.

The simulations of the orbital evolution of MPO were performed using the generated gravity fields of Mercury with the scale factors 1, 3, 5 and 10. The results of the simulations were analyzed and compared with each other. The evolution of the orbit of MPO is expressed in the orbital elements. The analysis is mainly focused on the periherm as the minimal distance to the surface of Mercury is critical for the mission. The results show that the geopotential of Mercury causes an increase in the eccentricity and a decrease in the periherm altitude. The semi-major axis and the inclination have a periodic character but remain almost constant. The longitude of ascending node decreases slowly with periodic fluctuations. The argument of periapsis falls almost linear. The standard deviations, as well as the difference between the minimal and maximal values get larger with a growing scale factor and over time. The values of the elements are still in an acceptable range after the first year. The change in the periherm after 2 years could already be considered as critical in some cases for the scale factor 1 because the periherm falls below critical value of 200 km. Moreover, the likelihood that the periherm is below 200 km after 2 years increases with the rising scale factor. Furthermore, there is a possibility that the satellite collides with the planet in the simulations for the scale factor 5 and 10.

The influence of the harmonic coefficients J_2, J_3 and J_4 on the longitude of ascending node, argument of periapsis and the eccentricity was investigated analytically which allows for an estimation of the effect of these coefficients, assuming the linear tendency.

In addition, the influence of the gravity of the Sun was investigated. The results show that the Sun has positive effect on the evolution of the periherm after 2 years. Taking into account Mercury's gravity field, the gravity of the Sun, radiation pressure and the solar system bodies, the results of the simulations are very similar to the case with the consideration of the geopotential of Mercury and of the Sun. Thus, the orbital evolution of MPO in mainly affected by the gravity of Mercury and the Sun.

Zusammenfassung

Die vorliegende Bachelorarbeit untersucht die Auswirkungen des Schwerefeldes des Merkurs auf die Umlaufbahn des Mercury Planetary Orbiters (MPOs). Der MPO ist Teil der europäisch-japanischen Mission BepiColombo, die im Oktober 2018 startete. Das Schwerefeld von Merkur wurde durch die NASA's Mission MESSENGER vermessen, welche den Merkur bis zum Jahr 2015 umkreiste. Wegen der hoch elliptischen Umlaufbahn von MESSENGER sind die Koeffizienten der Multipolentwicklung des Schwerefeldes mit Fehlern behaftet. Somit ist die Bahnentwicklung des MPOs nicht eindeutig vorhersagbar. Aus diesem Grund wurden verschiedene mögliche Schwerefelder mit einer Monte Carlo Methode erzeugt. Zur Erzeugung der zufälligen Schwerefelder wurden die Koeffizienten des von MESSENGER bestimmten 100x100 Schwerefeldes und deren Unsicherheiten verwendet. Die dafür verwendete normalverteilte Funktion, wurde in einen nummerischen Integrator implementiert, der am DLR Berlin entwickelt und für den durchgeführten Simulationen benutzt wurde. Außerdem wurden Skalierungsfaktoren von 1, 3, 5 und 10 für die Erzeugung der Schwerefelder genutzt.

Vor der Durchführung der Simulationen für die Bahnbestimmung von MPO wurden zuerst die Randbedingungen bestimmt. Die Anzahl an Simulationen wurde auf Grund der Berechnungsdauer auf 10000 festgelegt. Grad und Ordnung des Schwerefeldes wurden ebenfalls auf Grund der Berechnungsdauer und der geringen Relevanz der höheren Terme auf 50 begrenzt. Die Missionsdauer wurde auf 2 Erdenjahre festgelegt, da dieser Zeitraum die nominale und erweiterte Mission abdeckt. Die Verteilung von relevanten Koeffizienten wurde überprüft und der Einfluss von gravitativen sowie nicht gravitativen Kräften bestimmt. Wie erwartet werden die größten Störbeschleunigungen durch das Schwerefeld des Merkurs und durch die Sonne verursacht. Weitere relevante Störbeschleunigungen sind der Sonnenstrahlungsdruck und der indirekte Strahlungsdruck. Die kleinesten Störungen werden durch die Planeten des Sonnensystems verursacht.

Mit den verschiedenen Schwerefeldern konnten dann die Simulationen der Bahnentwicklung durchgeführt und die Auswirkungen der einzelnen Skalierungsfaktoren analysiert und miteinander verglichen werden.

Die Bahnentwicklung wird in dieser Arbeit mit Bahnelementen beschrieben. Der Schwerpunkt der Analyse liegt dabei auf dem Periherm. Die Ergebnisse zeigen, dass das Geopotential von Merkur einen Anstieg der Exzentrizität und somit einen Abfall des Periherms verursacht. Die große Halbachse und die Inklination haben einen periodischen Charakter, bleiben aber nahezu konstant. Die Länge des aufsteigenden Knoten sinkt langsam mit periodischen Oszillationen. Das Argument der Periapsis fällt nahezu linear. Die Standardabweichungen, sowie die Differenz zwischen den maximalen und minimalen Werten werden breiter mit steigendem Skalierungsfaktor und zunehmender Zeit. Die Werte der Bahnelemente liegen nach einem Jahr im Orbit in einem unkritischen Bereich. Nach 2 Jahren fällt das Periherm selbst bei einem Skalierungsfaktor von 1 in einigen Fällen allerdings schon unter den kritischen Wert von 200 km. Dieses Risiko nimmt mit steigendem Skalierungsfaktor zu. Darüber hinaus ist es sogar möglich, dass die Raumsonde mit dem Planeten kollidiert, was in den Simulationen ab Skalierungsfaktor 5 teilweise aufgetreten ist.

Der Einfluss der Koeffizienten J_2, J_3 and J_4 auf die Länge des aufsteigenden Knoten, das Argument der Periapsis und die Exzentrizität wurde analytisch untersucht. Diese Analyse dient nur zur Einschätzung des Effekts der Koeffizienten, ausgehend von einer linearen Tendenz.

Zusätzlich wurde der Einfluss der Gravitation der Sonne untersucht. Die Ergebnisse zeigen, dass die Sonne in allen Fällen einen positiven Effekt auf die Entwicklung des Periherms hat. Darüber hinaus wurde eine Untersuchung über den Einfluss des Strahlungsdrucks sowie die Planeten des

Sonnensystems durchgeführt. Die Ergebnisse zeigen, dass die Umlaufbahnentwicklung des MPOs hauptsächlich vom Schwerefeld des Merkurs und durch die Gravitationskraft der Sonne beeinflusst wird. Der Strahlungsdruck und die Planeten des Sonnensystems haben einen vernachlässigbaren Effekt.

Contents

Abstract 4
Zusammenfassung 5
List of Figures 9
List of Tables 11
1. Introduction 13
2. Mercury 14
3. Missions to Mercury 16
3.1. Mariner 10 16
3.2. MESSENGER 16
3.3. BepiColombo 17
3.4. MPO 18
4. Theoretical background 20
4.1. Unperturbed orbit 20
4.2. Orbit perturbations 21
4.2.1. Geopotential 22
4.2.2. Geopotential coefficients 24
5. Data and methods 25
5.1. Data used to generate random gravity fields 25
5.2. Data for input state vector of MPO 26
5.3. The numerical Integrator 27
5.4. SPICE 28
5.5. Generating random gravity fields 29
6. Determination of boundary conditions for simulations 31
6.1. Number of simulations 31
6.2. Time duration of the simulations 31
6.3. Output time step 31
6.4. Degree and order 32
6.5. Monte Carlo Method 33
6.6. Time duration of the mission of MPO for simulations 34
6.7. Accelerations acting on MPO due to perturbing forces 34
7. Results 37
7.1. Effect of geopotential of Mercury 37
7.1.1. Evolution of the orbital elements of MPO 37
7.1.2. Evolution of the periherm of MPO 37

7.1.3. Evolution of the eccentricity of MPO 41
7.1.4. Evolution of the apoherm of MPO 43
7.1.5. Evolution of the semi-major axis of MPO 45
7.1.6. Evolution of the inclination of MPO 45
7.1.7. Evolution of the argument of periapsis of MPO 46
7.1.8. Evolution of the longitude of ascending node of MPO 48
7.2. Analytical analysis of influence of the harmonic coefficients $J2$, $J3$ and $J4$ 50
7.3. Comparison with additional perturbing forces 51
7.3.1. Gravity of the Sun 51
7.3.2. Radiation pressure and solar system bodies 57
8. Discussion and conclusion 59
8.1. Discussion 59
8.2. Conclusion 59
Table of acronyms 61
Table of symbols 62
References 65
Appendix 68
Appendix 1 – Evolution of the orbital elements *e, r_a, a, i, Ω* and *ω* dependent on degree and order of the gravitational harmonic coefficients 68
Appendix 2 – Box plot for eccentricity of MPO and corresponded table 71
Appendix 3 – Box plot for apoherm of MPO and corresponded table 72
Appendix 4 – Evolution of orbital elements of MPO considering the geopotential of Mercury, additionally gravity force of the Sun and all perturbations 73

List of Figures

Figure 1. Mercury's interior structure 14
Figure 2. MPO in the orbit about Mercury 19
Figure 3. Angular orbital elements of a satellite around the central body 20
Figure 4. The mass element in the geopotential 22
Figure 5. Spherical harmonics 24
Figure 6. An excerpt from the file with data for spherical harmonic model of the gravity field for Mercury 25
Figure 7. A) The covariance matrix for the 100x100 gravity field of Mercury; B) The excerpt from the covariance matrix for the 100x100 gravity field of Mercury 26
Figure 8. Time duration of one simulation dependent on degree and order, mission duration and output time step 31
Figure 9. Evolution of the periherm dependent on the degree and order of gravitational harmonic coefficients considering from the Mercury's centre over 2 years (left); Zooming of Figure 4 (right). . 32
Figure 10. Further zooming of Figure 4 with evolution of periherm of MPO depended on degree and order of gravitational harmonic coefficients considering from the Mercury's centre over 2 years 32
Figure 11. Normal distribution of normalized gravitational coefficient GM, gravitational harmonic coefficients $C20$, $C22$ and $C30$ for the generated gravity fields with scale factor 1 33
Figure 12. The accelerations acting on the orbit of MPO over 2 years 35
Figure 13. The accelerations acting on MPO during the first day in the orbit 36
Figure 14. The evolution of the periherm dependent on the scale factor over 2 years 38
Figure 15. The box plots for the periherm altitude after 1 year and after 2 years 40
Figure 16. The evolution of the eccentricity dependent on the scale factor over 2 years 42
Figure 17. The evolution of the apoherm dependent on the scale factor over 2 years 44
Figure 18. The evolution of the semi-major axis dependent on the scale factor over 2 years 45
Figure 19. The evolution of the inclination dependent on the scale factor over 2 years 46
Figure 20. The evolution of the argument of periapsis dependent on the scale factor over 2 years 47
Figure 21. The evolution of the longitude of the ascending node dependent on the scale factor over 2 years 49
Figure 22. The evolution of the periherm considering the gravity field of Mercury over 2 years (left); The evolution of the periherm considering the gravity field of Mercury and the Sun as a mass point over 2 years (right). 52
Figure 23. The evolution of the eccentricity considering the gravity field of Mercury over 2 years (left); The evolution of the eccentricity considering the gravity field of Mercury and the Sun as mass point over 2 years (right) 53
Figure 24. The evolution of the apoherm considering the gravity field of Mercury over 2 years (left); The evolution of the apoherm considering the gravity field of Mercury and the Sun as mass point over 2 years (right) 54
Figure 25. The evolution of the longitude of ascending node considering gravity field of Mercury over 2 years (left); The evolution of the eccentricity considering the gravity field of Mercury and the Sun as a mass point over 2 years (right) 55
Figure 26. The evolution of the argument of periapsis considering gravity field of Mercury over 2 years (left); The evolution of the eccentricity considering gravity field of Mercury and Sun as a mass point (right) 56
Figure 27. The evolution of the inclination considering gravity field of Mercury over 2 years (left); The evolution of the eccentricity considering the gravity field of Mercury and the Sun as a mass point over 2 years (right) 57

Figure 28. The evolution of the semi-major axis considering gravity field of Mercury over 2 years (left); The evolution of the eccentricity considering the gravity field of Mercury and the Sun as a mass point over 2 years (right) 57
Figure 29. Evolution of the eccentricity dependent on the degree and order of gravitational harmonic coefficients over 2 years 68
Figure 30. Evolution of the apoherm considering from the Mercury's center dependent on the degree and order of gravitational harmonic coefficients over 2 years 69
Figure 31. Evolution of the semi-major dependent on the degree and order of gravitational harmonic coefficients over 2 years 69
Figure 32. Evolution of the inclination dependent on the degree and order of gravitational harmonic coefficients over 2 years 70
Figure 33. Evolution of the longitude of the ascending node dependent on the degree and order of gravitational harmonic coefficients over 2 years 70
Figure 34. Evolution of the argument of periapsis dependent on the degree and order of gravitational harmonic coefficients over 2 years 71
Figure 35. The box plots for the eccentricity after 1 and 2 years 71
Figure 36. The box plots for the apoherm after 1 and 2 years 72
Figure 37. Evolution of the periherm of MPO dependent on the considered perturbing forces 73
Figure 38. Evolution of the eccentricity of MPO dependent on the considered perturbing forces 74
Figure 39. Evolution of the apoherm of MPO dependent on the considered perturbing forces 75
Figure 40. Evolution of the argument of periapsis of MPO dependent on the considered perturbing forces 76
Figure 41. Evolution of the longitude of ascending node dependent on the considered perturbing forces 78
Figure 42. Evolution of the inclination of MPO dependent on the considered perturbing forces 79
Figure 43. Evolution of the semi-major axis of MPO dependent on the considered perturbing force 80

List of Tables

Table 1. Scientific instruments on board of MESSENGER 16
Table 2. The instruments on board of MPO 18
Table 3. The definition of the satellite's Kepler's elements 21
Table 4. Initial orbital elements of MPO in the inertial Mercury equatorial system 27
Table 5. SPICE system components 29
Table 6. Description of the most relevant kernels used in the simulations 29
Table 7. Parameter used by the generating random gravity fields. 30
Table 8. The nominal values and standard deviations for gravitational coefficient GM and harmonic coefficients $C20$, $C22$, $C30$ 34
Table 9. Input data for considering of the accelerations caused by solar pressure radiation 34
Table 10. Input data for considering of the accelerations caused by indirect radiation pressure. 35
Table 11. Nominal values for periherm considering above surface after 1 and 2 years 39
Table 12. Periherm values above surface after 1 year 39
Table 13. Periherm values above surface after 2 years 40
Table 14. The important parameter of the box plot dependent on the scale factor after 1 and 2 years 41
Table 15. Nominal values for eccentricity after 1 and 2 years 42
Table 16. Eccentricity values after 1 year 43
Table 17. Eccentricity values after 2 years 43
Table 18. Nominal values for apoherm after 1 and 2 years 44
Table 19. Apoherm values above surface after 1 year 44
Table 20. Apoherm values above surface after 2 years 44
Table 21. Nominal values for argument of periapsis after 1 and 2 years 47
Table 22. Values for argument of periapsis after 1 year 48
Table 23. Values for argument of periapsis after 2 years 48
Table 24. Nominal values for longitude of ascending node 49
Table 25. Values for longitude of ascending node after 1 year 49
Table 26. Values for longitude of ascending node after 2 years 49
Table 27. Change in argument of periapsis dependent on the scale factor due to $J2$ after 1 year 50
Table 28. Change in eccentricity dependent on the scale factor due to $J3$ after 1 year 51
Table 29. Change in argument of periapsis dependent on the scale factor due to $J3$ after 1 year 51
Table 30. Change in argument of periapsis dependent on the scale factor due to $J4$ after 1 year 51
Table 31. Nominal values for periherm considering the effect of the gravity field of Mercury and the gravity force of the Sun 52
Table 32. Periherm values above surface after 1 year 52
Table 33. Periherm values above surface after 2 years 52
Table 34. Nominal values for eccentricity considering the gravity field of Mercury and the gravity of the Sun 53
Table 35. Eccentricity values after 1 year 53
Table 36. Eccentricity values after 2 years 53
Table 37. Nominal values for apoherm above surface considering the gravity field of Mercury and the gravity of the Sun 54
Table 38. Apoherm values above surface after 1 year 54
Table 39. Apoherm values above surface after 2 years 54
Table 40. Nominal values for longitude of ascending node the gravity field of Mercury and the gravity of the Sun 55

Table 41. Values for the longitude of ascending node after 1 year 55
Table 42. Values for the longitude of ascending node after 2 years..... 55
Table 43. Nominal values for the argument of periapsis considering the gravity field of Mercury and the gravity of the Sun 56
Table 44. Values for the argument of periapsis after 1 year..... 56
Table 45. Values for the argument of periapsis after 2 years 56
Table 46. Description of the simulations..... 57
Table 47. The important parameter of the box plot for the eccentricity dependent on the scale factor after 1 and 2 years..... 72
Table 48. The important parameter of the box plot for the apoherm dependent on the scale factor after 1 and 2 years..... 72
Table 49. Nominal values for periherm considering all perturbations 73
Table 50. Periherm values above surface after 1 year..... 73
Table 51. Periherm values above surface after 2 year..... 74
Table 52. Nominal values for eccentricity considering all perturbations..... 74
Table 53. Eccentricity values after 1 year..... 75
Table 54. Eccentricity values after 2 year..... 75
Table 55. Nominal values for apoherm above surface considering all perturbations 75
Table 56. Apoherm values above surface after 1 year..... 76
Table 57. Apoherm values above surface after 2 year..... 76
Table 58. Nominal values for argument of periapsis considering all perturbations 77
Table 59. Values for argument of periapsis after 1 year..... 77
Table 60. Values for argument of periapsis after 2 year..... 77
Table 61. Nominal values for longitude of ascending node considering all perturbations 77
Table 62. Values for longitude of ascending node after 1 year 77
Table 63. Values for longitude of ascending node after 2 year 77

1. Introduction

Mercury is the innermost and smallest planet in the Solar System which is difficult to explore because it is very close to the Sun. The first mission to Mercury was Mariner 10 by National Aeronautics and Space Administration (NASA). During the three flybys of the planet, 45 per cent of the surface area was mapped and the first measured values for the gravity field as well as for the magnetic field of Mercury were provided.

MESSENGER was the second NASA-Mission that succeeded to research the planet from a high elliptical polar Mercury orbit. MESSENGER was able to carry out global mapping, analysis of the interior structure and of the polar caps, as well as to explore the exosphere and the magnetosphere. Mercury's gravity field was determined from radio tracking data of the three Mercury flybys in 2008 and 2009 and orbital observation between 2011 and 2015. This data serves as foundation for this bachelor thesis.

However, there were questions left to be answered by MESSENGER. Therefore, the European Space Agency (ESA) and the Japan Aerospace Exploration Agency (JAXA) decided to join forces and sent the space mission BepiColombo to Mercury. The Mission started with the Ariane-5 rocket on October 20, 2018. BepiColombo will swing into the Mercury orbit after flybys of Earth, Venus and Mercury in 2025. BepiColombo consists of two spacecrafts: The Mercury Planetary Orbiter (MPO) by ESA, and the Mercury Magnetospheric Orbiter (MMO) by JAXA.

BepiColombo will investigate planet characteristics, the composition and dynamics of the exosphere, the structure and origin of the magnetic field of Mercury. The objectives of MPO are surface mapping and the exploration of the interior composition of the planet. The aim of MMO is to research the magnetic field and its interaction with the Solar wind.

The MPO carries a payload of 11 science instruments, i.a. Laser Altimeter BELA, developed by German Aerospace Center Adlershof (Deusches Zentrum für Luft- and Raumfahrt, abbreviated DLR). A low polar orbit is planned for the MPO, one that will change because of different perturbations. The major orbit perturbations will be caused by the gravitational potential of Mercury. By means of MESSENGER gathering data, a model of the gravity field was determined.

The objective of this bachelor thesis is the investigation of the consequences of the gravity field of Mercury on the orbit of MPO. Since the gravity field wasn't determined accurately, the gravitational harmonic coefficients are afflicted with uncertainties. Therefore, the orbital evolution of MPO is predictable, but with some inaccuracies. Within the framework of this bachelor thesis, different possible gravity fields were generated which lie within the margin of error of the gravity field, obtained by MESSENGER. The possible consequences on the orbital evolution of MPO were defined and analysed using a Monte Carlo Method. The analysis may help improving future predictions made about the evolution of MPO. It could also assist in estimating the possible operating time.

2. Mercury

Mercury is the innermost planet in the solar system which is locked with the Sun in a 3:2 spin-orbit resonance. It means that Mercury rotates on its axis three times during the two revolutions around the Sun [Stark, 2015]. The rotation of Mercury amounts to 58.646 Earth days [Mazarico et al., 2014] with rotational rate of 6.1385° per day [Archinal et al., 2018], whereas one Mercury's year lasts 87.969 Earth days [Mazarico et al, 2014]. As a consequence of the 3:2 spin-orbit resonance, the Mercury day, which is defined as the time between successive sunrises, is twice longer than the Mercury's year [Rothery, 2015]. Such rotational motion can be explained by "the Sun's torque on the asymmetric mass distribution of Mercury" [Stark, 2015]. The planet follows a highly elliptical orbit with the eccentricity of 0.206 [Tresaco et al., 2018]. Therefore, the difference between Mercury's perihelion (the closest point to the Sun) and aphelion (the farthest point) is large. The distance at perihelion accounts for 0.31 AU from the Sun, but at aphelion, it is 0.47 AU [Strom, 1987], the semi-major axis is 56.7 million km [Stark, 2015]. The inclination of the orbit of Mercury amounts to 7° to the ecliptic plane (plane of Earth's orbit), whereas its axial tilt is almost zero and accounts for 2.036+/-0.058 arcminutes [Margot et al., 2017]

Mercury is the smallest terrestrial planet in the solar system which like Venus has no moons. Its mean radius amounts to 2439.36 +/- 0.02 km [Perry et al., 2015] which is a little bigger than the mean radius of the Earth's Moon with 1734.4 km [Williams et al., 2017]. The mass of the planet accounts for $3.30111 +/- 0.00015 \cdot 10^{23}$ kg [Margot et al., 2017]. Mercury's bulk density is anomalously high with 5,429.30 +/- 0.28 kg/m^3 and similar to the Earth's with ρ = 5,514 kg/m^3, although the size of the both planets is different [Margot et al., 2017]. The explanation of the high uncompressed density of the planet lies in a large core almost dominated by iron which "should by alloyed with one or more light elements" [Hauck et al., 2013] such as silicon and sulfur. Mercury interior structure can be represented as a 4-shell model in which there are inner solid core, outer liquid core with the radius of 1,985+/-39 km, mantle and crust [Genova et al, 2018] (see Figure 1).

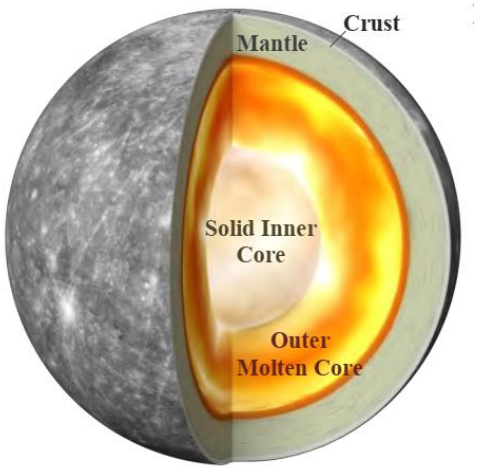

Figure 1. Mercury's interior structure [Genova et al, 2018]

Mercury is heavily cratered planet. The Caloris basin is one of the largest impact basins on Mercury with the diameter of 1,550 km. The planet also demonstrates an effusive volcanism based on extensive lava flows [Rothery, 2015].

Mercury like Earth possesses a large-scale magnetic field [Johnson et al., 2012] with a north-south asymmetry [Rothery, 2015]. The planet presents a dipolar internal field of dynamo origin with the

same polarity as Earth's field [Johnson et al., 2012]. The strength of Mercury's surface magnetic field accounts for about 1 % of the Earth's. The magnetosphere of Mercury is about 8 times smaller than the Earth's because of high solar wind pressure and Mercury's weak dipole moment [Johnson et al., 2012].

Mercury has no atmosphere, but 'surface-bounded' exosphere which contents calcium, sodium, magnesium, potassium, oxygen, hydrogen and helium. Mercury's exosphere is about 10^{13} times smaller than the Earth's atmosphere, while the atmospheric pressure at the Mercury's surface is approximately only 10^{-15} of the Earth's. The temperature on the surface of Mercury varies very strong and is between 100 K on night side and 700 K on the sunward side [Rothery, 2015].

The exploration of Mercury is important for understanding of formation and evolution of other terrestrial planets in our Solar System [Kato et al., 2012], but the investigation of this planet is very challenging. At first, it is difficult to observe the planet telescopically and to photograph it from the Earth due to "Mercury's small size, low reflectivity, and close proximity to the Sun" [Perry et al., 2015]. Secondly, it is hard to orbit the planet by space probe due to gravitational potential of the Sun. Thirdly, the thermal environment, consisting of increased solar radiance and the thermal radiation from the planet, is hostile [Balogh et al., 2007]. For this reason, only two spacecraft visited the planet: Mariner 10, which performed three flybys of Mercury, and MESSENGER which was orbiting the planet between 2011 and 2015 after three flybys of Mercury. The third mission, BepiColombo is on the way to Mercury and will swing into the orbit approximately in 2025.

3. Missions to Mercury

3.1. Mariner 10

The first spacecraft to visit Mercury was Mariner 10 led by NASA. It was launched on November 3, 1973 by an Atlas/Centaur rocket with seven scientific instruments on board. Mariner 10 was the first spacecraft to use gravity-assist for speed reduction and for changing the trajectory without using valuable fuel [Strom, 1987]. It had three flybys around Mercury in March and September 1974 and March 1975 [Rothery, 2015]. During the encounters with the planet, the space probe succeeded in mapping the surface area covered heavily with craters. The obtained data gave new information about the origin of the magnetic field which is "internally generated and similar in form to the Earth's field". [Strom, 1987] The first measurements of the low-degree gravity were also provided. The gravitational coefficient GM and the gravitational harmonic coefficients C_{20} and C_{22} were estimated [Mazarico et al., 2014]. The radius and the mass of Mercury were measured more accurately than "previous Earth-based determinations" [Strom, 1987]. Furthermore, the probe was able to determine that Mercury has no atmosphere but possesses an "exosphere".

Mariner 10 provided important information about the structure, the interior, the gravity field, as well as the magnetic field of Mercury.

3.2. MESSENGER

The NASA's MErcury Surface, Space ENvironment, GEochemistry, and Ranging (MESSENGER) was the first probe to orbit and Mercury launched on August 3, 2004 on a Delta II rocket [Rothery, 2015]. MESSENGER carried a payload of seven instruments and radio science [Solomon et al., 2007] which are listed in Table 1. MLA and RS were the most relevant for the investigation of the planet's interior in that they obtained data, which allowed for a determination of Mercury's gravitational field, rotation and tides [Genova et al., 2018].

Acronym	Description
GRNS	**G**amma-**R**ay and **N**eutron **S**pectrometer
XRS	**X**-**R**ay **S**pectrometer
MDIS	**M**ercury **D**ual **I**maging **S**ystem
MAG	**MAG**netometer
MLA	**M**ercury **L**aser **A**ltimeter
MASCS	**M**ercury **A**tmospheric and **S**urface **C**omposition **S**pectrometer
EPPS	**E**nergetic **P**article and **P**lasma **S**pectrometer
RS	**R**adio **S**cience

Table 1. Scientific instruments on board of MESSENGER [Solomon et al., 2007]

After one Earth flyby in 2005 and two Venus flybys in 2006 and 2007, MESSENGER executed Mercury flyby 1 and in January and October 2008. During both encounters, MESSENGER succeeded in:

- imaging about 90 % of the planet with a 2-km resolution;
- mapping the neutral-atom tails of sodium and calcium;
- discovering tail structure of exospheric magnesium;
- the first laser ranging;
- the observing the internal magnetic field of Mercury under different solar-wind conditions, etc [McNutt et al., 2010].

After the third encounter in 2009, 98 % of the planet was imaged, seasonal changes in exosphere observed and the magnetic field confirmed. “Each flyby passed within 200 km of the surface of Mercury” [Rothery, 2015].

MESSENGER was inserted into orbit about Mercury in March 2011 [Mazarico et al., 2014]. Its initial orbit of 200 km × 15,200 km was highly eccentric with an orbital period of 12.07 hours. It led to that the northern hemisphere was mainly covered, while the southern part was poorly studied [Schuster and Jehn, 2014]. The mission was set to one Earth year and then extended by four Earth years until it ran out of fuel and crashed into the planet in April 2015 [Rothery, 2015].

During the orbiting of Mercury, MESSENGER mapped the landforms and the surface topography of the planet [ESA, 2019a], examined the mineralogy of the surface and content of the exosphere, measured and identified the impact craters, provided evidence of volcanism in Mercury’s past, and discovered the youngest shallows, called “hollows” [ESA, 2019a], [McNutt et al., 2010], [Rothery, 2015]. Furthermore, the spacecraft measured the magnetic field and identified its north-south asymmetry and explored that the magnetosphere of Mercury is remarkably dynamic [Rothery, 2015]. Moreover, the data gathered from the spacecraft helped to determine accurate values for the radius, mass, density, moment of inertia, as well as the thickness and structure of the crust [ESA, 2019a].

Thanks to MESSNGER's radio tracking data, the gravitational coefficient GM and gravitational harmonic coefficients in the degree and order of 100 (see Figure 6), together with their improved uncertainties were estimated [Mazarico, 2018]. The gravitational harmonic coefficients are important for understanding the structure of Mercury’s interior and the long-term evolution of a spacecraft orbit [Mazarico et al., 2014].

3.3. BepiColombo

BepiColombo is the third mission to go to Mercury which started with the Ariane-5 rocket from the European Spaceport in Kourou on October 20, 2018. The BepiColombo mission is a joint project of ESA and JAXA which consists of two spacecrafts: The Mercury Planetary Orbiter (MPO) led by ESA and the Mercury Magnetic Orbiter (MMO) led by the Institute of Space Astronautical Science (ISAS) at JAXA [ESA, 2019b]. MPO and MMO are transported to Mercury by a Mercury Transfer Module (MTM) which provides solar-electric propulsion and all services required en route after separation from the launcher. MTM will be jettisoned shortly before Mercury orbit insertion. The MMO Sunshield and Interface Structure (MOSIF) provides the thermal protection as well as mechanical and electrical interfaces for MMO. The European Space Operations Centre (ESOC) in Darmstadt, Germany, coordinates the mission using the Cebreros 35 m antenna in Spain. After swinging into final orbits, MMO will be operated by the ISAS/JAXA Sagamihara Space Operation Centre while ECOS will continue to coordinate MPO [Rothery, 2015], [ESA, 2019b].

After one Earth flyby, two encounters with Venus and six Mercury flybys, BepiColombo will arrive the planet in December 2025, at which point MMO will be released. MPO will swing into orbit in March 2026. The MMO will have a polar 590 km × 11640 km orbit with a period of about 9.3 hours. The orbit of MMO will coplanar with of MPO’s orbit. During the mission, which was set to one Earth year, with a possible extension by one further Earth year, MPO will image and map Mercury, while MMO will explore the magnetic environment of the planet and its interactions with the solar wind [ESA, 2019e].

Sine there were questions left to be answered by MESSENGER, BepiColombo has the following goals:

- Exploration of the origin and the evolution of Mercury close to the Sun;

- Research of the interior structure and the composition of the planet, inter alia the size and the composition of the core;
- Investigation of the surface geology and the crater history;
- Examination of the composition and the dynamics of the exosphere;
- Exploration of the structure and the dynamics of the magnetosphere and determination of its origin;
- Test of Einstein's theory of general relativity;
- Examination of the composition and the origin of polar deposits;
- Investigation of cosmic environment [ESA, 2019c].

3.4. MPO

As mentioned above, the MPO's main goal is to investigate the surface and the interior of Mercury. In order to achieve the science objectives, MPO has 11 science instruments on board, inter alia the laser altimeter BELA developed by DLR in Adlershof, Berlin. BELA will map the global shape and the topography of Mercury, determine the tidal deformation of the surface, explore the surface roughness and albedo, as well as support the navigation [Lüdicke, 2019], [Rothery, 2015]. The instruments of MPO are summarized in Table 2.

Acronym	Description
BELA	**Be**piColombo **L**aser **A**ltimeter
ISA	**I**talian **S**pring **A**ccelerometer
MPO-MAG	**M**ercury **P**lanetary **O**rbiter **MAG**netometer
MERTIS	**ME**rcury **R**adiometer and **T**hermal **I**nfrared **S**pectrometer
MGNS	**M**ercury **G**amma-ray and **N**eutron **S**pectrometer
MIXS	**M**ercury **I**maging **X**-ray **S**pectrometer
MORE	**M**ercury **O**rbiter **R**adio-science **E**xperiment
PHEBUS	**P**robing of **H**ermean **E**xosphere **b**y **U**ltraviolet **S**pectroscopy
SERENA	**S**earch for **E**xospheric **R**efilling and **E**mitted **N**atural **A**bundance
SIMBIO-SYS	**S**pectrometer and **I**magers for **M**PO **B**epiColombo **I**ntegrated **O**bservatory **SYS**tem
SIXS	**S**olar **I**ntensity **X**-ray and particle **S**pectrometer

Table 2. The instruments on board of MPO [ESA c, 2019]

MPO is a three-axis stabilized and nadir pointing spacecraft whose 'dry mass' accounts for 1,150 kg, whereas its payload weight is 80 kg. The spacecraft is insulated by a heat pipes feeding radiator panel in order to cope with the thermal environment in Mercury orbit [Rothery, 2015]. The three-panel solar array will provide the electrical power of about 1,000 W and there will be a battery capable of similar support for approximately an hour. The telecommunications are performed via two fixed in MPO Low-Gain Antennas, a steerable Medium-Gain Antenna and a steerable High-Gain Antenna. The rate of data transmission will depend on the Earth-Mercury distance and the visibility of ground stations. The downlinked data volume will amount to about 1,550 Gbits per year. The principal Altitude and Orbit Control System comprises Star Trackers, Inertial Measurement Units, Fine Sun sensors, reaction wheal assemblies, sets of 22-Newton hydrazine/MON-3 (Mixed Oxides of Nitrogen) thrusters needed for the change in velocity, as well as 10-Newton monopropellant thruster for altitude control and reaction wheel momentum [ESA, 2019e], [ESA, 2019f], [Rothery, 2019].

Figure 2. MPO in the orbit about Mercury [ESA, 2019g]

MPO will have a polar eccentric 480 km × 1500 km orbit with a period of about 2.3 Earth hours (see Figure 2). This orbit will allow for the study the southern hemisphere from low latitude. The detailed information about the orbit parameter and dimensions of MPO are represented below in Table 4, Table 9 and Table 10.

4. Theoretical background

4.1. Unperturbed orbit

The motion of a spacecraft under the space conditions is fundamentally defined by the gravity. The Newton's gravity law is the source of every calculation for the spacecraft around a central body which can be formulated as:

$$F = -\frac{GMm}{r^2} \tag{1}$$

Here *F* denotes the gravitational force, *G* depicts the universal gravitational constant with $6.6729 \pm 0.00085 \cdot \frac{10^{-11} m^3}{kg \cdot s^2}$, *M* is the mass of the central body, *m* represents the mass of the satellite and *r* is the distance between the centres of mass [Ley et al., 2011]. This inverse-square law describes the gravitation attraction of the central body, in following a planet, which is considered as a point-like mass built up of concentric shell of constant density.

Hence, unperturbed motion of the satellite under the influence of the force F (equation 1) with an assumption, that the total mass of the planet is concentrated in the center of the coordinate system, can be described by the following equation:

$$\ddot{r} = -\frac{GM}{r^3}\boldsymbol{r} \tag{2}$$

Here, the fraction $-\boldsymbol{r}/r$ denotes a unit vector pointing from the satellite to the center of the planet in a non-rotating geocentric coordinate system [Montenbruck and Gill, 2000].

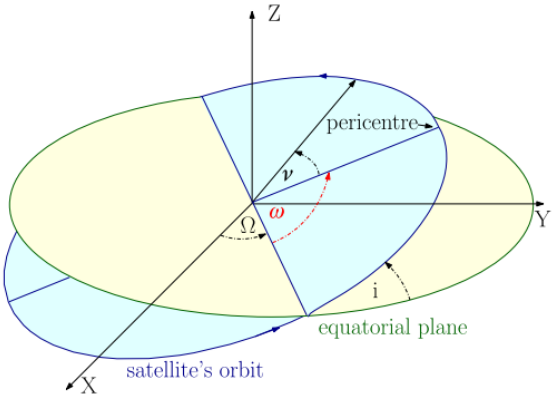

Figure 3. Angular orbital elements of a satellite around the central body [Schuster and Jehn, 2014]

The equation of the satellite motion is described by a sixth-order scalar differential equation which requires six initial conditions in order to determine the six constants of integration. These will be the three components of position (x, y, z) and of velocity (v_x, v_y, v_z). A standard way of specifying an orbit is to use the six orbital elements, so-called Kepler's elements, which define the orbit and position of the body along it in an inertial reference frame [Fortescue et al., 2011]. The first group comprises three elements: inclination *i*, longitude of ascending node *Ω*, and argument of periapsis *ω*, which all three describe the orientation of the orbit with regard to an inertial reference system. Eccentricity *e* and semi-major axis *a* give information about the type and size of the orbit. The last element, mean anomaly *M*, represents the position of the body along the orbit. The angular orbital

elements of the satellite orbit are shown in Figure 3. The definition of the orbital element is summarized in Table 3.

Orbital elements		Definition
Acronym	*Description*	
a	Semi-major axis	The mean value of the maximum and minimum distance of the satellite to the central body.
e	Eccentricity	Determination of the type of the orbit: • Circle when e = 0; • Ellipse when 0 < e < 1; • Parabola when e = 1; • Hyperbola when e > 1.
i	Inclination	Angle of intersection of the equatorial plane and the satellite's orbit.
Ω	Longitude of ascending node	Angle between X-axis and the point on the orbit, at which the satellite crosses the equator from south to north.
ω	Argument of periapsis	Angle between the direction of the ascending node and the direction of the perigee.
M	Mean anomaly	*M* is defined as $M = n \cdot (t - t_p)$ where *n* is mean motion and t_p denotes the time of perigee passage; it changes by 360° during one revolution and increases uniformly with the time [Montenbruck and Gill, 2000].

Table 3. The definition of the satellite's Kepler's elements

4.2. Orbit perturbations

Section 4.1 considers unperturbable Kepler orbit elements with regards to the physics of Newton and Kepler. These elements remain constant over time. The reference frame used by this consideration is an inertial coordinate system, i.e. non-rotating with respect to stars.

Since the realistic distribution of the mass of planets is non-uniform and aspheric, the equation 2 is not valid for the realistic consideration. Furthermore, there are additional perturbing forces which act on the spacecraft, e.g. the gravity forces of additional masses that provide secondary gravitational fields [Fortescue et al., 2011], in case of Mercury orbit, the Sun provides such force.

The equation of motion for the spacecraft around the planet taken into account perturbative influence can be formulated detailed [Damme, 2011]:

$$\ddot{\boldsymbol{r}} = -\frac{GM}{r^3}\boldsymbol{r} + \Sigma\ddot{\boldsymbol{r}}_{PB}(r,t) + \ddot{\boldsymbol{r}}_{Geop}(\boldsymbol{r},t) + \ddot{\boldsymbol{r}}_{RP}(\boldsymbol{r},t) + \ddot{\boldsymbol{r}}_{Atm}(\boldsymbol{r},\dot{\boldsymbol{r}},t) + \ddot{r}_{Tilt}(\boldsymbol{r},t) \qquad (3)$$

The first term shows the gravity acceleration due to the central term of the central body, the second term summarizes the acceleration caused by the gravity forces of other bodies considering as a point-like mass. The third term describes the perturbations due to the higher term of the gravity field of the planet, about which the spacecraft orbits. The fourth term represents the influence of the radiation pressure which comprises the solar radiation pressure, the thermal radiation pressure and the albedo of the planet. The fifth term denotes the acceleration because of the atmospheric drags. The sixth term encompasses the effect of the tidal forces on the orbit evolution of the spacecraft. Moreover, the motion of the space probe may be also affected by the action of an onboard thruster system. Furthermore, relativistic effects should be taken into account by the prediction of orbital evolution of the satellite [Montenbruck and Gill, 2000].

4.2.1. Geopotential

The force induced by the gravity field of the planet can be expressed as the gradient of a certain potential U. It is written in terms of the position vector *r* of the spacecraft with regards to the central planet [Tresaco et al., 2018]:

$$\ddot{r} = \nabla U \tag{4}$$

with

$$U = \frac{GM}{r} \tag{5}$$

The potential can be expressed by an arbitrary mass distribution which comprises the sum of the contributions created by individual mass element $dm = \rho(s)\, d^3 s$ according to

$$U = G \int \frac{\rho(s)\, d^3 s}{|r - s|} \tag{6}$$

Here *ρ(s)* denotes the density at some point ***s*** inside the planet and $|r\text{-}s|$ is the spacecraft's distance from this place (see Figure 4).

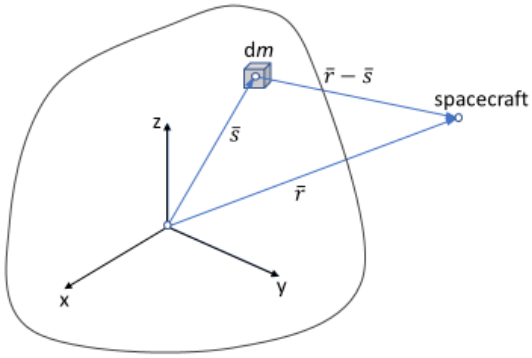

Figure 4. The mass element in the geopotential (adapted from [Montenbruck and Gill, 2000])

The inverse of the distance can be expanded in series of Legendre polynomials:

$$\frac{1}{|r - s|} = \frac{1}{r} \sum_{n=0}^{\infty} \left(\frac{s}{r}\right)^n P_n(cos\gamma) \tag{7}$$

with $r > s$ *and* $cos\,\gamma = \frac{r \cdot s}{rs}$, where $P_n(u)$ is the Legendre polynomial of degree n and γ denotes the angle between ***r*** and ***s***. The Legendre polynomial is defined as:

$$P_n(u) = \frac{1}{2^n n!} \frac{d^n}{du^n} (u^2 - 1)^n \tag{8}$$

For this consideration, the geographic longitude λ, which is counted positively towards the East, and the geographic latitude ϕ for the position of the spacecraft *r*, as well as λ' and ϕ' for the position of the mass element *s* will be introduced. The vectors $\bar{r}$ and $\bar{s}$ are expressed by:

$$\bar{r} = \begin{pmatrix} x \\ y \\ z \end{pmatrix} = \begin{pmatrix} r cos\phi \cos\lambda \\ r cos\phi \sin\lambda \\ r sin\phi \end{pmatrix} \tag{9}$$

$$\bar{s} = \begin{pmatrix} x' \\ y' \\ z' \end{pmatrix} = \begin{pmatrix} s cos\phi' \cos\lambda' \\ s cos\phi' \sin\lambda' \\ s \sin\phi' \end{pmatrix} \tag{10}$$

Using the addition theorem of Legendre polynomials, the Legendre polynomial can be expressed as:

$$P_n(cos\,\gamma) = \sum_{m=0}^{n} (2-\delta_{0m}) \frac{(n-m)!}{(n+m)!} P_{nm}(sin\,\phi) P_{nm}(sin\,\phi') cos(m(\lambda-\lambda')) \quad (11)$$

Here P_{nm} is the associated Legendre polynomial of degree n and order m, which is defined as [Montenbruck and Gill, 2000]:

$$P_{nm}(u) = (1-u^2)^{\frac{m}{2}} \frac{d^m}{du^m} P_n(u) \quad (12)$$

The symbol δ_{0m} represents the Kronecker delta which is equal 1 for *m = 0* and 0 for *m ≠ 0* [Kaula, 2000].

Using equation 11, the gravity potential of the planet can be described by the following formula:

$$U = \frac{GM}{r} \sum_{n=0}^{\infty} \sum_{m=0}^{n} \frac{R^n}{r^n} P_{nm}(sin\phi)(C_{nm}\,cos(m\lambda) + S_{nm}\,sin(m\lambda)) \quad (13)$$

Here R denotes the average radius of the planet, C_{nm} and S_{nm} are the geopotential harmonic coefficients which describe the dependency on the planet's internal mass distribution. These coefficients are defined as:

$$C_{nm} = \frac{2-\delta_{0m}}{M} \frac{(n-m)!}{(n+m)!} \int \frac{s^n}{R^n} P_{nm}(sin\,\phi')\,cos(m\,\lambda')\,\rho(s)\,d^3s \quad (14)$$

$$S_{nm} = \frac{2-\delta_{0m}}{M} \frac{(n-m)!}{(n+m)!} \int \frac{s^n}{R^n} P_{nm}(sin\,\phi')\,sin(m\,\lambda')\,\rho(s)\,d^3s \quad (15)$$

In order to make the harmonic coefficients more readable [Kaula, 2000], they are normally used in a normalized form:

$$\bar{C}_{nm} = \sqrt{\frac{(n+m)!}{(2-\delta_{0m})(2\cdot n+1)(n-m)!}}\, C_{nm} \quad (16)$$

$$\bar{S}_{nm} = \sqrt{\frac{(n+m)!}{(2-\delta_{0m})(2\cdot n+1)(n-m)!}}\, S_{nm} \quad (17)$$

The acceleration due to the gravity potential of the planet, using the normalized harmonic coefficients, can be rewritten as:

$$\ddot{r} = \nabla \frac{GM}{r} \sum_{n=0}^{\infty} \sum_{m=0}^{n} \frac{R^n}{r^n} \bar{P}_{nm}(sin\phi)(\bar{C}_{nm}\,cos(m\lambda) + \bar{S}_{nm}\,sin(m\lambda)) \quad (18)$$

where $\bar{P}_{nm}$ are the normalized associated Legendre functions, which are defined as [Montenbruck and Gill, 2000]:

$$\bar{P}_{nm} = \sqrt{\frac{(2-\delta_{0m})(2\cdot n+1)(n-m)!}{(n+m)!}}\, P_{nm} \quad (19)$$

As it can be seen in equation 13, the gravity potential depends on the universal gravitational constant *G*, the planet's mass *M* and radius *r* and harmonic coefficients C_{nm} and S_{nm}.

4.2.2. Geopotential coefficients

The gravitational harmonic coefficients C_{nm} and S_{nm} with *m = 0* are called zonal coefficients and independent of the longitude [Tresaco et al., 2018]. The coefficients C_{n0} are usually expressed by J_n with J_n= - C_{n0}. All S_{n0} vanish because of their definition [Montenbruck and Gill, 2000]. The even zonal coefficients are symmetric about the equator while the odd zonal coefficients are antisymmetric about the equator and describe the pear-shape asymmetry of the planet [Tresaco et al., 2018]. The geopotential coefficients with *m < n* are called tesseral coefficients and with *m = n* sectorial coefficients [Montenbruck and Gill, 2000]. They depend on longitude [Tresaco et al., 2018].

Furthermore, the harmonic coefficient C_{00} is always equal to 1, so the first term in the expansion of the planet's potential represents the potential reduced to that of a point-like mass [Montenbruck and Gill, 2000].

Moreover, the coefficient C_{22}, which describes the equatorial flattening of the planet [Verma and Margot, 2016], plays a key role in the gravity field of Mercury. The coefficients J_2 and J_3 show the non-sphericity of Mercury [Tresaco et al., 2018]. In particular, J_2 represents the oblateness of the planet while J_3 encompasses the North-South mass asymmetry (pear-shape) of Mercury [Khan and Rocchi, 2018]. Some types of the spherical harmonics are presented in Figure 5.

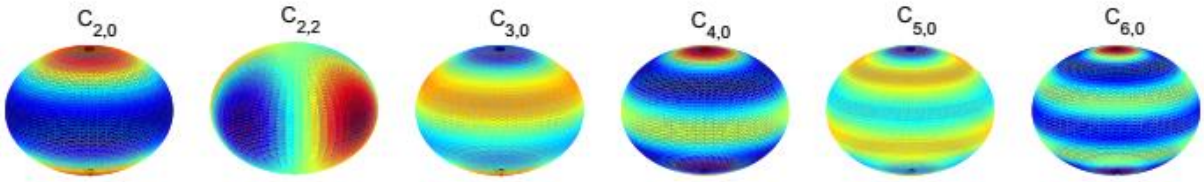

Figure 5. Spherical harmonics [Tresaco et al., 2018]

5. Data and methods

5.1. Data used to generate random gravity fields

Generating random gravity fields was performed using the updated and extended 100×100 gravity field determined by Erwan Mazarico and his team at NASA GSFC (Goddard Space Flight Center) on June 18, 2018 and released by the Geosciences Node of NASA's Planetary Data System (PDS). The gravity field data is based on 7 years of the MESSENGER radio tracking data obtained from the three Mercury flybys in 2008 and 2009 [Mazarico et al., 2014] and orbital observation between March 2011 and April 2015. For the calculation of the gravity field, a Kaula rule[1] of $\frac{3.0 \cdot 10^{-5}}{L^2}$ was applied, where L is degree of the gravity field. The file with data is represented in binary form and consists of four binary tables: a *header table* with descriptive information about the spherical harmonic coefficients, a *names table* with the names of the coefficients, a *coefficients table with* coefficient values and a *covariance table* with the covariance values for the spherical harmonic model coefficients [Mazarico, 2018].
The file with the gravity field for Mercury was obtained from the binary file by DLR and has a form represented in Figure 6. It consists of a header containing additional information and a list of data with spherical harmonic coefficients.
The header has eight units:

- Reference radius of Mercury r_M in km, proceeding from sphericity of the planet;
- Gravitational coefficient GM of Mercury in $\frac{km^3}{s^2}$ for a gravity field model;
- Uncertainty in gravitational coefficient GM in $\frac{km^3}{s^2}$ for a gravity field model;
- Degree of the gravity field;
- Order of the gravity field;
- Normalization state that shows whether the harmonic coefficients are normalized or not:
    - 0 if coefficients are not normalized;
    - 1 if coefficients are normalized;
- Reference longitude of the spherical harmonic expansion;
- Reference latitude of the spherical harmonic expansion.

The table of coefficients includes the coefficients for the spherical harmonic model in degree and order of 100. The first and the second columns in this table represent the degree index m and the order index n respectively. The next two columns denote the coefficients C_{nm} and S_{nm}.

```
2439.4, 22031.815411154894, 0.000194, 100, 100, 1, 0.0, 0.0

  0   0   1.0000000000e+00   0.0000000000e+00
  1   0   0.0000000000e+00   0.0000000000e+00
  1   1   0.0000000000e+00   0.0000000000e+00
  2   0  -2.2508016774e-05   0.0000000000e+00
  2   1  -9.0596611472e-10  -3.3180545835e-09
  2   2   1.2461628084e-05   8.4039263385e-09
  3   0  -4.7542281665e-06   0.0000000000e+00
  3   1  -3.5979709938e-06  -2.6539618850e-06
  3   2   9.7183321341e-07  -5.8540636831e-07
  3   3   6.1598023107e-07   1.6582923777e-06
  4   0  -5.8611942789e-06   0.0000000000e+00
  4   1   1.7574028585e-06   3.3595555536e-06
  4   2   1.9023082170e-06   2.8140599780e-06
  4   3  -7.6767475950e-07   1.4175656777e-06
  4   4   1.3277903366e-08  -3.0832632525e-07
```

Figure 6. An excerpt from the file with data for spherical harmonic model of the gravity field for Mercury

[1] If the data needed for the determination of the spherical harmonic gravity field is not globally distributed, like in the case of MESSENGER, the usage of a priori constraint is necessary. For example, in the determination of gravity fields of planets, the "Kaula rule" is "used for a smoothing constraint, whereby each coefficient C_{ln} or S_{ln} is assigned an a priori uncertainty on the basis of its expected variance at degree l" [Mazarico et al., 2014].

Figure 7 A shows the covariance matrix for the gravitational harmonic coefficients up to degree and order 100. It is represented in 10201×10201 matrix. Each cell depicts the covariances between the coefficients beginning with C_{nm} from left to right and from top to bottom and following with S_{nm} from the middle of the square. The diagonal comprises the variances, i.e. squared uncertainties in C_{nm} and S_{nm}. The dark cells denote weak covariances and the light cells represent strong covariances. In order to do the covariances lucidly due to large variation of their values, the matrix was plotted logarithmically on the basis of 10 using absolute values of covariances. It can be seen, that the low-degree zonal coefficients are highly correlated due to the eccentric orbit of MESSENGER [Mazarico et al., 2014].

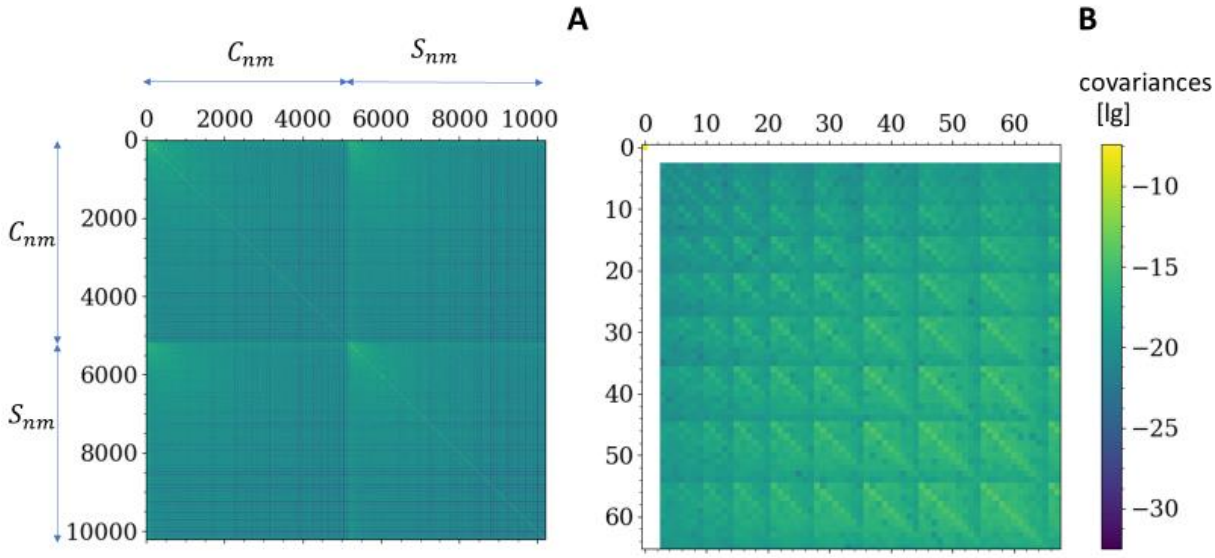

Figure 7. A) The covariance matrix for the 100x100 gravity field of Mercury; B) The excerpt from the covariance matrix for the 100x100 gravity field of Mercury

Figure 7 B presents an excerpt from the covariance matrix for low-degree of C_{nm} (see section 6.4).

5.2. Data for input state vector of MPO

The values for input state vector of MPO and its associated mission start date, used in Integrator for orbit propagation, were taken from the BepiColombo Mercury Cornerstone Consolidated Report on Mission Analysis (CREMA), updated on June 11, 2018. Table 4 lists the elements for target orbit of MPO. Since the information about mean anomaly wasn't available in CREMA, it was set to 0°.

The orbital period of MPO is 2.362 h which means that the satellite will orbit Mercury 10.16 times per Earth day.

The arrival date in the target orbit is given in MJD2000 time epoch. MJD means Modified Julian Date and refers to a time frame, defined as the number of days since 01-01-2000, 12:00 noon UTC. MPO will presumably arrive the orbit on March 14, 2026 at 15:40:19.2 UTC that corresponds to MJD2000 = 9,569.653 and to J2000 = 826,774,888.3855518 respectively.

The data is put in relation to the inertial Mercury equatorial system (MercuryIAU), expressed in J2000 Earth equator system. MercuryIAU is defined as follows:

- z-axis points in direction of the angular momentum of Mercury with coordinates α = 281.0097 ° and δ = 61.4155°, where α and δ denote right ascension and declination respectively [Seidelmann et al., 2007];
- x-axis: intersection between Mercury equator system, meaning orbital plane, and Earth equator system in J2000 [Khan and Rocchi, 2018];
- y-axis: $Z \cdot X$, using right-hand system [Khan and Rocchi, 2018].

Parameter	Value	Unit
Periherm altitude, h_p	480	km
Apoherm altitude, h_a	1500	km
Semi-major axis, *a*	3430	km
Velocity in periherm, v_p	2.944	$\frac{km}{s}$
Velocity in apoherm, v_a	2.182	$\frac{km}{s}$
Orbital period, *T*	2.362	h
Eccentricity, *e*	0.148688	-
Inclination, *i*	90	°
Longitude of ascending node	67.8	°
Argument of periapsis, *ω*	16	°
Mean anomaly, *M*	0	°
Date (MJD2000)	9569.653	*days*

Table 4. Initial orbital elements of MPO in the inertial Mercury equatorial system (adapted from [Khan and Rocchi, 2018])

5.3. The numerical Integrator

The simulations for the orbital evolution of MPO were performed with numerical Integrator developed by DLR Adlershof in Berlin. The Integrator provides the solution for an equation of motion of a satellite and allows to predict the trajectory of the spacecraft orbiting about a central body or during the flybys considering gravitational and as well as non-gravitational perturbing forces. The Integrator is written in program language Fortran 77 and uses the software platform SPICE (see section 5.4) which provided the data sets called kernels with information about e.g. rotation and shape size of natural bodies, ephemerides, leap seconds etc. The Integrator was configured and controlled using a Python interface. Furthermore, the Python modules numpy, scipy and matplotlib were used for the analysis and visualization of the results.

The input state vector in the Integrator can be keyed as state vector in cartesian coordinates (x, y, z, v_x, v_y, v_z) or in orbital elements (*a, e, i, Ω, ω, M*). The state vector comprises the three-dimensional coordinates (x, y, z) given in km and corresponding velocity vector (v_x, v_y, v_z) given in $\frac{km}{s}$. The orbital elements contain semi-major axis *a* [km], eccentricity *e*, inclination *i* [°], the longitude of the ascending node *Ω* [°], argument of periapsis *ω* [°] and mean anomaly *M* [°]. The input state vector can be specified in three different reference frames: J2000, inertial PlanetIAU and body-fixed IAUPlanet. The step size for output has to be specified.

The Integrator allows to include the following disturbing forces acting on the orbit of the spacecraft:

1. Gravity field and higher terms of the geopotential of the central body;
2. Additional perturbing bodies, for example, the Sun, all planets of the Solar system acting as point mass and the geopotential of one additional body;
3. Solar radiation pressure (SRP);
4. Atmospheric drag;

5. Tidal potential;
6. Indirect radiation pressure comprises the thermal radiation pressure and radiation due to bond albedo of the central body.

The file with gravitational coefficient GM and the harmonic coefficients needs to have a specific structure to be readable for the program which was described in (section 5.1). The uncertainties in GM and C_{nm} and S_{nm} are not taking into account by propagation of the trajectory of the spacecraft in the Integrator (see Section 5.5).

Note that the spacecraft is considered as massless body. Only for calculations including atmospheric drag and/or SRP, a spacecraft mass given in kg is assumed. In this case, the surface-to-mass ratio of the satellite is used. The orbiter is modelled as a cuboid consisting of six surfaces s_1, s_2, s_3, s_4, s_5, s_6 and with a solar panel s_7 which is always perpendicular to the Sun. The surface s_4 is always nadir pointing. The area is given in m^2 and its reflectivity of each surface is entered in the input file of the Integrator.

For the simulation, indirect radiation pressure (the thermal radiation and reflected radiation due to the bond albedo), the central body is assumed as a sphere. Therefore, the visible area of the planet for the satellite is assumed as a circle that is divided into k discrete surface segments, so-called concentric rings and one central cap. The rings in turn are divided into surface segments n_i with *i=1,…,k*. Moreover, the parameter $n_a$represents the number of additional surface segments in the outer rings.

The available methods for solving the numerical integration are RK4 (Runge-Kutta method of order four), RKFB (Runge-Kutta-Fehlberg method of order five), dop853 (Runge-Kutta method of order eight), dlsode (Adam multi-step method of order 12 with a double precision) and dop853 with projection. Note that the method dlsode was used for the simulations in this bachelor thesis.

The output file with calculated results is returned either as state vector (x, y, z, v_x, v_y, v_z) or orbital elements (r_p, *e, i, Ω, ω, M*) where r_p encompasses the pericenter altitude from the centre of the body. Furthermore, the output reference frame can be either J2000, planetIAU or IAUplanet. The accelerations due to selected perturbing forces are presented in the output file and can be summarized and returned in a figure.

See [Damme, 2011] and [Bahloul, 2013] for more detailed description of the Integrator.

5.4. SPICE

As mentioned above, the Integrator uses the SPICE information system provided by NAIF (NASA's Navigation and Ancillary Information Facility). SPICE includes data sets called kernels which include information to help scientists and engineers design missions, plan scientific observations, analysis science data and conduct various engineering functions associated with flight projects. [Acton, 2019]

The main eponymous components of the SPICE system are presented in Table 5. In addition, there are also important data products of SPICE not included in the “SPICE” acronym. A frames kernel (FK) comprises “specifications for the assortment of reference frames used by flight projects”. The spacecraft clock (SCLK) and leap second (LSK) are used “in converting time tags between various time measurement systems”. Therefore, a digital shape model kernel (DSK) provides the “higher fidelity shape models” for “small irregularly shaped bodies such as asteroids and comet nuclei” and “large, more uniformly shaped bodies such as Moon, Earth and Mars” [Acton, 2019].

Furthermore, the SPICE system provides also a large collection of software called SPICE Toolkit whose principal component is a library of subroutines “needed to read the kernel files and to then calculate observation geometry parameters of interest to scientists” [Acton, 2019]. The SPICE Toolkit can be integrated by users into their own programs.

S	Spacecraft ephemeris as a function of time (SPK).
P	Planet, satellite, comet, asteroid ephemerides and location of bodies (SPK); certain physical, dynamical and cartographic constants for bodies (PCK).
I	Instrument information about descriptive data to the geometric aspects of a particular scientific instrument, e.g. field-of-view size, shape and orientation parameter (IK).
C	Orientation information with a transformation called the “C-Matrix”, which provides time-tagged pointing (orientation) angles for a spacecraft bus or spacecraft structure (CK)
E	Events information, summarizing mission activities which is contained in the SPICE E-kernel file set comprising three components: Science Plans, Sequences, and Notes (EK)

Table 5. SPICE system components [Acton, 2019]

The most relevant kernels used in the simulations are depicted in Table 6.

Name of kernel	Description of kernel
pck00010.tpc	Orientation and size/shape data for natural bodies;
de432s.bsp	SPK-Kernel providing ephemerides for the planets and satellites;
naif0012.tls	Leap seconds;
gm_de431.tpc	Mass parameter to planets and satellites.

Table 6. Description of the most relevant kernels used in the simulations

5.5. Generating random gravity fields

As described in section 5.3, the Integrator doesn’t take the uncertainties of the gravitational coefficient GM and as well as in gravitational harmonic coefficients C_{nm} and S_{nm} into account. In order to take these uncertainties into account, it was decided to generate random gravity fields on the basis of the 100x100 gravity field with nominal values for GM, C_{nm} and S_{nm} and their associated uncertainties.

In order to check as many variations as possible, it was decided to use the Monte Carlo Method (see section 6.5) and generate random gravity fields which lie within the margin of error of 100X100 gravity field using covariance matrix for uncertainties. These random gravity fields were generated using the function “random multivariate normal” which was implemented in the class Geopotential into the Integrator. This function represents Gaussion distribution as a generalization of the one-dimensional normal distribution to higher dimensions [The SciPy community, 2018]. The distribution is specified by its nominal values for GM, C_{nm} and S_{nm} and covariance matrix. Furthermore, this function has a parameter k depicting the number of generating fields. The option “seed” was used to assure the fixing random state for reproducibility of the gravity fields. Therefore, the parameter scale factor was integrated in this function. The scale factor is usually used “to obtain conservative error estimates for the gravity field coefficients” [Mazarico et al., 2014]. The scale factor was multiplied with the standard deviation σ that was limited to 5 σ to avoid the generating extreme and unrealistic fields.

Note that the generation of GM and coefficients was executed separately, i.e. without correlations between each other.

Table 7 represents the summary of the main parameters used for generating the gravity fields.

Description of parameter	**Value**
Number of generating gravity fields per scale factor	10000
Number of using “seed”	1
Value of chosen “seed”	7
Scale factors	1, 3, 5, 10
Limit for standard deviations	5 σ

Table 7. Parameter used by the generating random gravity fields.

6. Determination of boundary conditions for simulations

Before performing the simulations for orbital prediction of MPO, the boundary conditions were determined which are presented in this section.

6.1. Number of simulations

Since a Monte Carlo Method was decided to use for the simulations, the number of the attempts have to be large enough to allow the statistical consideration. On the other hand, the limited time and resources had to be considered. As a compromise, the number of the simulations was set to 10,000 (see next section).

6.2. Time duration of the simulations

In order to estimate the time needed for the simulations, the orbital evolution was simulated for one gravity field with different degrees and orders, output time steps and mission duration. The degree and order were taken from 0 to 100. The output time step was set to 60 s and 3,600 s. The orbital evolution was simulated over 1 year and 2 years. Figure 8 demonstrates the time duration of one simulation considering different conditions. It can be seen, that the time duration grows exponential with the increasing degree and order, rising mission duration and smaller output time step.

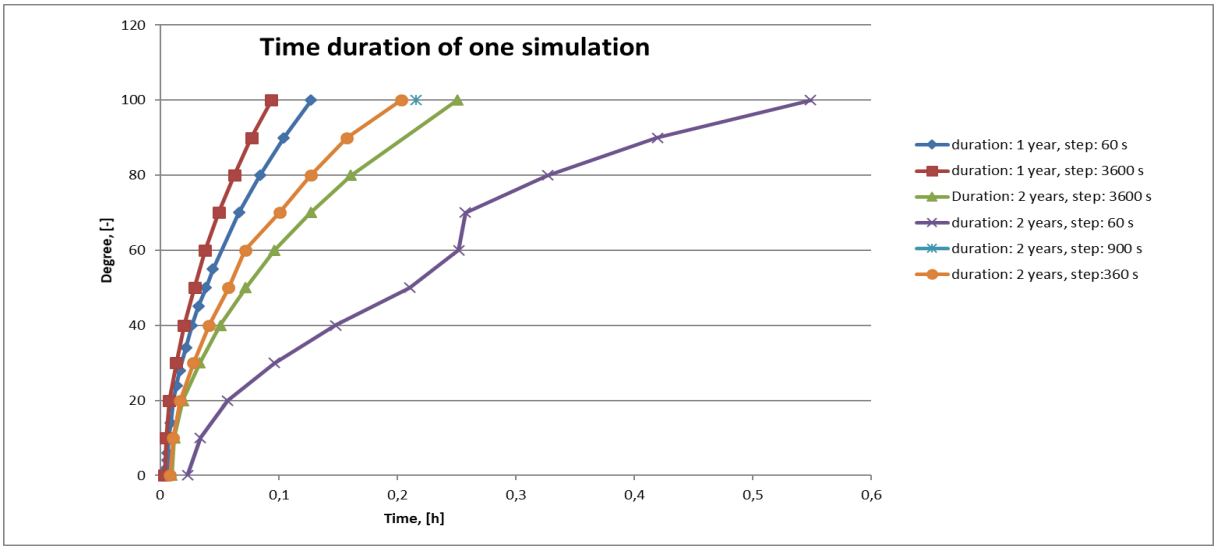

Figure 8. Time duration of one simulation dependent on degree and order, mission duration and output time step.

6.3. Output time step

Since the output time step doesn't affect the quality of the integrated trajectory and the orbital elements don't evolve rapidly, the output time step was set to 10,000 (1.7 h per step) from the reason of data size because to big data size leads to the long processing time.

6.4. Degree and order

In order to analysis the effect of the degree and order on the evolution of orbital elements of MPO and to define the reasonable degree and order in the scope of this bachelor thesis, ten simulations were performed using nominals values of the 100×100 gravity field without considering the uncertainties. The degree and order were varied from 0 to 100 in step of 10.

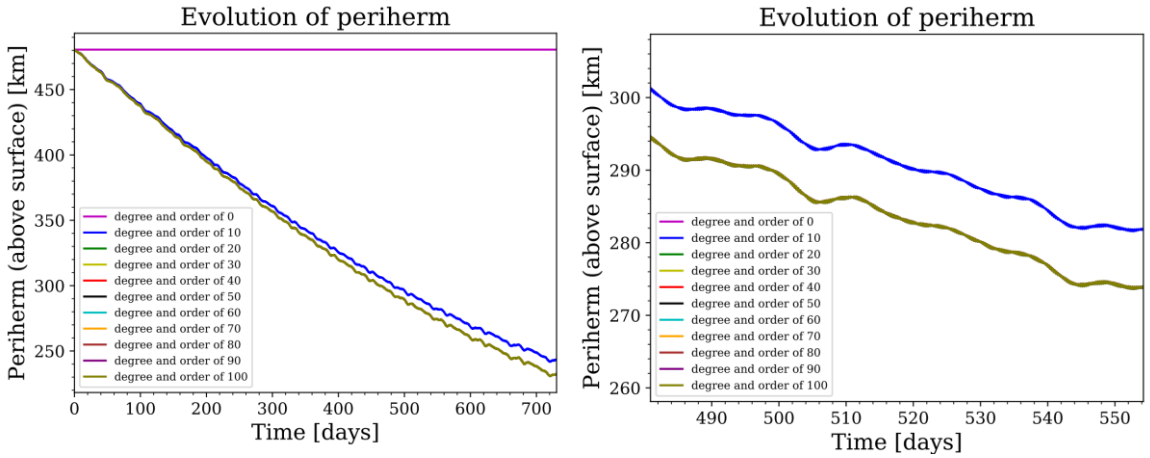

Figure 9. Evolution of the periherm dependent on the degree and order of gravitational harmonic coefficients considering from the Mercury's centre over 2 years (left); Zooming of Figure 4 (right).

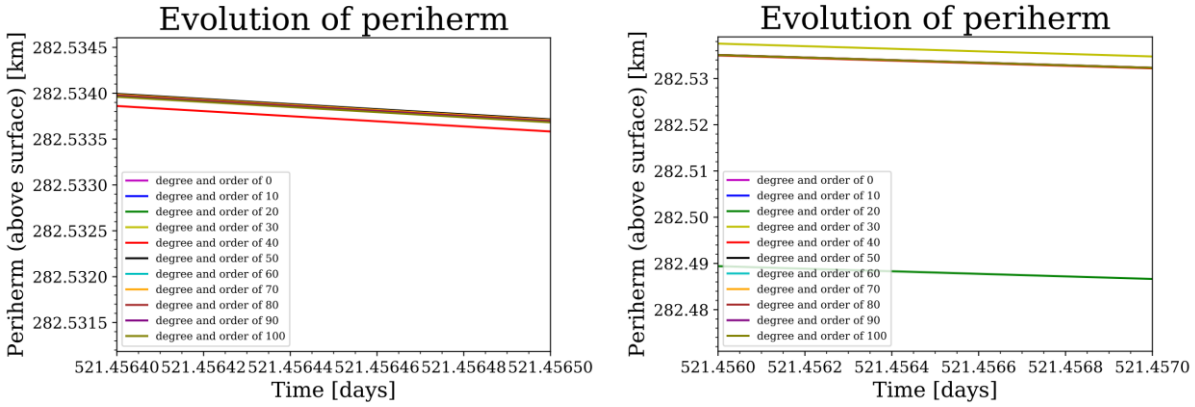

Figure 10. Further zooming of Figure 4 with evolution of periherm of MPO depended on degree and order of gravitational harmonic coefficients considering from the Mercury's centre over 2 years

Figure 9 shows the evolution of periherm of MPO depended on degree and order of gravitational harmonic coefficients considering from the surface of Mercury. The legend of the plot depicts the colour lines corresponding to degree and order from 0 to 100. According to the plot, the periherm doesn't change for degree and order of zero over time because the orbital elements are unperturbable due to considering only the central GM of Mercury. The influence of the degree and order up to 10, which leads to the periherm decrease, is clearly seen. Furthermore, the gravity field in the degree and order up to 20 presenting with the gold line causes stronger decline of the periherm than in the order and degree of 10 depicted as the blue line, the difference is in km and accounts for 5 km after 1 year and 12 km after 2 years.

As demonstrated in Figure 10, the difference between degree and order up to 50 and 40 is in the range of m. The interesting point is, that the gravity field in degree and order of 20 decreases the r_p

more than in degree and order up to 30. Since the change in the periherm by considering the difference between degree and order of 50 and higher is in the range of mm, it was decided to take into consideration the change in the periherm accuracy within m under scope of this bachelor thesis.

The decision about degree and order was made through the example of periherm because it is the most important parameter for considering in the scope of this bachelor thesis. The plots with the evolution of other elements e, r_a, a, i, Ω and ω dependent on degree and order of gravitational harmonic coefficients can be found in Appendix.

In the following, all simulations were performed using the gravity field up to degree and order 50.

6.5. Monte Carlo Method

The generation of gravity fields for the simulations was performed with the Monte Carlo Method, which is based on random selection of parameter values and subsequent evolution of function values. This method was used due to its simple implementation. Note that usage of the Monte Carlo Method requires a large number of simulations. As described in section 6.1, the number of simulations was set to 10,000.

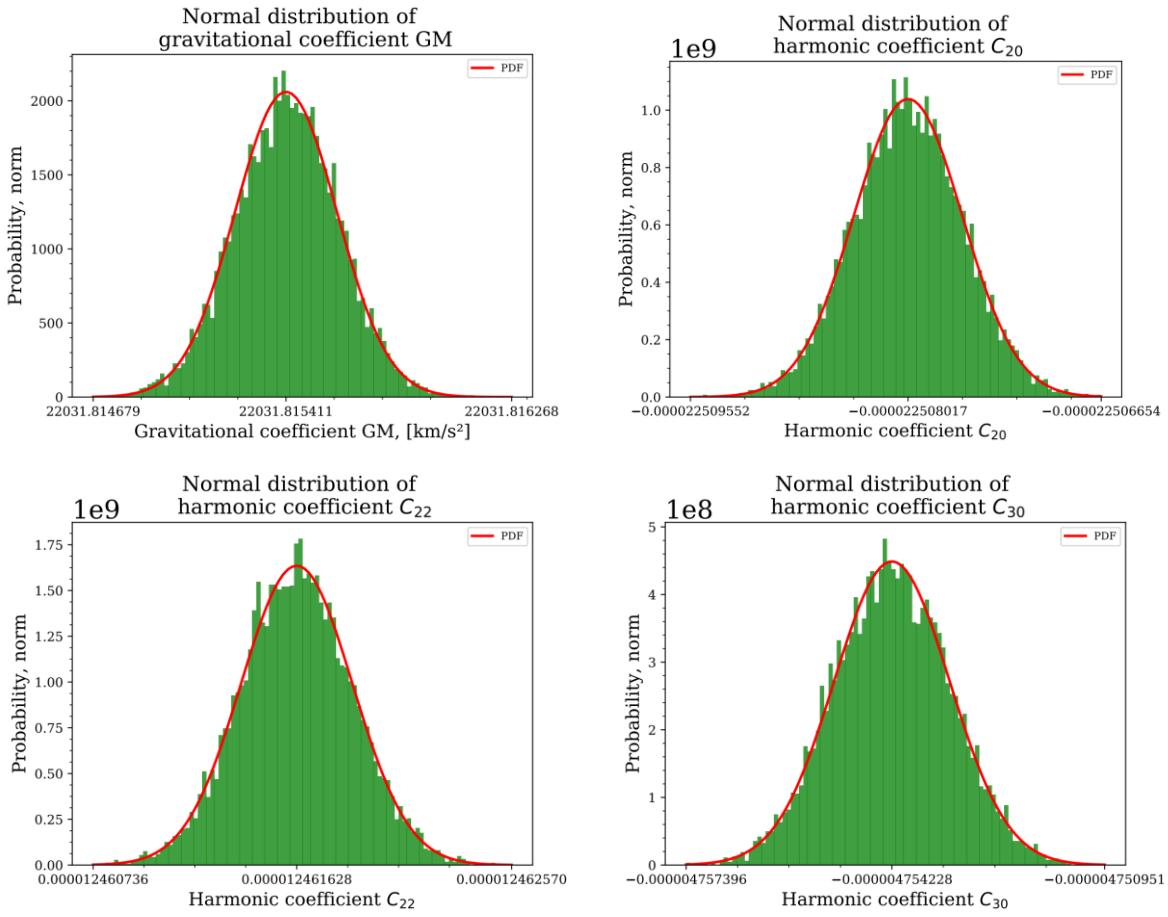

Figure 11. Normal distribution of normalized gravitational coefficient GM, gravitational harmonic coefficients C_{20}, C_{22} and C_{30} for the generated gravity fields with scale factor 1

Although the generating random gravity fields was performed with the function multivariate which is based on the normal distribution, in order to review the consistent filling of the generating harmonic coefficients in the margin of error, the histograms with normal distribution, shown in Figure 11, were

created for the gravitational coefficient GM and gravitational harmonic coefficients C_{20}, C_{22} and C_{30}. These coefficients were selected because they mainly affect the evolution of the orbital elements.

The green bars denote the real normalized distribution of GM and harmonic coefficients, the red line represents probability density which was calculated with the probability density function (PDF) on basis of the nominal value (μ) and standard deviation (σ). The values of μ and σ for GM, C_{20}, C_{22} and C_{30} are represented in Table 8.

According to the plots, GM and the coefficients are generally spread well, the distribution is approximately symmetrical.

Parameter	**μ**	**σ**
GM [$\frac{km^3}{s^2}$]	$2.2031815411154894 \cdot 10^4$	$1.9361909444154922 \cdot 10^{-4}$
C_{20}	$-2.2508016774 \cdot 10^{-5}$	$3.8394711196316993 \cdot 10^{-10}$
C_{22}	$1.2461628084 \cdot 10^{-5}$	$2.4395099417725768 \cdot 10^{-10}$
C_{30}	$-4.7542281665 \cdot 10^{-6}$	$8.8860037567489276 \cdot 10^{-10}$

Table 8. The nominal values and standard deviations for gravitational coefficient GM and harmonic coefficients C_{20}, C_{22}, C_{30}

6.6. Time duration of the mission of MPO for simulations

As mentioned in section 3.3, the primary mission of MPO was set up to one Earth year with additional option of extending it by one Earth year. Therefore, it was decided to predict and analyse the evolution of the orbital elements of MPO in the gravity field of Mercury over 2 Earth years.

6.7. Accelerations acting on MPO due to perturbing forces

In order to estimate the impact of different perturbing forces which affect the trajectory of the orbiter, a simulation was performed using nominal values for the gravity field without considering the uncertainties and taking gravitational as well as non-gravitational effects into account. The additional input data needed for this simulation is listed in Table 9 and Table 10. The output time step was set to 100,000 that correspond to 631.152 s and 0.17532 h per step respectively.

Surface of MPO	**Surface size [m^2]**	**Surface reflectivity**
s_1	2.852	0.8
s_2	4.692	0.8
s_3	2.852	0.8
s_4	4.692	0.8
s_5	4.6375	0.9
s_6	3.9525	0.8
s_7	2.7008	0.21

Table 9. Input data for considering of the accelerations caused by solar pressure radiation [Lüdicke, 2008]

Figure 12 shows the order of the magnitude of accelerations acting on MPO. As expected, the main accelerations are caused by the central term GM of Mercury, followed by higher terms of gravitational potential of Mercury, the gravity force of the Sun considered as a point mass and the solar radiation pressure. The next important perturbing force is indirect radiation pressure which is represented as the sum of thermal radiation pressure and reflected albedo radiation. Both effects are also shown in Figure 7 separately. The smallest perturbations are the gravity forces of Venus, the

Earth-Moon barycentre, Jupiter, Saturn and Mars, which are taken into consideration as a point mass.

Parameter	Value	Units
Mass of MPO	1,150 [ESA, 2018]	kg
Bond albedo of Mercury	0.12 [Kato et al., 2012]	-
Minimal temperature	100 [Rothery, 2015]	K
Number of concentric rings	2	-
Number of elements in the innermost ring	6	-
Addition of ring elements to each ring, starting after innermost ring	6	-

Table 10. Input data for considering of the accelerations caused by indirect radiation pressure.

As it can be seen in Figure 12, the accelerations due to the higher terms of the geopotential of Mercury have a periodic character. These accelerations are caused by the rotation of Mercury on its axis and vary between $6.36 \cdot 10^{-7}\ \frac{km}{s^2}$ and $1.223 \cdot 10^{-9}\ \frac{km}{s^2}$.

Furthermore, the influence of the gravity of the Sun is associated with the proximity of Mercury to the Sun. The accelerations caused by the Sun are in the range of $1.108 \cdot 10^{-8}\ \frac{km}{s^2}$ in perihelion and $1.115 \cdot 10^{-9}\ \frac{km}{s^2}$ in aphelion. The solar radiation pressure and indirect radiation pressure depend also on the position of Mercury relative to the Sun. When Mercury is located in the pericenter, the solar radiation and corresponding accelerations are stronger. The maximal value for SRP is $4.923 \cdot 10^{-10}\ \frac{km}{s^2}$, for indirect RP amounts to $3.413 \cdot 10^{-11}\ \frac{km}{s^2}$. The minimal value for SPR and albedo is $0\ \frac{km}{s^2}$ when the satellite is over the dark hemisphere of Mercury whereas the accelerations due to the thermal radiation accounts for $4.173 \cdot 10^{-15}\ \frac{km}{s^2}$.

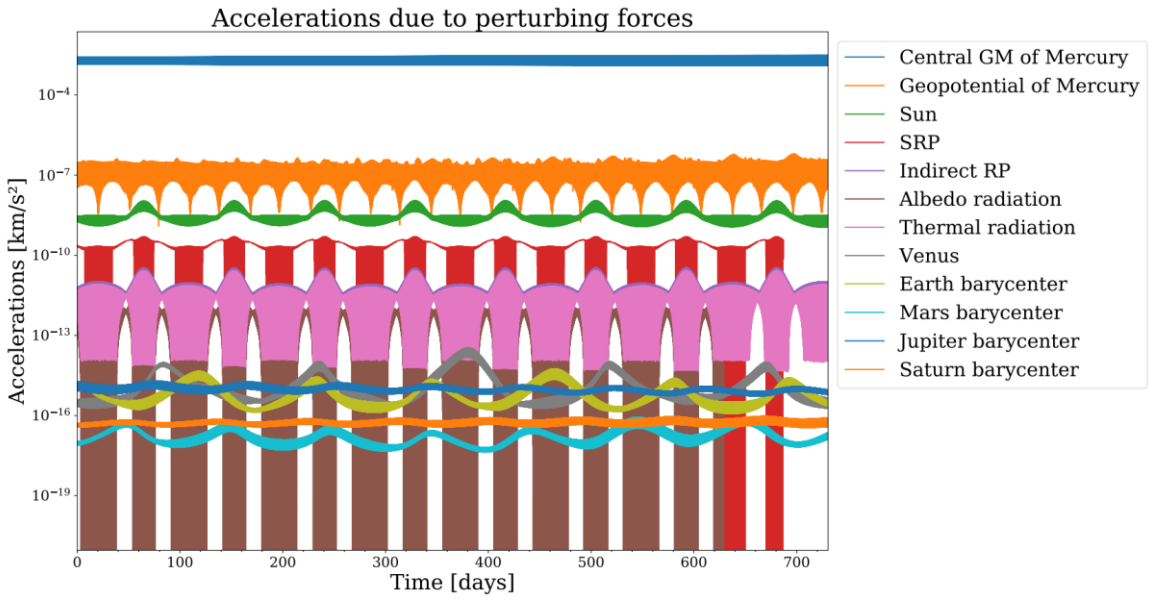

Figure 12. The accelerations acting on the orbit of MPO over 2 years

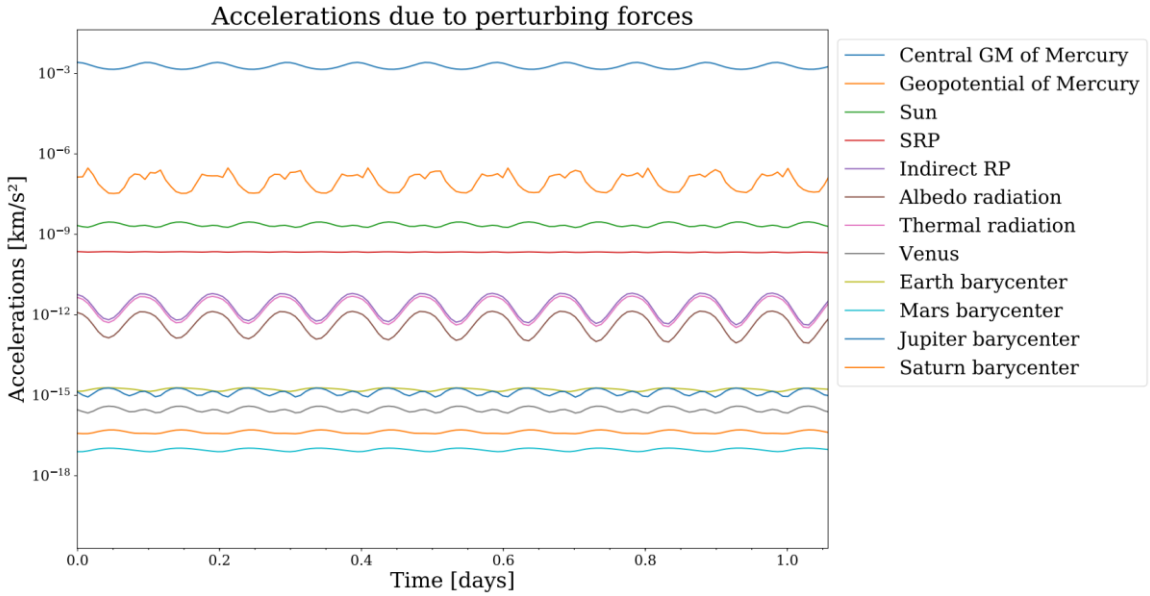

Figure 13. The accelerations acting on MPO during the first day in the orbit

Figure 13 shows a more detailed look on the accelerations during the first day of the spacecraft in the orbit. Hence, the perturbations due to the central GM of Mercury are periodic and depend on the position of the satellite. MPO experiences the maximal accelerations of $3.03 \cdot 10^{-3} \frac{km}{s^2}$ in the periherm and $1.27 \cdot 10^{-3} \frac{km}{s^2}$ in the apoherm. This can be explained with the inverse-square law for the gravitational attraction of a point-like mass. The accelerations due to the geopotential have also a periodic character and depend on the proximity of the spacecraft to the planet. The indirect radiation pressure has a stronger influence on MPO in the periherm than in apoherm. The gravity force of the Sun has an opposite effect depending to the distance the satellite to the Sun due to Newton's gravitational law.

7. Results

7.1. Effect of geopotential of Mercury

In this section, the influence of the geopotential of Mercury on the evolution of the orbital elements of MPO was investigated.

7.1.1. Evolution of the orbital elements of MPO

By preparation of the space mission, it is very important to be able to predict and analysis the changes in the orbital elements of a spacecraft over time. Not all changes in the orbit have a negative effect, but changes in some elements are desirable. For example, the movement of the argument of periapsis is welcome by DLR for operating the BELA altimeter. By this, more surface area can be covered from the lower distance without additional expense of fuel for manoeuvres.

In order to investigate the effect of the gravity field of Mercury on the evolution of orbital elements of MPO systematically and to analysis their consequences, the simulations were performed using gravity fields generated on basis of the scale factors 1, 3, 5 and 10. 10,000 simulations per each scale factor were carried out. Note that only 9,851 simulations from 10,000 were successfully executed for the scale factor 10 due to the collision of the satellite with the planet. In the simulations, only the gravity field of Mercury was taken into account because the gravity field causes the largest perturbations which affect the trajectory of a spacecraft, as shown above in Figure 12. The nominal values for every orbit element were obtained from the simulations based on the nominal values of the gravity field without considering uncertainties.

7.1.2. Evolution of the periherm of MPO

A critical point for the instruments on board of MPO, among other things for BELA altimeter, is the spacecraft altitude. If the periherm falls below 200 km [Khan and Rocchi, 2018], the thermal stress on the instruments may cause an overheating and could damage them. Therefore, this analysis focuses on the changes in periherm r_p.

Figure 14 demonstrates the evolution of the periherm of MPO for the scale factors = 1, 3, 5 and 10 over 2 years. The black line represents the periherm for nominal values without considering the uncertainties. The blue and green lines denote the minimal and maximal values of periherm based on the standard deviations. The yellow and red lines encompass the maximal and minimal values of periherm of all simulations. Note that minimal and maximal values of r_p could belong to different gravity fields per output time step. All values are given in km above ground. The reference radius of Mercury r_M was taken from the input file for generating gravity fields and amounts to 2439.4 km (see section 5.2). The time is given in Earth days and Earth years respectively and is designated shortly as days and years.

The standard deviations were calculated with following formula:

$$\sigma = \sqrt{\frac{\sum(x - \bar{x})^2}{N}} \tag{20}$$

where σ denotes standard deviation, x is each value of the data set, $\bar{x}$ represents nominal value and *N* presents the number of simulations.

The maximal and minimal values of periherm based on the standard deviations ($r_{p,\sigma,max}$ and $r_{p,\sigma,min}$) are the sum of nominal value of periherm plus/minus standard deviation.

In some cases, the periherm falls below 0 km, i.e. the satellite collides with the planet. The Integrator doesn't stop the integration after the crash of the orbiter and continues calculating. As the values lie below 0 km, the results were set to 0 km.

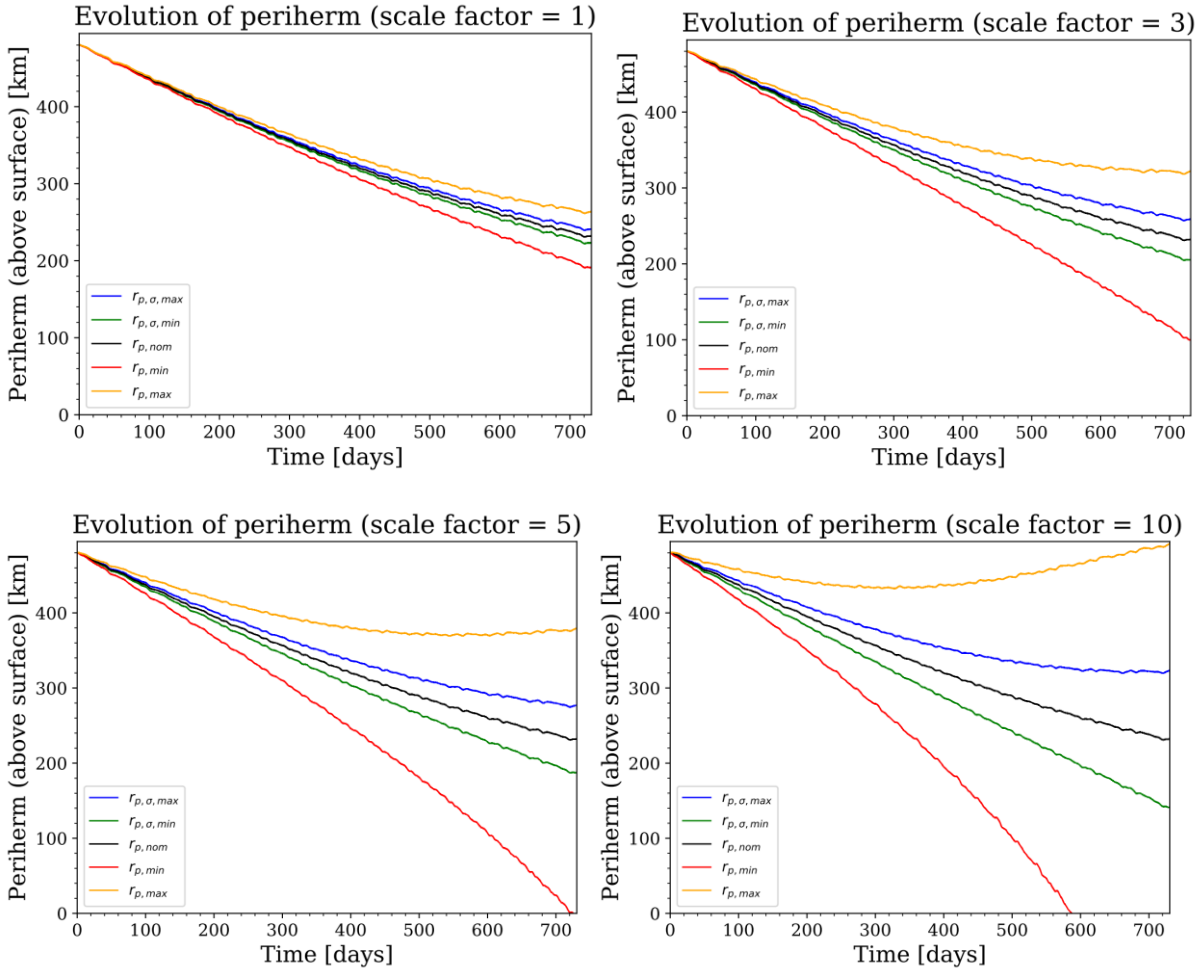

Figure 14. The evolution of the periherm dependent on the scale factor over 2 years

According to the plots, the gravitational potential causes generally a decrease in periherm after 1 and 2 years expect the maximal value for scale factors 5 and 10, which follow the tendency of a slow decline and then begin to increase. The standard deviations are larger with the growing scale factor. The difference between the minimal and maximal values is also greater when the scale factor is bigger. Furthermore, there is a possibility that the spacecraft crashes into the planet after 725 and after 587 days when considering the maximal value for scale factor 5 and the maximal value for scale factor 10 respectively.

Table 11 depicts the nominal values of the periherm $r_{p,nom}$ without considering uncertainties after 1 and 2 years. It can be seen, that $r_{p,nom}$ declines by 30.8 % after the first year and by 51.6 % after 2 years when compared with the initial value of periherm $r_{p,init}$, which accounts for 2920 km or rather 480.6 km when considering above surface. The mean rate of decrease of $r_{p,nom}$ (by assumption of

the linear tendency) is 0.4 km/day after 1 year and 0.3 km/day after 2 years. The mean rate after 2 years is smaller because of slow-moving of $r_{p,nom}$ after 1 year downwards.

r_p [km]	after 1 year	after 2 years
$r_{p,nom}$	332.423	232.555
$r_{p,init}$ - $r_{p,nom}$	148.177	248.045
rate per day	0.405	0.339

Table 11. Nominal values for periherm considering above surface after 1 and 2 years

The general trend of the evolution of r_p for scale factor 1 is even decrease. The standard deviation is 2.9 km after the first year and 8.9 km after 2 years. The periherm declines by 30.2% - 31.5% and by 49.8% - 53.5% in the range of standard deviation after 1 and 2 years respectively when comparing with $r_{p,init}$. These values lie in an acceptable range, whereas the minimal value of r_p after 2 years falls below the critical distance of 200 km which could lead to the damage of the satellite.

When considering the change in the periherm for the scale factor 3, the standard deviation is three times larger than by scale factor 1. The periherm altitude decreases by 29% - 32.6 % and by 46% - 57.2 % in the field of the standard deviation when compared with $r_{p,init}$. The maximal value of the periherm falls slower than by scale factor 1, while the minimal value of r_p has nearly a linear tendency and backs down rapidly reaching the value of 99.8 km after 2 years which could be considered as critical.

The evolution of the periherm for the scale factor 5 looks more pronounced than for the scale factors 1 and 3. The standard deviation is 1.67 times bigger than for the scale factor 3. The periherm in the area of standard deviation changes by 27.9 % - 33.8 % after 1 year and by 42.3% - 61 % after 2 years relative to $r_{p,init}$. The minimal value of r_p based on standard deviation falls already below 200 km after 2 years. The difference between minimal and maximal values varies strongly and amounts to 115.1 km after 1 year and to 379.9 km after 2 years. The maximal values of periherm fall slowly, change the tendency of drop and start to increase approximately after 500 days. As mentioned above, the minimal values of periherm decrease rapidly, i.e. the satellite loses the altitude fast. This leads to the crash of the spacecraft onto the planet after 725 days.

Moreover, the collision of MPO with Mercury could already happen after 587 Earth days when considering the minimal value of periherm for the scale factor 10. The maximal values of periherm drop slowly and start to increase after ca. 285 Earth days reaching the value which exceeds $r_{p,init}$ by 11.8 km after 2 years. As expected, the standard deviation is 10 times bigger than for the scale factor 1 and amount to 28.6 km after 1 year and 91.3 km after 2 years. The periherm falls by 24.9% - 36.8 % and by 32.6% - 70.6 % considering the values in the range of standard deviation after 1 year and after 2 years respectively compared with $r_{p,init}$. The minimal value of r_p in the range of deviation after 2 years can be considered as critical.

The detailed information about the periherm values per scale factor after 1 and 2 years is represented in Table 12 and Table 13.

r_p [km]	scale factor 1	scale factor 3	scale factor 5	scale factor 10
σ	2.865	8.597	14.330	28.602
$r_{p,\sigma,min}$	329.557	323.826	318.092	303.821
$r_{p,\sigma,max}$	335.288	341.019	346.753	361.025
$r_{p,min}$	319.958	294.676	269.310	226.638
$r_{p,max}$	342.483	362.389	384.388	434.478

Table 12. Periherm values above surface after 1 year

r_p [km]	scale factor 1	scale factor 3	scale factor 5	scale factor 10
σ	8.916	26.801	44.858	91.258
$r_{p,\sigma,min}$	223.639	205.753	187.697	141.296
$r_{p,\sigma,max}$	241.470	259.356	277.413	323.813
$r_{p,min}$	191.474	99.775	0	0
$r_{p,max}$	264.217	322.627	379.930	492.416

Table 13. Periherm values above surface after 2 years

In order to have an overview of the distribution of the periherm per scale factor after 1 and 2 years, the box plots were created which are shown in Figure 15.

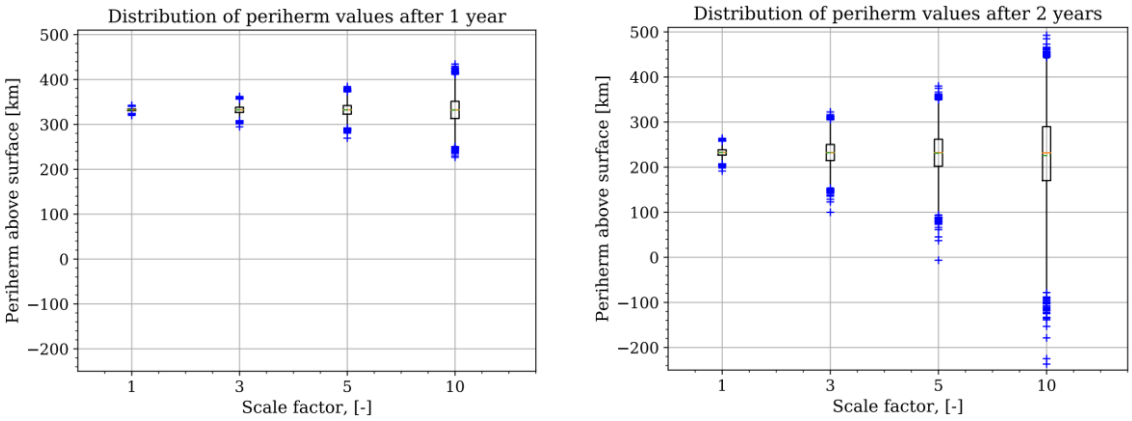

Figure 15. The box plots for the periherm altitude after 1 year and after 2 years

The box extends from the lower to upper quartile values and represents 50% of the data. The orange line, located in the box, denotes the median, which depicts the middle value of the dataset and separates the higher half from the lower half of the sample data. The upper half and lower half of the box separated with the median represents per 24.75% of the data values. The green dashed line encompasses the averaged value of data. The median and the averaged value can be hardly identifiable because they lie either on top of each other or in proximity to each other. The blue crosses depict the outliers values of data which amount to 0.25% per side. The lines extending vertically from the boxes are called whiskers and indicate variability outside the upper and lower quartiles. The values reaching from the lower cap of whisker to the upper cap account for 99% of data.

According to the plots, the likelihood that the periherm falls below 200 km after the first year is equal zero for all scale factors. But it can happen in two from 10,000 cases when considering the periherm values for the scale factor 1 after 2 years. By consideration of the scale factor 3, there is 11.7% of the possibility that the periherm altitude is between 99.8 km and 200 km after 2 years. Moreover, 23.69% of the periherm values for the scale factor 5 after 2 years are below 200 km.

Furthermore, the possibility that the satellite collides with Mercury before or rather after 2 years amounts to 1.5% when taken into consideration the scale factor 10. The likelihood of the values of periherm below 200 km after 2 years is quite large and accounts to 36.2%. Therefore, there is 0.02% of the possibility that the periherm after 2 years is greater than $r_{p,init}$.

In addition, the box plots show clearly the linear dependency of the evolution of periherm over 1 year or rather 2 years on scale factor.

Moreover, the box plot gives the information about symmetry of data dispersion. As can be seen, the distribution is not symmetrical and tends to be left skewed.

A more detailed information about distribution of the periherm values after 1 and 2 years is represented in Table 14.

	scale factor 1		**scale factor 3**		**scale factor 5**		**scale factor 10**	
	after 1 year	*after 2 years*	*after 1 year*	*after 2 years*	*after 1 year*	*after 2 years*	*after 1 year*	*after 2 years*
upper outliers	342.483	264.217	362.389	322.627	384.388	379.93	434.478	492.416
upper whisker	340.48	257.734	356.463	304.92	372.642	349.218	411.615	442.715
upper quartile	334.345	238.551	338.183	250.359	342.06	261.925	351.539	289.732
median	332.402	232.475	332.361	232.318	332.391	232.079	332.317	231.592
lower quartile	330.517	226.628	326.697	214.604	322.827	202.205	313.108	170.147
lower whisker	324.380	207.586	308.153	153.942	291.954	94.149	250.675	-78.304
lower outliers	319.958	191.474	294.676	99.775	269.31	-6.570	226.638	-236.804

Table 14. The important parameter of the box plot dependent on the scale factor after 1 and 2 years

The box plots for the eccentricity and the apoherm and corresponded tables can be found in Appendix.

7.1.3. Evolution of the eccentricity of MPO

The second orbital element eccentricity e determines the form of the orbit. In case of MPO, the initial orbit is highly elliptically with the eccentricity value e_{init} of 0.148688. Figure 16 shows the evolution of the eccentricity of MPO dependent on the scale factor over 2 years. The gravitational potential of Mercury generally causes the eccentricity to increase which means that the orbit becomes more elliptically. This in turn leads to decrease in periherm altitude. All values of the eccentricity follow the tendency of growth, except the minimal values of e for the scale factors 5 and 10.

Table 15 represents the nominal values for the eccentricity e_{nom} without considering the uncertainties after 1 and 2 years. It can be seen, that e_{nom} rises by 29% after 1 year and by 48.7% after 2 years relative to e_{init}. The mean rate of the increase of e_{nom} is 0.0001182/day after 1 year and 0.0000987/day, assuming a linear trend. The mean rate after 2 years is smaller because the eccentricity begins to climb slower after 1 year.

The general trend of evolution of the eccentricity for the scale factor 1 is an ongoing growth. The eccentricity increases by 28.5% - 29.6% after 1 year and by 46.9% - 50.4 % after 2 years when considering the values in the range of standard deviation in terms of e_{init}. The minimal value of the eccentricity changes by 27.1% after 1 year and by 42.4 % after 2 years while the maximal value grows by 31.5% after 1 year and by 56.7 % when compared with e_{init}.

The general trend of evolution of the eccentricity for the scale factor 1 is an ongoing growth. The eccentricity increases by 28.5% - 29.6 % after 1 year and by 46.9% - 50.4 % after 2 years when considering the values in the range of standard deviation in terms of e_{init}. The minimal value of the

eccentricity changes by 27.1% after 1 year and by 42.4% after 2 years while the maximal value grows by 31.5% after 1 year and by 56.7% when compared with e_{init}.

By considering of the eccentricity for the scale factor 3, the standard deviation is larger by 0.00167 after 1 year and by 0.00521 after 2 years in comparison to the scale factor 1. The minimal value of the eccentricity grows by 0.0344 after 1 year and by 0.046 after 2 years with regard to e_{init}. When taken into consideration the values in the range of standard deviations, the eccentricity increases by 27.4% - 36.4% after 1 year and by 43.4% - 53.9% relative to the initial value of e.

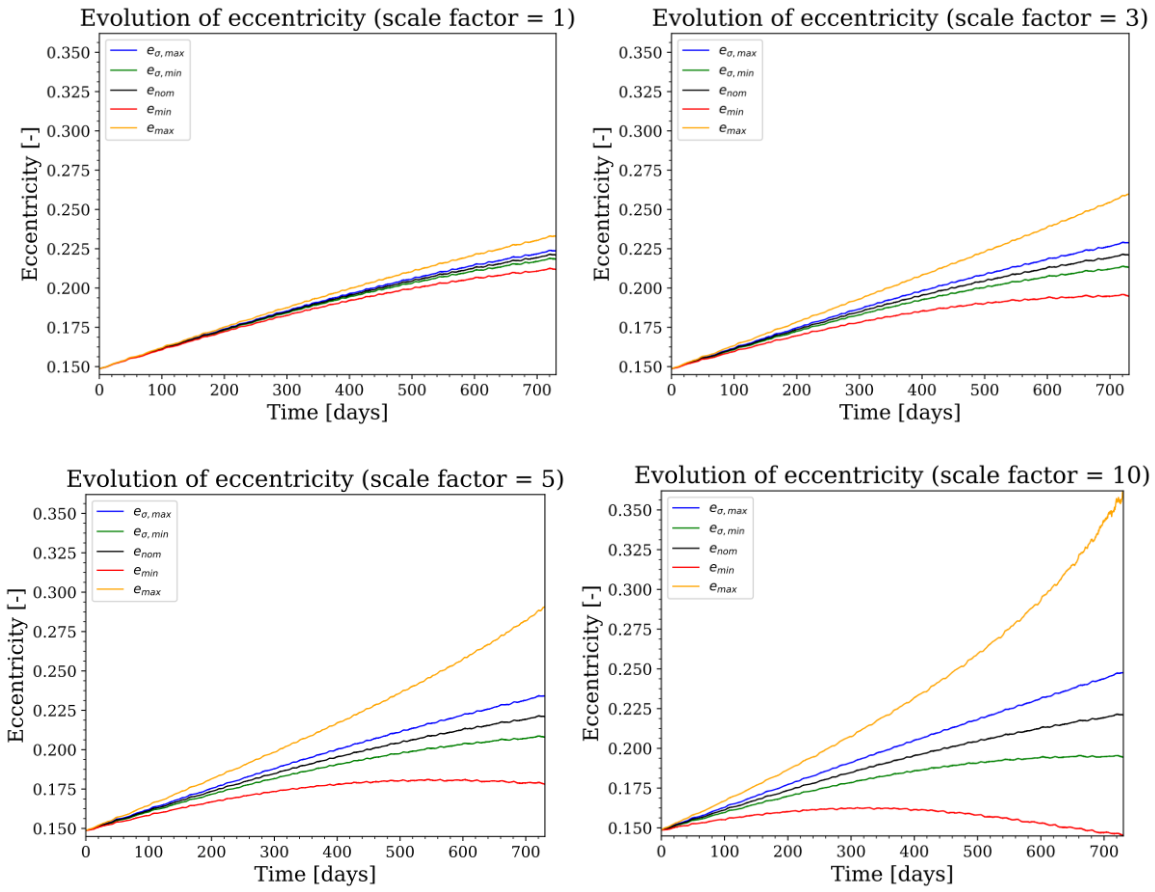

Figure 16. The evolution of the eccentricity dependent on the scale factor over 2 years

***e* [-]**	**after 1 year**	**after 2 years**
e_{nom}	0.1918620	0.2209888
$e_{init} - e_{nom}$	-0.0431740	-0.0723008
rate per day	-0.0001182	-0.0000987

Table 15. Nominal values for eccentricity after 1 and 2 years

When taken into account the values for the scale factor 5, it is clearly seen that the location of the minimal and maximal value of e is not symmetrical relative to the nominal value of the eccentricity. In addition, the difference between the minimal and maximal values after 1 year is greater than the by scale factors 1 and 3 and is 0.0336. As expected, the standard deviation is 5 and 1.67 times bigger than for the scale factor 1 and 3 respectively. The eccentricity values in the area of standard deviation rise by 26.2% – 31.9% after 1 year and by 39.8% – 57.4% after 2 years in terms of e_{init}.

The minimal value of the eccentricity for scale factor 10 doesn't follow the overall trend of the ongoing growth. It increases slowly and begins to back down after the first year, then it reaches the value which is smaller by 0.0034612 than e_{init}. The maximal value of the eccentricity has the tendency of the rapid growth. The considering of e_{max} after 2 years makes no sense due to the

collision of the spacecraft with the planet after 587 days. The difference between the minimal and maximal values of e is 2.6 greater than by scale factor 5. The values for the eccentricity in the range of standard deviation increases by 23.4% - 34.7% after 1 year and by 30.7% - 66.5% after 2 years when compared with e_{init}.

The detailed information about the values of the eccentricity after 1 year and after 2 years for scale factors 1, 3, 5 and 10 is listed in Table 16 and Table 17. The values corresponded to the crash of the satellite on the planet are shown in bold.

***e* [-]**	**scale factor 1**	**scale factor 3**	**scale factor 5**	**scale factor 10**
σ	0.0008354	0.0025065	0.0041782	0.0083393
$e_{\sigma,min}$	0.1910266	0.1893555	0.1876838	0.1835227
$e_{\sigma,max}$	0.1926974	0.1943684	0.1960402	0.2002013
e_{min}	0.1889292	0.1831258	0.1767112	0.1621066
e_{max}	0.1954964	0.2028688	0.2102664	0.2227022

Table 16. Eccentricity values after 1 year

***e* [-]**	**scale factor 1**	**scale factor 3**	**scale factor 5**	**scale factor 10**
σ	0.002599	0.0078137	0.0130781	0.0266057
$e_{\sigma,min}$	0.2183894	0.2131751	0.2079108	0.1943831
$e_{\sigma,max}$	0.2235881	0.2288025	0.2340669	0.2475945
e_{min}	0.2117578	0.1947289	0.1780219	0.1452268
e_{max}	0.2329656	0.2596999	**0.2907041**	**0.3578205**

Table 17. Eccentricity values after 2 years

7.1.4. Evolution of the apoherm of MPO

Due to the increase of the eccentricity that leads to the decrease in periherm, the apoherm rises because the semi-major axis remains constant. Although the treatment of the apoherm is redundant to the eccentricity, the evolution of the apoherm was added to analysis of the orbital elements nevertheless.

Figure 17 demonstrates the evolution of the apoherm r_a of MPO dependent on the scale factor over 2 years. The apoherm follows generally the tendency of the growth after 1 year and 2 years except the maximal value of the apoherm for the scale factors 5 and 10 which begin to fall after slow rise. The standard deviations are larger with the increasing scale factor. The minimal and maximal values have also more significant divergences when the scale factor is bigger. The initial value of apoherm $r_{a,init}$ amounts to 3940 km and 1500.6 km when considering from the surface of Mercury.

The detailed information about the values of the apoherm after 1 year and after 2 years for scale factors 1, 3, 5 and 10 is listed in Table 18, Table 19 and Table 20. The values corresponded to the crash of the satellite on the planet are shown in bold.

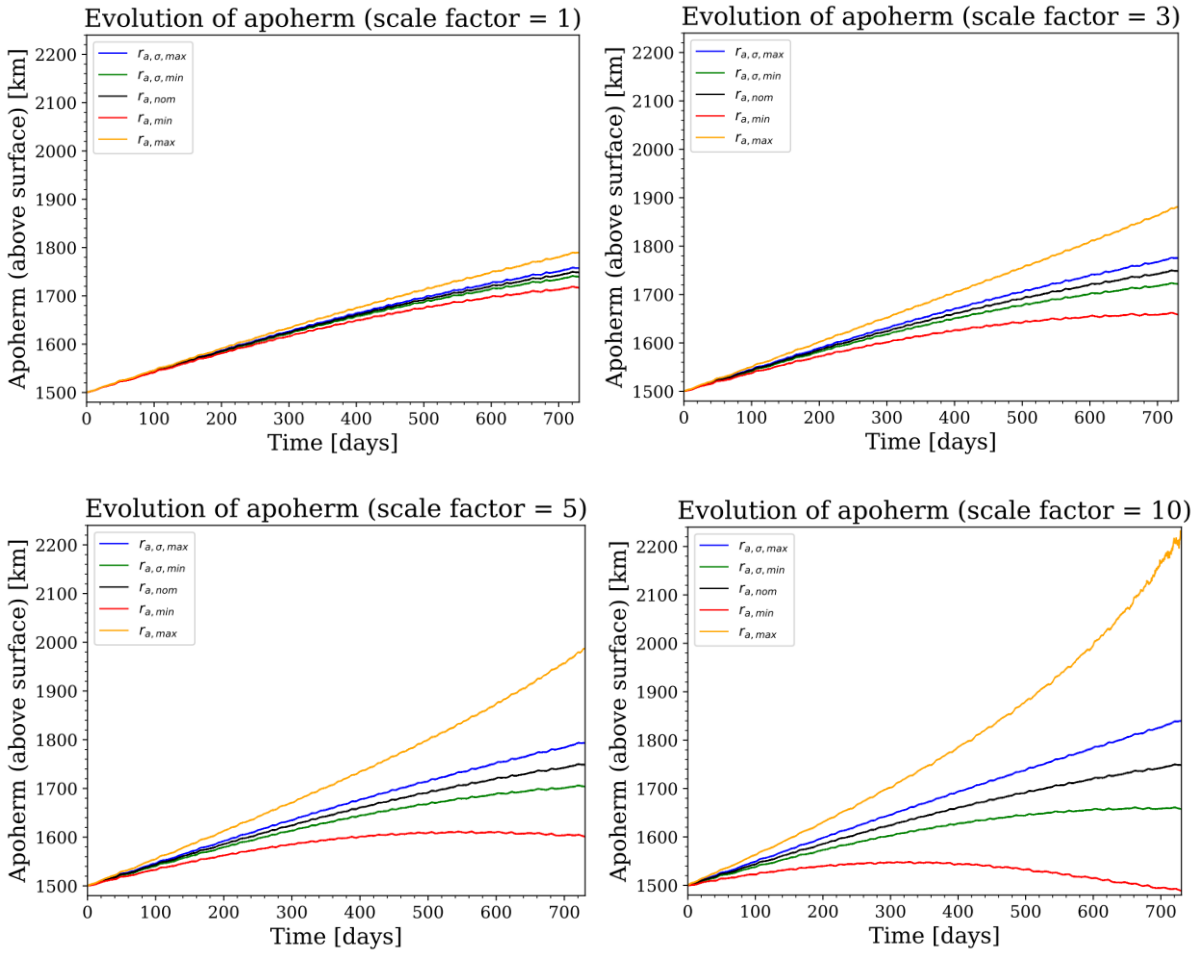

Figure 17. The evolution of the apoherm dependent on the scale factor over 2 years

r_a [km]	after 1 year	after 2 years
$r_{a,nom}$	1648.553	1748.507
$r_{a,init}$ - $r_{a,nom}$	-147.953	-247.907
rate per day	-0.405	-0.339

Table 18. Nominal values for apoherm after 1 and 2 years

r_a [km]	scale factor 1	scale factor 3	scale factor 5	scale factor 10
σ	2.866	8.597	14.331	28.604
$r_{a,\sigma,min}$	1645.688	1639.956	1634.222	1619.949
$r_{a,\sigma,max}$	1651.419	1657.150	1662.885	1677.157
$r_{a,min}$	1638.495	1618.592	1596.587	1546.492
$r_{a,max}$	1661.021	1686.313	1711.696	1754.321

Table 19. Apoherm values above surface after 1 year

r_a [km]	scale factor 1	scale factor 3	scale factor 5	scale factor 10
σ	8.915	26.799	44.855	91.252
$r_{a,\sigma,min}$	1739.592	1721.708	1703.652	1657.256
$r_{a,\sigma,max}$	1757.423	1775.307	1793.362	1839.759
$r_{a,min}$	1716.848	1658.441	1601.137	1488.652
$r_{a,max}$	1789.586	1881.278	**1987.615**	**2217.755**

Table 20. Apoherm values above surface after 2 years

7.1.5. Evolution of the semi-major axis of MPO

Although the gravitational potential causes increase in the eccentricity and decrease in the periherm altitude, the semi-major axis remains almost constant over time.

Figure 18 shows the evolution of the semi-major axis of MPO dependent on the scale factor over 2 years. The black line represents the semi-major axis for nominal values without considering the uncertainties. The blue and green lines denote the minimal and maximal values of semi-major axis based on the standard deviations. The blue dashed and green dashed lines encompass the maximal and minimal values of semi-major axis of all simulations.

The evolution of the semi-major axis has a periodical character. The oscillations are caused by the periodic part of the perturbations due to the gravitational potential of Mercury. It can be seen, that the period of the oscillation corresponds to one half rotation of Mercury about its axis. Moreover, the amplitude of the oscillations grows slightly with the increasing scale factor and with rising number of mission days.

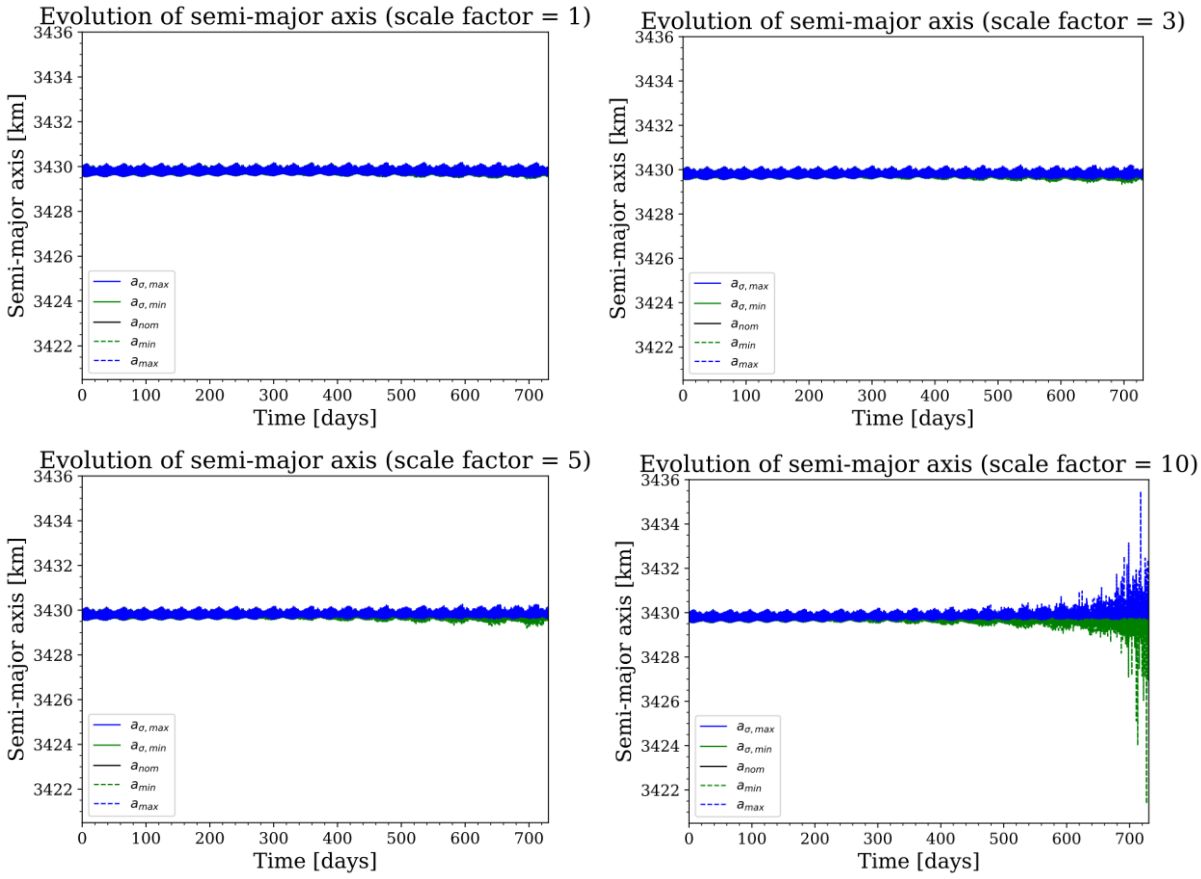

Figure 18. The evolution of the semi-major axis dependent on the scale factor over 2 years

7.1.6. Evolution of the inclination of MPO

Figure 19 shows the evolution of the inclination dependent on the scale factor over 2 years. The inclination remains constant over time like the semi-major axis with minor periodical oscillations. The period of the oscillation corresponds to one half rotation of Mercury about its axis. Therefore, the amplitude of the oscillations grows with the rising scale factor.

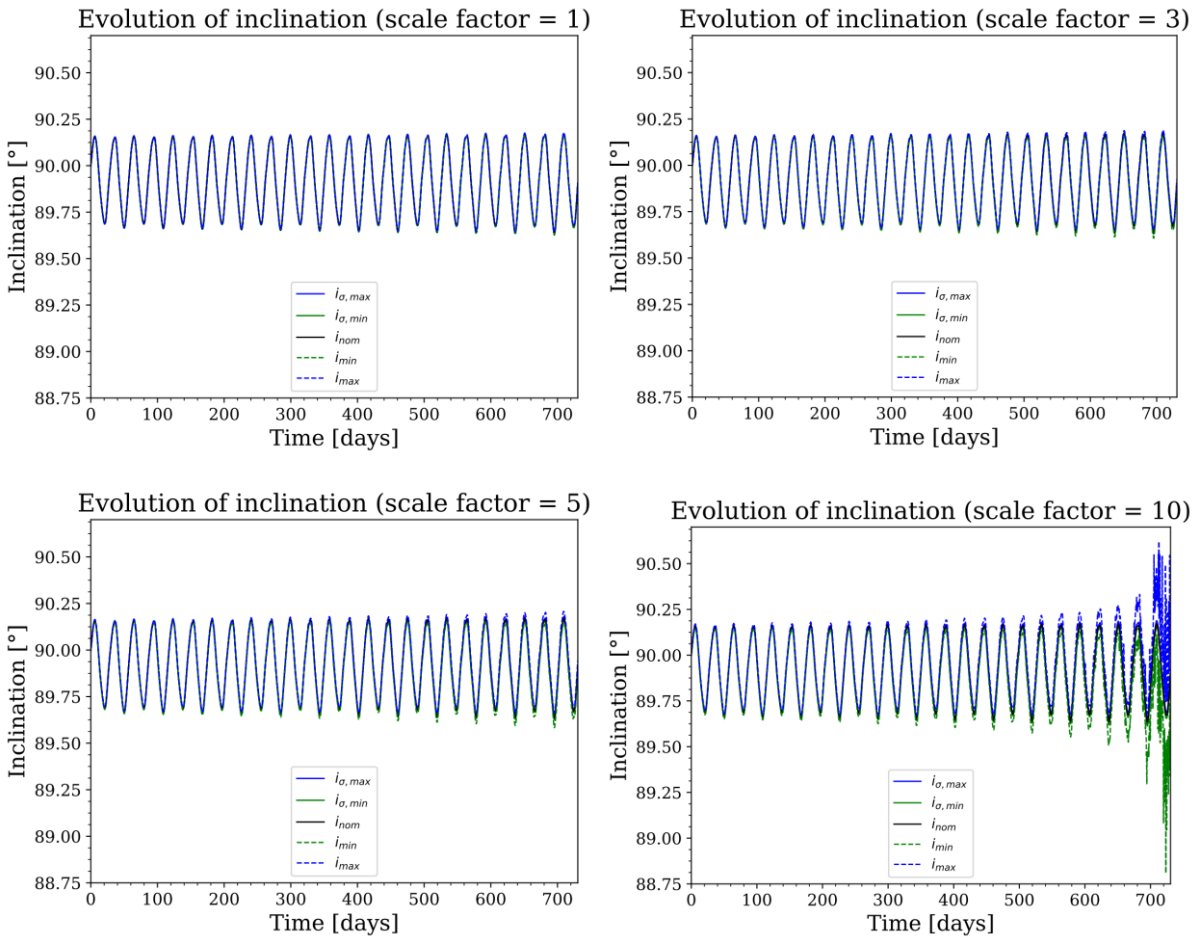

Figure 19. The evolution of the inclination dependent on the scale factor over 2 years

7.1.7. Evolution of the argument of periapsis of MPO

As mentioned above, the changes in the argument of periapsis is desirable in the scope of the mission of MPO because more surface area of Mercury can be investigated by the altimeter BELA from the lower altitude. Note that altitudes above 1,000 km to the surface of Mercury are not applicable for the BELA instrument [Lüdicke, 2008] due to the low signal to noise ratio at higher altitudes.

Figure 20 shows the evolution of the argument of periapsis ω of MPO dependent on the scale factor over 2 years. According to the plots, the overall tendency of the evolution of ω is steady decline over time. The changes in the position of ω can be explained by the influence of the flattening [Tresaco et al., 2018] and the North-South mass asymmetry of Mercury [Khan and Rocchi, 2018].

Table 21 depicts the nominal value of the argument of periapsis ω_{nom} without considering the uncertainties after 1 and 2 years. It decreases by 32.59° after 1 year and by 61.2° after 2 years relative to the initial value of argument of periapsis ω_{init} amounted to 16°. The mean rate of the decline is 0.09°/day after 1 year and 0.08°/day after 2 years.

The standard deviation for the scale factor 1 is small. The argument of periapsis in the range of deviation decreases by 32.5°- 32.9° after 1 year and by 60.67°- 61.73° after 2 years comparative to ω_{init}. The minimal and maximal values differ not strongly from the nominal value.

The argument of periapsis in the region of deviation for the scale factor 3 declines by 32.31°- 32.87° after 1 year and by 59.6°- 62.8° after 2 years when compared with the initial value. The difference between the minimal and maximal values is larger and amounts to 2.2° after 1 year and to 13.18° after 2 years.

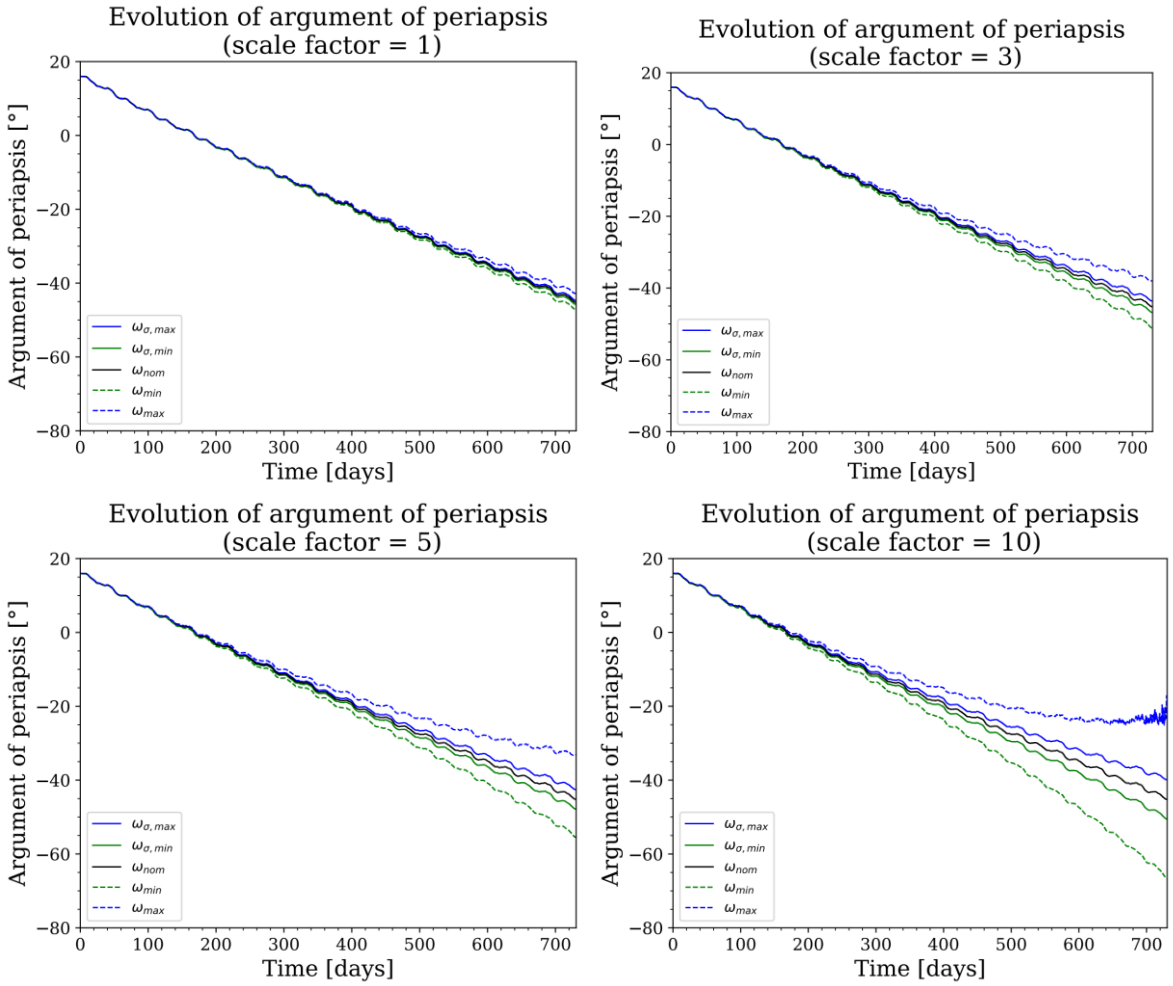

Figure 20. The evolution of the argument of periapsis dependent on the scale factor over 2 years

ω [°]	**after 1 year**	**after 2 years**
ω_{nom}	-16.5897	-45.1951
ω_{init} - ω_{nom}	32.5897	61.1951
rate per day	0.0892	0.0838

Table 21. Nominal values for argument of periapsis after 1 and 2 years

The values of ω in area of standard deviation for the scale factor 5 fall stronger by 0.37° after 1 year and by 2.13° after 2 years than for the scale factors 1 and 3 in comparison to ω_{init}. The minimal value of ω decreases by 34.31° after 1 year and by 71.49° after 2 years while the maximal value drops by 30.61° after 1 year and by 49.09° after 2 years when compared with ω_{init}.

The argument of periapsis in the range of deviation for the scale factor 10 has more significant changes than for the scale factors 1, 3 and 5 by comparison with the initial value of ω. The standard deviation is approximately two times bigger than for the scale factor 5 after 2 years. A more detailed information about the values of the argument of periapsis dependent on the scale factor after 1 and 2 years is demonstrated in Table 22 and Table 23.

ω [°]	scale factor 1	scale factor 3	scale factor 5	scale factor 10
σ	0.0932	0.2797	0.4662	0.9316
$\omega_{\sigma,min}$	-16.6829	-16.8693	-17.0559	-17.5213
$\omega_{\sigma,max}$	-16.4965	-16.3100	-16.1234	-15.6580
ω_{min}	-16.9181	-17.5838	-18.3094	-20.1214
ω_{max}	-16.1856	-15.3875	-14.6129	-13.3556

Table 22. Values for argument of periapsis after 1 year

ω [°]	scale factor 1	scale factor 3	scale factor 5	scale factor 10
σ	0.5311	1.5949	2.6646	5.3703
$\omega_{\sigma,min}$	-45.7262	-46.7900	-47.8597	-50.5655
$\omega_{\sigma,max}$	-44.6640	-43.6002	-42.5305	-39.8248
ω_{min}	-47.1725	-51.1678	-55.4912	-66.6767
ω_{max}	-42.8051	-37.9923	-33.0853	-20.8924

Table 23. Values for argument of periapsis after 2 years

7.1.8. Evolution of the longitude of ascending node of MPO

The evolution of the longitude of ascending node Ω dependent on the scale factor over 2 years is represented in Figure 21. The overall tendency is the decrease with periodic oscillations caused by orbital period of the satellite and rotational period of the planet [Tresaco, 2018]. The maximal values of Ω for the scale factor 5 and 10 don't follow the general trend and start to grow after slow decrease. The standard deviation becomes larger with the increasing scale factor and growing number of the mission days. The amplitude of the oscillations climbs over time. The variations between minimal and maximal values are larger with the rising scale factor and over time.

Table 21 depicts the nominal value of the longitude of ascending node without considering uncertainties Ω_{nom} after 1 and 2 years. It decreases by 0.31° after 1 year and by 0.69° after 2 years when compared with the initial value of the longitude of ascending node Ω_{init} which accounts for 67.8°.

The longitude of the ascending node in the range of standard deviations falls by 0.30°-0.31° after 1 year and by 0.67°-0.7° after 2 years for the scale factor 1, by 0.294°- 0.317° after 1 year and 0.65°-0.72° after 2 years for the scale factor 3, 0.287°- 0.324° after 1 year and by 0.63°- 0.75° after 2 years considering the scale factor 5 and by 0.27°- 0.34° after 1 year and by 0.57°- 0.81° after 2 years taken into account the scale factor 10 when compared with Ω_{init}.

A more detailed information about the values of the longitude of the ascending node dependent on the scale factor after 1 and 2 years is demonstrated in Table 22 and Table 23.

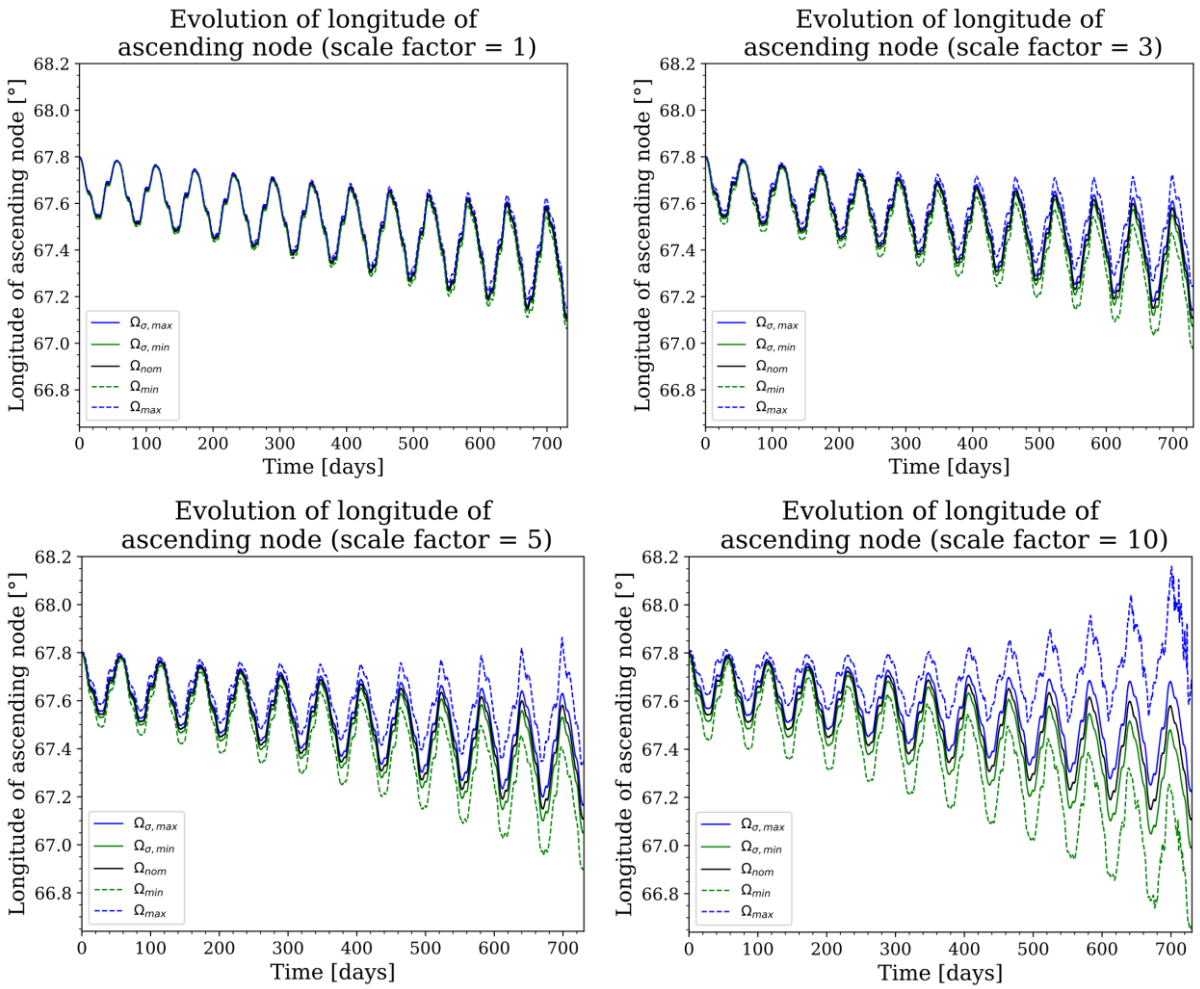

Figure 21. The evolution of the longitude of the ascending node dependent on the scale factor over 2 years

Ω [°]	**after 1 year**	**after 2 years**
Ω_{nom}	67.4943	67.1134
Ω_{init} - Ω_{nom}	0.3057	0.6866

Table 24. Nominal values for longitude of ascending node

Ω [°]	**scale factor 1**	**scale factor 3**	**scale factor 5**	**scale factor 10**
σ	0.0037	0.0112	0.0187	0.0375
$\Omega_{\sigma,min}$	67.4906	67.4831	67.4756	67.4568
$\Omega_{\sigma,max}$	67.4981	67.5056	67.5130	67.5318
Ω_{min}	67.4792	67.4494	67.4196	67.3473
Ω_{max}	67.5091	67.5386	67.5681	67.6428

Table 25. Values for longitude of ascending node after 1 year

Ω [°]	**scale factor 1**	**scale factor 3**	**scale factor 5**	**scale factor 10**
σ	0.0117	0.0350	0.0586	0.1201
$\Omega_{\sigma,min}$	67.1018	67.0784	67.0548	66.9933
$\Omega_{\sigma,max}$	67.1251	67.1484	67.1720	67.2335
Ω_{min}	67.0670	66.9776	66.8911	66.6665
Ω_{max}	67.1587	67.2506	67.3504	67.6785

Table 26. Values for longitude of ascending node after 2 years

7.2. Analytical analysis of influence of the harmonic coefficients J_2, J_3 and J_4

In this section, the influence of the gravitational harmonic coefficients J_2, J_3 and J_4 on the evolution of the longitude of ascending node, the argument of periapsis and the eccentricity was analytically analysed. This analysis gives only approximately estimation of the effect of the coefficients assuming the linear tendency. Note that the coefficients J_2, J_3 and J_4 are normalized.

The influence of J_2, which mainly causes the precession of the longitude of ascending node and the rotation of the argument of periapsis, is described by the following formulas:

$$\dot{\Omega} = -\frac{3}{2} J_2 n \left(\frac{R_{planet}}{p}\right)^2 cos\, i \tag{21}$$

$$\dot{\omega} = \frac{3}{4} J_2 n \left(\frac{R_{planet}}{p}\right)^2 (5\ \cos^2 i - \ 1) \tag{22}$$

Here, p is semi-latus rectus with $p = a \cdot (1 - e^2)$ and n is mean motion with $n = \sqrt{\frac{GM}{a^3}}$.

The semi-latus rectus of MPO is 3354.2 km while the mean motion accounts for $7.3889 \cdot 10^{-4}$ rad/sec when considering the nominal value for GM.

The change in Ω due to J_2 is equal zero because the orbit of MPO is polar with i = 90°.

The change in ω due to J_2 is -11.92903°/year. The standard deviations, as well as minimal and maximal values for $\dot{\omega}$ dependent on the scale factor are given in Table 27.

$\dot{\omega}$ [°/year]	scale factor 1	scale factor 3	scale factor 5	scale factor 10
σ	0.0002047	0.0006142	0.0010171	0.0020342
$\dot{\omega}_{min}$	-11.9298	-11.9315	-11.9331	-11.9372
$\dot{\omega}_{max}$	-11.9283	-11.9269	-11.9252	-11.9213

Table 27. Change in argument of periapsis dependent on the scale factor due to J_2 after 1 year.

J_3 predominantly affects the eccentricity and the argument of periapsis. The influence of J_3 is given by the formulas:

$$\dot{e} = \frac{3}{8} J_3 n \left(\frac{R_{planet}}{p}\right)^3 (1 - e^2)\, cos\, \omega \tag{23}$$

$$\dot{\omega} = \frac{3}{8} J_3 n \left(\frac{R_{planet}}{p}\right)^3 \frac{1 + 4e^2}{e}\ sin\, \omega \tag{24}$$

The change in the eccentricity of MPO due to J_3 is 0.0150323/year while the change in the argument of periapsis amounts to -1.8488°/year when considering the nominal values in both cases. The standard deviations, as well as minimal and maximal values for $\dot{e}$ and $\dot{\omega}$ dependent on the scale factor are shown in Table 28 and Table 29 respectively.

$\dot{e}$ [1/year]	scale factor 1	scale factor 3	scale factor 5	scale factor 10
σ	$2.8115 \cdot 10^{-6}$	$8.4346 \cdot 10^{-6}$	$1.3974 \cdot 10^{-5}$	$2.7947 \cdot 10^{-5}$
$\dot{e}_{min}$	0.01502195	0.01500123	0.01498314	0.01493397
$\dot{e}_{max}$	0.01504233	0.01506237	0.01508498	0.01513765

Table 28. Change in eccentricity dependent on the scale factor due to J_3 after 1 year

$\dot{\omega}$ [°/year]	scale factor 1	scale factor 3	scale factor 5	scale factor 10
σ	0.0003458	0.0010373	0.0017186	0.0034371
$\dot{\omega}_{min}$	-1.85	-1.8525	-1.8552	-1.8617
$\dot{\omega}_{max}$	-1.8475	-1.8449	-1.8427	-1.8367

Table 29. Change in argument of periapsis dependent on the scale factor due to J_3 after 1 year

The gravitational coefficient J_4 mainly causes the change in the argument of periapsis on a polar orbit. It is described by [Schuster and Jehn, 2014]:

$$\dot{\omega} = -\frac{15}{32} J_4 n \left(\frac{R_{planet}}{p}\right)^4 \left[3 + \frac{9}{4}e^2 - \left(1 + \frac{5}{2}e^2\right)\cos(2\omega)\right] \quad (25)$$

The change in ω considering the nominal value affected by J_4 accounts for -2.2128°/year. The change in the argument of periapsis for the minimal and maximal values, as well as standard deviations dependent on the scale factor is presented in Table 30.

$\dot{\omega}$ [°/year]	scale factor 1	scale factor 3	scale factor 5	scale factor 10
σ	0.0009836	0.0029507	0.0048854	0.0097708
$\dot{\omega}_{min}$	-2.2164	-2.2236	-2.2333	-2.2538
$\dot{\omega}_{max}$	-2.2096	-2.2031	-2.1950	-2.1773

Table 30. Change in argument of periapsis dependent on the scale factor due to J_4 after 1 year

7.3. Comparison with additional perturbing forces

7.3.1. Gravity of the Sun

Since the second major perturbing force affecting the trajectory of the orbiter is the gravitational attraction of the Sun, 10,000 simulations were performed using the gravity fields generated on basis of the scale factor 1 taking the gravity field of Mercury, as well as the gravity force of the Sun as a mass point into account. The aim of these simulations is comparison of the results of the simulations considering only gravity field of Mercury and the both effects to investigate and understand the changing the trajectory of MPO.

Figure 22 (left) demonstrates the evolution of the periherm of MPO considering the effect of the gravity field of Mercury while the changes in the periherm of the spacecraft, taken the influence of the geopotential of Mercury, as well as the attraction of the Sun into account, is shown by Figure 22 (right). According to the plots, the gravity force of the Sun has generally a positive effect on the evolution of the periherm after 2 years in the orbit. The Sun generally causes an increase in periherm altitude. On the other hand, as it can be seen by Table 24, the tendency up to the first year is opposite to the trend afterwards. The nominal value of periherm considering the gravity field of Mercury is greater by 1 km after 1 year and smaller by 25.8 km after 2 years compared to the nominal value of the periherm including the gravity force of the Sun. Hence, the standard deviation including the Sun doesn't differ significantly from the standard deviation without the third body effect after 1 year and is smaller by 0.04 km. The difference in standard deviation after 2 years is a little bit larger and amounts to 0.5 km.

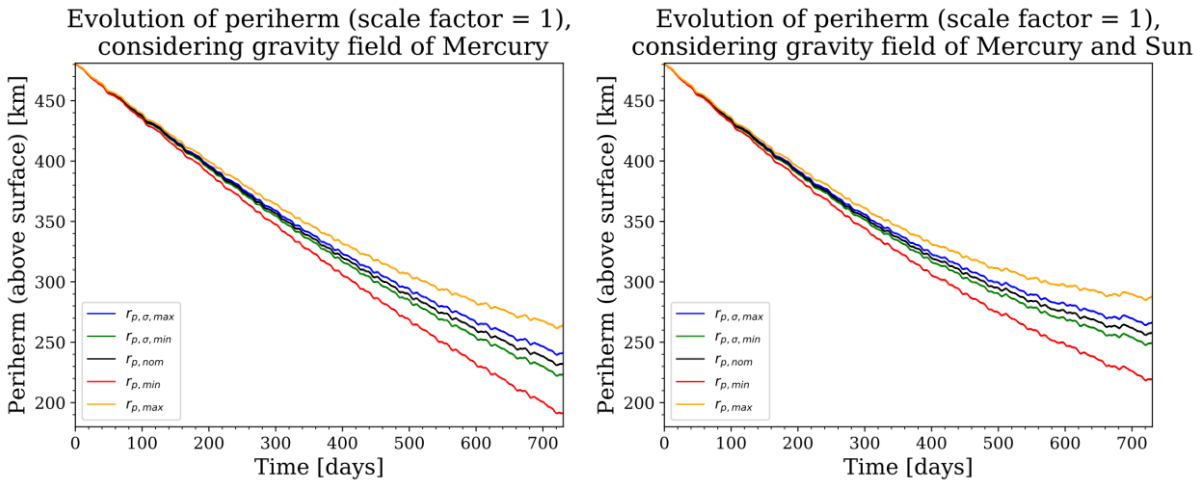

Figure 22. The evolution of the periherm considering the gravity field of Mercury over 2 years (left); The evolution of the periherm considering the gravity field of Mercury and the Sun as a mass point over 2 years (right).

While the minimal value of periherm exceeds the critical distance of 200 km when considering the gravity field of Mercury only, the minimal value of r_p including the Sun is in the acceptable range after 2 years.

A more detailed information about values of the periherm within and without considering of the gravity of the Sun is depicted in Table 31, Table 32 and Table 33.

$r_{p,M,S}$ [km]	after 1 year	after 2 years
$r_{p,nom}$	331.417	258.307
$r_{p,init}$ - $r_{p,nom}$	149.183	222.293
rate per day	0.408	0.304

Table 31. Nominal values for periherm considering the effect of the gravity field of Mercury and the gravity force of the Sun

r_p [km]	gravity field of Mercury	both effects
σ	2.865	2.821
$r_{p,\sigma,min}$	329.557	328.596
$r_{p,\sigma,max}$	335.288	334.238
$r_{p,min}$	319.958	319.167
$r_{p,max}$	342.483	341.314

Table 32. Periherm values above surface after 1 year

r_p [km]	Gravity field of Mercury	both effects
σ	8.916	8.417
$r_{p,\sigma,min}$	223.639	249.891
$r_{p,\sigma,max}$	241.470	266.724
$r_{p,min}$	191.474	219.744
$r_{p,max}$	264.217	288.251

Table 33. Periherm values above surface after 2 years

Figure 23 (left) shows the evolution of the eccentricity of MPO taken the geopotential of Mercury into account over 2 years. Figure 23 (right) represents the changes in the eccentricity of the satellite considering both perturbing forces. The eccentricity does not rise strongly when an attraction of the Sun is taking into account. The standard deviation is a little bit smaller when the gravity force of the Sun is included than without it and differs by 0.0000129 after 1 year and by 0.0002552 after 2 years.

A more detailed information about the values of the eccentricity considering the gravity field of Mercury and the geopotential of Mercury with the gravity force of the Sun is presented in Table 34, Table 35 and Table 36.

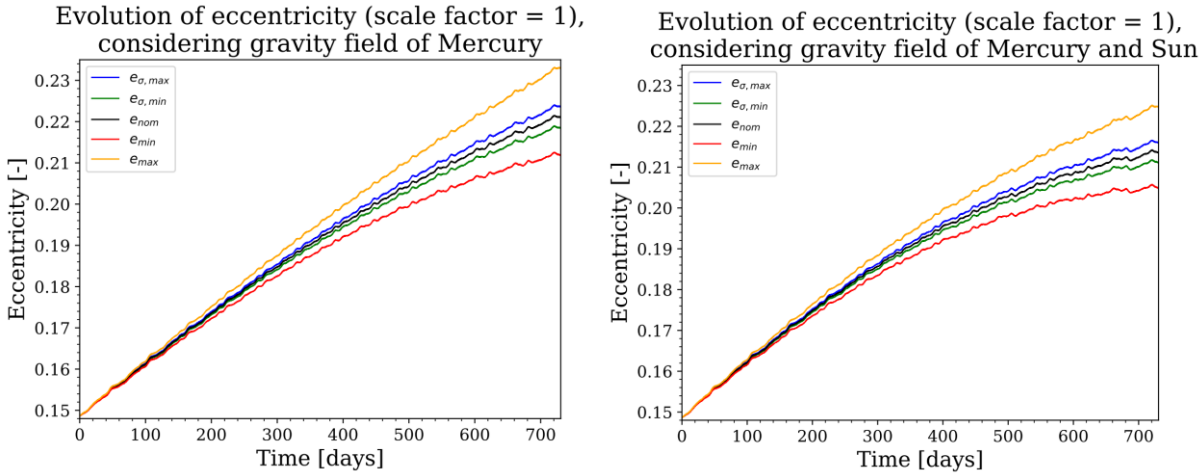

Figure 23. The evolution of the eccentricity considering the gravity field of Mercury over 2 years (left); The evolution of the eccentricity considering the gravity field of Mercury and the Sun as mass point over 2 years (right)

$e_{M,S}$ [-]	after 1 year	after 2 years
e_{nom}	0.1921561	0.2134819
$e_{init} - e_{nom}$	-0.0434681	-0.0647939
rate per day	-0.00011901	-0.0000887

Table 34. Nominal values for eccentricity considering the gravity field of Mercury and the gravity of the Sun

e [-]	gravity field of Mercury	both effects
σ	0.0008354	0.0008225
$e_{\sigma,min}$	0.1910266	0.1913336
$e_{\sigma,max}$	0.1926974	0.1929787
e_{min}	0.1889292	0.1892709
e_{max}	0.1954964	0.1957283

Table 35. Eccentricity values after 1 year

e [-]	gravity field of Mercury	both effects
σ	0.002599	0.0023438
$e_{\sigma,min}$	0.2183894	0.2110281
$e_{\sigma,max}$	0.2235881	0.2159357
e_{min}	0.2117578	0.2047521
e_{max}	0.2329656	0.2247247

Table 36. Eccentricity values after 2 years

Figure 24 show the evolution of the apoherm of MPO considering only the gravity field of Mercury (left) and both perturbing forces (right) over 2 years respectively. According to the plots, the Sun causes the small increase in the apoherm after the first year and a bigger decrease after 2 years, namely the apoherm by considering the both effects reaches smaller values than without taking the third body effect into account. The standard deviation of the apoherm by taking the gravity field of Mercury and the attraction of the Sun into consideration is smaller than without the gravity of the Sun.

A more detailed information about the values of the apoherm considering the gravity field of Mercury and the geopotential of Mercury with the gravity force of the Sun is presented in Table 37, Table 38 and Table 39.

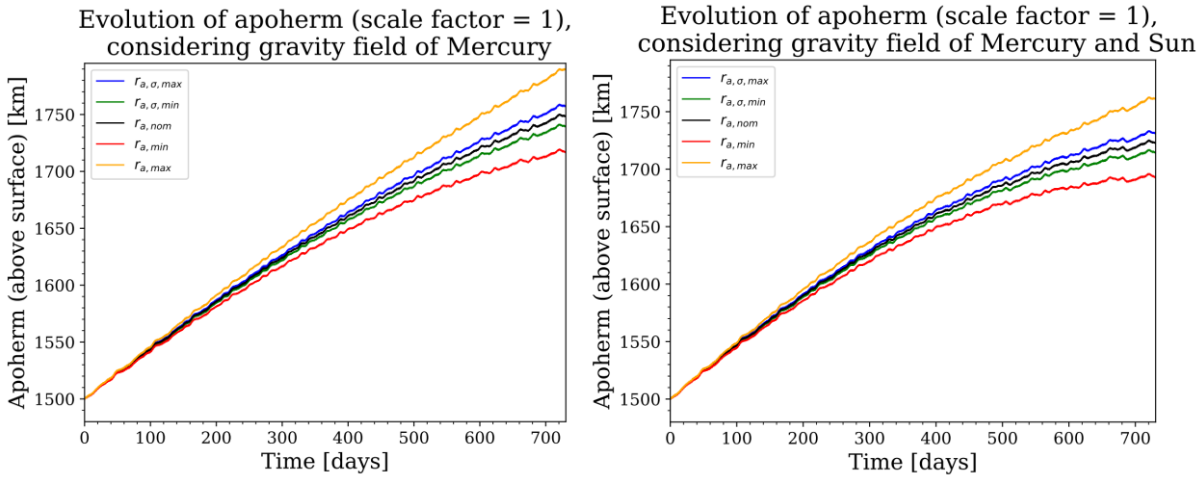

Figure 24. The evolution of the apoherm considering the gravity field of Mercury over 2 years (left); The evolution of the apoherm considering the gravity field of Mercury and the Sun as mass point over 2 years (right)

$r_{a,M,S}$ [km]	after 1 year	after 2 years
$r_{a,nom}$	1649.567	1722.766
$r_{a,start}$ - $r_{a,nom}$	-148.967	-222.166
rate per day	-0.408	-0.304

Table 37. Nominal values for apoherm above surface considering the gravity field of Mercury and the gravity of the Sun

r_a [km]	gravity field of Mercury	both effects
σ	2.866	2.821
$r_{a,\sigma,min}$	1645.688	1646.745
$r_{a,\sigma,max}$	1651.419	1652.388
$r_{a,min}$	1638.495	1639.671
$r_{a,max}$	1661.021	1661.821

Table 38. Apoherm values above surface after 1 year

r_a [km]	gravity field of Mercury	both effects
σ	8.915	8.416
$r_{a,\sigma,min}$	1739.592	1714.350
$r_{a,\sigma,max}$	1757.423	1731.182
$r_{a,min}$	1716.848	1692.825
$r_{a,max}$	1789.586	1761.327

Table 39. Apoherm values above surface after 2 years

Figure 25 and Figure 26 demonstrate the evolution of the longitude of ascending node and argument of periapsis respectively over 2 years. The left plots show the change in Ω and ω taking the gravitational potential of Mercury into consideration, the right plots represent the evolution of Ω and ω considering the gravity field of Mercury as well as the attraction of the Sun. It can be seen, that the Sun causes a slower decrease of the longitude of ascending node and the argument of periapsis than by taking only the gravity field into account. For example, the difference between nominal values of Ω is 0.0138° after 1 years and 0.0422°, and between nominal values of ω amounts to 2.13° after 1 year and to 3.07° after 2 years. The standard deviation by considering the both perturbing forces is smaller than without the Sun.

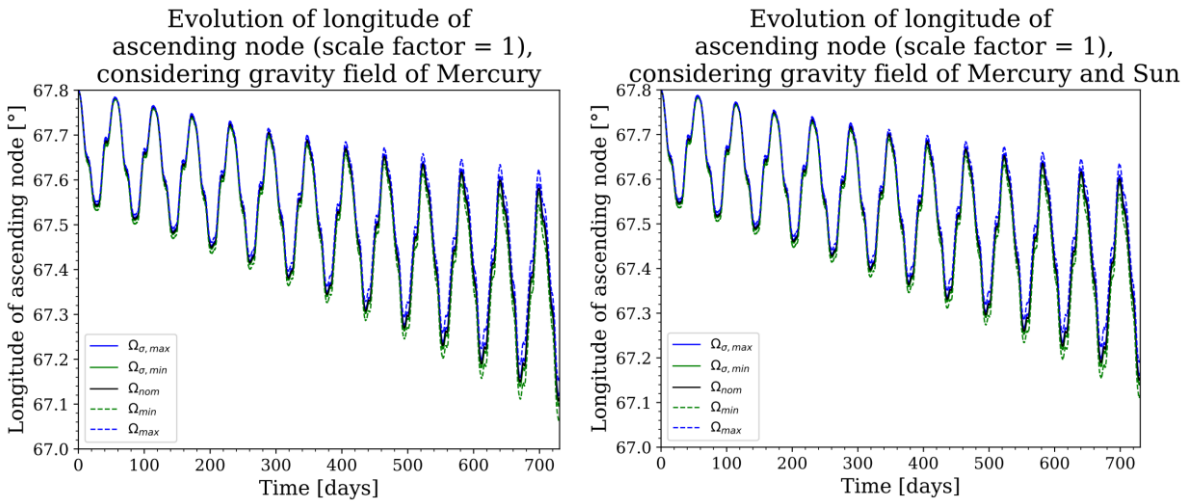

Figure 25. The evolution of the longitude of ascending node considering gravity field of Mercury over 2 years (left); The evolution of the eccentricity considering the gravity field of Mercury and the Sun as a mass point over 2 years (right)

Table 40, Table 41, Table 42, Table 43, Table 44 and Table 45 represent a more detailed information about the values of Ω and ω within and without considering of the gravity force of the Sun after 1 and 2 years.

$\Omega_{M,S}$ [°]	after 1 year	after 2 years
Ω_{nom}	67.5081	67.1556
Ω_{init} - Ω_{nom}	0.2919	0.6444

Table 40. Nominal values for longitude of ascending node the gravity field of Mercury and the gravity of the Sun

Ω [°]	**gravity field of Mercury**	**both effects**
σ	0.0037	0.0035
$\Omega_{\sigma,min}$	67.4906	67.5045
$\Omega_{\sigma,max}$	67.4981	67.5117
Ω_{min}	67.4792	67.4938
Ω_{max}	67.5091	67.5220

Table 41. Values for the longitude of ascending node after 1 year

Ω [°]	**gravity field of Mercury**	**both effects**
σ	0.0117	0.0106
$\Omega_{\sigma,min}$	67.1018	67.1661
$\Omega_{\sigma,max}$	67.1251	67.1450
Ω_{min}	67.0670	67.1150
Ω_{max}	67.1587	67.1975

Table 42. Values for the longitude of ascending node after 2 years

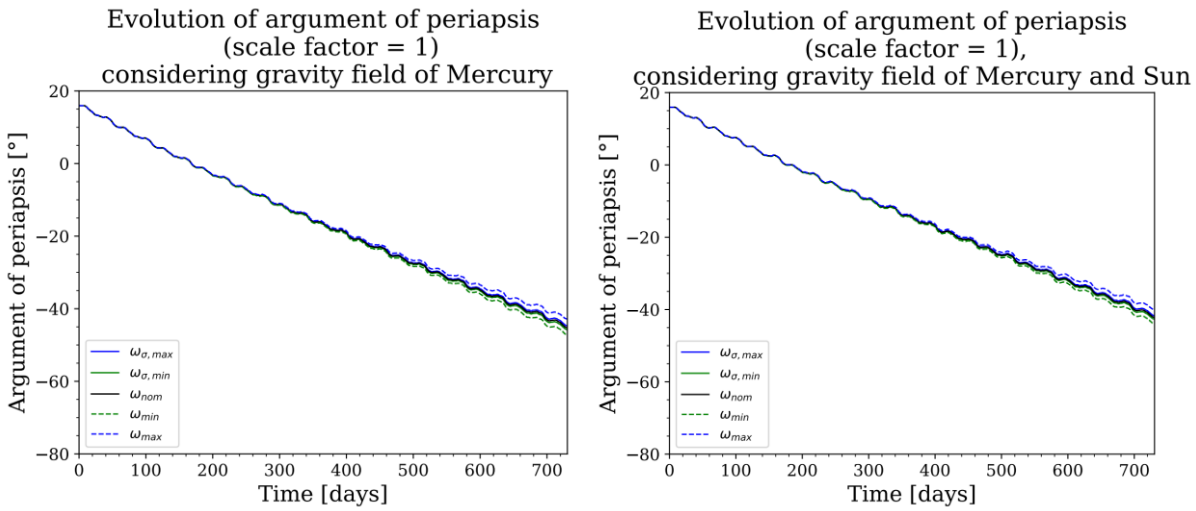

Figure 26. The evolution of the argument of periapsis considering gravity field of Mercury over 2 years (left); The evolution of the eccentricity considering gravity field of Mercury and Sun as a mass point (right)

$\omega_{M,S}$ [°]	after 1 year	after 2 years
ω_{nom}	-14.4586	-42.1231
ω_{init} - ω_{nom}	30.4586	58.1231
rate per day	0.0834	0.0796

Table 43. Nominal values for the argument of periapsis considering the gravity field of Mercury and the gravity of the Sun

ω [°]	gravity field of Mercury	both effects
σ	0.0932	0.0852
$\omega_{\sigma,min}$	-16.6829	-14.5439
$\omega_{\sigma,max}$	-16.4965	-14.3734
ω_{min}	-16.9181	-14.7587
ω_{max}	-16.1856	-14.0897

Table 44. Values for the argument of periapsis after 1 year

ω [°]	gravity field of Mercury	both effects
σ	0.5311	0.4827
$\omega_{\sigma,min}$	-45.7262	-42.6058
$\omega_{\sigma,max}$	-44.6640	-41.6404
ω_{min}	-47.1725	-43.9248
ω_{max}	-42.8051	-39.9622

Table 45. Values for the argument of periapsis after 2 years

Figure 27 and Figure 28 show the evolution of the inclination and the semi-major axis of MPO considering the gravity field of Mercury (left) and the both perturbing forces (right) respectively. According to the plots, the amplitude of the periodic oscillations in the inclination and in the semi-major axis, taking both effects into account, are slightly larger, but the standard deviation is tinier.

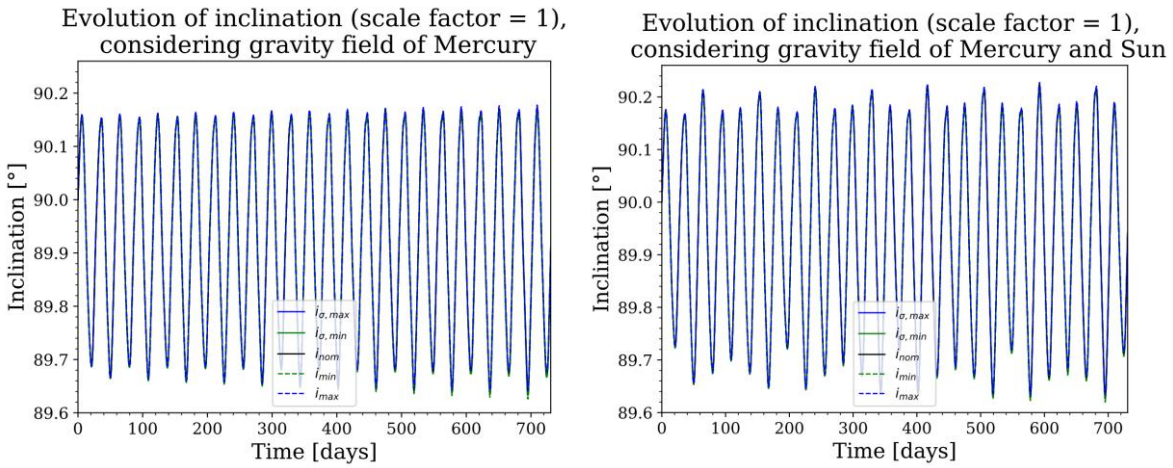

Figure 27. The evolution of the inclination considering gravity field of Mercury over 2 years (left); The evolution of the eccentricity considering the gravity field of Mercury and the Sun as a mass point over 2 years (right)

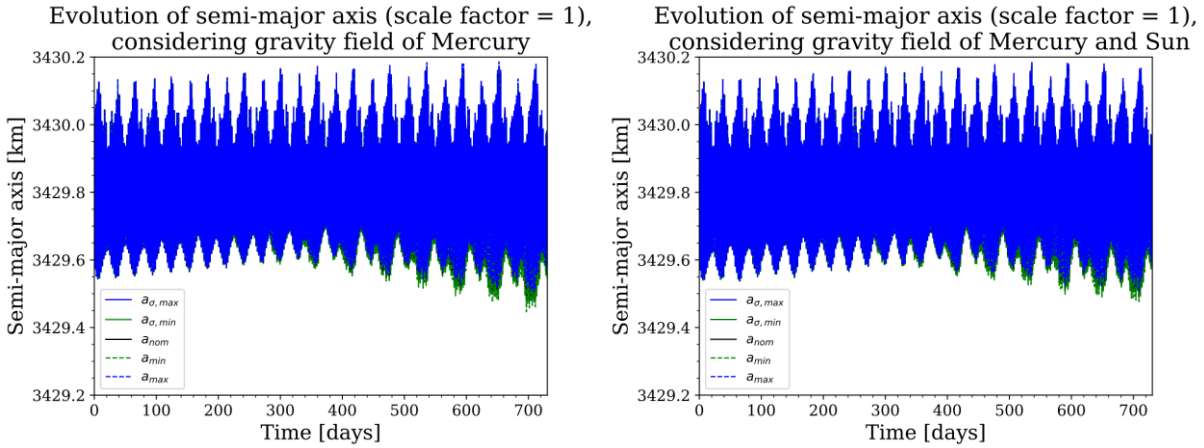

Figure 28. The evolution of the semi-major axis considering gravity field of Mercury over 2 years (left); The evolution of the eccentricity considering the gravity field of Mercury and the Sun as a mass point over 2 years (right)

7.3.2. Radiation pressure and solar system bodies

In addition to the simulations discussed in sections 7.1 and 7.3.1, the simulations based on the gravity fields with the scale factor 1 were performed taken into consideration the radiation pressure and solar system bodies additionally to the geopotential of Mercury and the gravity force of the Sun. The radiation pressure includes SPR, the thermal radiation pressure and the reflected albedo pressure. The solar system bodies are represented by Venus, Earth-Moon, Mars, Jupiter and Saturn (see Figure 12). The number of the simulations was limited to 100 due to the long processing time.

Case	Number of simulations	Scale factor	Consideration of perturbing forces
Case 1	100	1	Gravity field of Mercury
Case 2	100	1	Gravity field of Mercury and gravity of the Sun
Case 3	100	1	Gravity field of Mercury, gravity of the Sun, RP, solar system bodies (shortly: all perturbations)

Table 46. Description of the simulations

Table 46 describes the three analysed cases. The results of these three cases were compared with each other in order to investigate the differences in changes in the orbital elements of MPO. Note

that 100 simulations in each case were taken for the comparison in order to do the analysis legitimately.

The obtained results show that the values of the orbital elements in case 3 are very similar to the values in case 2. The difference in values is very tiny and accounts approximately for 0.1 %. For example, the periherm nominal value in case 3 is smaller by 0.2 km than in case 2 after 2 years. Otherwise, the differences between the values for case 1 and 3 are appreciable. For example, the nominal value of periherm in case 3 is bigger by 25.6 km than in case 1 after 2 years.

Summarizing the results, the simulations show that, it is necessary to take the gravitational potential of Mercury and as well as the gravity force of the Sun into account for the prediction of the orbit evolution of MPO over time, because they cause the major perturbations in the satellite motion. The other considered disturbance forces of case 3 can be neglected due to the very small resulting acceleration. On the other hand, the number of the simulations is too small to do the qualitative analyses. It can only give the primary estimation.

The plots with evolution of the orbital elements and the tables with more detailed information about the values of the orbital elements for these three cases after 1 and 2 years can be found in Appendix.

8. Discussion and conclusion

8.1. Discussion

Within the framework of this bachelor thesis, the simulations for the prediction of the orbital evolution of MPO in the gravity field of Mercury were performed using gravity fields based on the scale factors 1, 3, 5 and 10. The aim of the simulations is the systematically investigation of the consequences of the generated gravity fields of Mercury which lie in the margin of error of the gravitational coefficients. Scale factors are used for conservative consideration of the estimations for the harmonic coefficients. The recommended scale factor is between 10 and 15 [Mazarico et al., 2014]. For this reason, the simulations using the generated gravity fields, based on the scale factors 10 and 15, were executed during the definition of the boundary conditions. The simulations with the scale factor 15 failed most of the time as the Integrator stopped the calculations after short time and reported the error. This was due to some extreme gravity fields which caused the satellite to crash into the planet after short time in the orbit. Although these generated fields could be considered as highly unlikely, they are still a possible solution and lie within the margins for the scale factor 15. For this reason, it was decided to investigate the influence of the gravity fields with the scale factor 1, 3, 5 and 10, and not to include the simulations with the scale factor 15.

The scale factors have a linear effect on the evolution of the elements, as it was shown before. By investigating the scale factors 1, 3, 5 and 10, the effect of a scale factor of 15 can be investigated. In fact, a higher scale factor will lead to a higher probability that the orbit falls below the critical altitude of 200 km or even crashes into the planet.

All gravity fields were generated up to degree and order of 50 although 100x100 gravity fields would have been possible. The degree and order were reduced for two reasons:

Higher terms of the gravity field have only a minor effect on the orbital evolution. The terms with degree and order above 50 have such a small effect, that they are not noticeable in the results. The second reason was to simplify the considered model and to reduce the calculation time significantly.

As shown in section 7.3.1, the gravity field of the Sun as a point-like mass has also appreciable influence on the evolution of the periherm after 2 years. For this reason, the attraction of the Sun had to be included in simulation in order to obtain better and more realistic results.

In addition, the effect of other disturbing forces has been analysed. This includes the solar radiation pressure, the gravitational forces of solar system planets like Venus, Earth, Jupiter etc., and the indirect radiation pressure which includes the thermal radiation pressure and the albedo. All these perturbing forces have only a minor effect on the orbital evolution. Perturbations are caused by the solid tidal forces and propulsive manoeuvres as well as the relativistic perturbations were not considered. A detailed analysis of these forces would go beyond the scope of this bachelor thesis.

In a future work, based on the results of this thesis, it could be studied which kind of orbit correction manoeuvres needs to be performed to maintain the desired altitude of MPO.

8.2. Conclusion

The main acceleration acting on the motion of MPO is caused by the gravity field of Mercury. The performed simulations show that the geopotential of Mercury increases the eccentricity of the orbit which in turn leads to a decrease in the periherm altitude and a rise of the apoherm respectively. The

semi-major axis and the inclination remain almost constant over time but have a periodical character due to the perturbations. The overall trend in the evolution of the longitude of ascending node is a slow decrease with periodic fluctuations because of the motion of the satellite and the planet's rotation. Moreover, the argument of periapsis decreases almost linearly, which is caused by the North-South mass asymmetry and flattening of Mercury.

The standard deviations, as well as the differences between the minimal and maximal values of the orbital elements get larger with growing scale factor and over time. The values of the elements lie in an acceptable range after 1 year while the change, for example, in the periherm after 2 years could be already considered as critical for the scale factor 1, whereas there is a chance of 0.02 % that the periherm falls below 200 km. The likelihood that the periherm lies under the critical value after 2 years increases with the rising scale factor and amounts to 11.74 % for the scale factor 3, to 23.69 % for the scale factor 5 and to 36.21 % for the scale factor 10. Furthermore, the satellite ends up with the collision into the planet in 0.01% of the simulations for the scale factor 5 and in 1.51 % of the simulations for the scale factor 10.

The maximal and minimal values of the orbital elements for the scale factor 10 can be defined as extreme. This might be caused by the extreme gravity fields of Mercury which could exist statistically but the likelihood of them is very tiny.

When considering third-body perturbing force as a point mass additionally to the gravitational potential of Mercury, an attraction of the Sun has a positive effect on the evolution of the periherm, i.e. the gravity force of the Sun reduces the increase in the eccentricity and the decrease of the periherm respectively after 2 years in the orbit. For example, considering the gravity of the Sun and the geopotential of Mercury, the periherm ends up 25.8 km higher than without the attraction of the Sun. Moreover, the minimal value of the periherm doesn't fall below 200 km after 2 years when the gravity of the Sun is taking into account. Considering only the gravity field of Mercury, the minimal value of the periherm falls below this critical value.

Furthermore, "the third-body perturbation makes the orbit to flatten in the direction of the perturbing body. It produces secular effects on the argument of periapsis and the right ascension of the ascending node" [Tresaco et al., 2018], namely both elements fall slower than by considering only the gravitational potential of Mercury. Furthermore, the periodic oscillations in semi-major axis and in inclination are slightly larger than without considering the attraction of the Sun. Moreover, the standard deviation of all orbital elements is tinier when considering both perturbing forces instead of taking only the gravitational potential of Mercury into account.

By consideration of the radiation pressure and the solar system bodies additionally to the geopotential of Mercury and the attraction of the Sun, the results of the simulations show that the evolution of the orbital elements of MPO in this case is similar to the case with the Sun's gravity force. This difference is unappreciable and accounts for ca. 0.1 %, because the radiation pressure and the solar system bodies masses cause only small perturbations on the motion of MPO. For this reason, these disturbing forces can be neglected by the prediction of the orbital evolution of the spacecraft.

The results of the performed simulations of this bachelor thesis are in accordance with the results presented in CREMA in which the gravity field of Mercury, the gravity of the Sun and SRP are taken into account [Khan and Rocchi, 2018]. This thesis expands the results of CREMA and gives additional probabilities on how the orbit will evolve.

Table of acronyms

Acronym	Description
BELA	BepiColombo Laser Altimeter
CREMA	Cornerstone Consolidated Report on Mission Analysis
DLR	Deutsches Zentrum für Luft und Raumfahrt
dlsode	Adam multi-step integration method
dop853	integration method
EPPS	Energetic Particle and Plasma Spectrometer
ESA	European Space Agency
ESOC	European Space Operations Centre
GRNS	Gamma-Ray and Neutron Spectrometer
GSFC	Goddard Space Flight Center
IAUplanet	body-fixed equatorial system
ISA	Italian Spring Accelerometer
ISAS	Institute of Space Astronautical Science
J2000	Earth equator system
JAXA	Japan Aerospace Exploration Agency
MAG	MAGnetometer
MASCS	Mercury Atmospheric and Surface Composition Spectrometer
MDIS	Mercury Dual Imaging System
MercuryIAU	Inertial Mercury equatorial system
MERTIS	MErcury Radiometer and Thermal Infrared Spectrometer
MESSENGER	MErcury Surface, Space ENvironment, GEochemistry, and Ranging
MGNS	Mercury Gamma-ray and Neutron Spectrometer
MIXS	Mercury Imaging X-ray Spectrometer
MJD	Modified Julian Date
MJD	Modified Julian Date
MLA	Mercury Laser Altimeter
MMO	Mercury Magnetospheric Orbiter
MON-3	Mixed Oxides of Nitrogen
MORE	Mercury Orbiter Radio-science Experiment
MOSIF	MMO Sunshield and Interface Structure
MPO	Mercury Planetary Orbiter
MPO-MAG	Mercury Planetary Orbiter MAGnetometer
MTM	Mercury Transfer Module
NASA	National Aeronautics and Space Administration
PDF	probability density function
PDS	Planetary Data System
PHEBUS	Probing of Hermean Exosphere by Ultraviolet Spectroscopy

PlanetIAU	inertial equatorial system
RK4	Runge-Kutta integration method
RKFB	Runge-Kutta-Fehlberg integration method
RP	Radiation pressure
RS	Radio Science
SERENA	Search for Exospheric Refilling and Emitted Natural Abundance
SIMBIO-SYS	Spectrometer and Imagers for MPO BepiColombo Integrated Observatory SYStem
SIXS	Solar Intensity X-ray and particle Spectrometer
SRP	solar radiation pressure
XRS	X-Ray Spectrometer

Table of symbols

Symbol	**Description**	**Unit**
GM	gravitational coefficient	$\frac{km^3}{s^2}$
C_{mn}, S_{nm}	spherical harmonic coefficients	-
a	semi-major axis	km
e	eccentricity	-
i	inclination	°
Ω	the longitude of the ascending node	°
ω	argument of periapsis	°
M	mean anomaly	°
α	right ascension	°
δ	declination	°
σ	standard deviation	-
r_p	periherm	km
μ	nominal value	-
$s_1, s_2, s_3, s_4, s_5, s_6, s_7$	surface areas of the spacecraft	m^2
k	number of concentric rings	-
n_i for i=1,…,k	number of surface segments	-
n_a	number of additional surface segments in the outer rings	-
r_a	apoherm	km
r_M	reference radius of Mercury	km
F	Gravitational force	
m	Mass of the satellite	kg
r	distance between the centres of mass	km
G	universal gravitational constant	$\frac{m^3}{kg \cdot s^2}$
$\ddot{r}$	acceleration	$\frac{km}{s^2}$
$\ddot{r}_{PB}$	acceleration due to gravity forces of bodies	$\frac{km}{s^2}$
$\ddot{r}_{Geop}$	acceleration due to higher terms of the geopotential	$\frac{km}{s^2}$

$\ddot{r}_{RP}$	acceleration due to radiation pressure	$\frac{km}{s^2}$
$\ddot{r}_{Atm}$	acceleration due to atmospheric drag	$\frac{km}{s^2}$
$\ddot{r}_{tilt}$	acceleration due to tilt forces	$\frac{km}{s^2}$
∇U	gradient of gravitational potential	$\frac{km}{s^2}$
U	gravitational potential	$\frac{km^2}{s^2}$
$\rho(s)$	density at some point s	$\frac{kg}{km^3}$
$P_n(u)$	Legendre polynomial of degree n	-
λ, λ'	geographic longitude	km
ϕ, ϕ'	geographic latitude	km
δ_{0m}	Kronecker delta	-
P_{nm}	associated Legendre polynomial of degree n and order m	-
$\bar{C}_{nm}, \bar{S}_{nm}.$	normalized spherical harmonic coefficients	-
v_p	velocity in periherm	$\frac{km}{s}$
v_a	velocity in apoherm	$\frac{km}{s}$
T	orbital period	hours
h_p	periherm altitude	km
h_a	apoherm altitude	km
(x, y, z)	Three dimensional coordinates	km
(v_x, v_y, v_z)	Three-dimensional velocity vector	$\frac{km}{s}$
N	Number of simulations	-
$\bar{x}$	Nominal value	-
x	Value of the data set	-
$r_{p,\sigma,max}$	Maximal value of periherm based on standard deviation	km
$r_{p,\sigma,min}$	Minimal value of periherm based on standard deviation	km
$r_{p,init}$	Initial value of periherm	km
$r_{p,nom}$	Nominal value of periherm	km
$r_{p,min}$	Minimal value of periherm	km
$r_{p,max}$	Maximal value of periherm	km
e_{nom}	Nominal value of eccentricity	-
e_{init}	Initial value of eccentricity	-
$e_{\sigma,min}$	Minimal value of eccentricity based on standard deviation	-
$e_{\sigma,max}$	Maximal value of eccentricity based on standard deviation	-
e_{min}	Minimal value of eccentricity	-
e_{max}	Maximal value of eccentricity	-
$r_{a,nom}$	Nominal value of apoherm	km
$r_{a,init}$	Initial value of apoherm	km
$r_{a,\sigma,min}$	Minimal value of apoherm based on standard deviation	km
$r_{a,\sigma,max}$	Maximal value of apoherm based on standard deviation	km
$r_{a,min}$	Minimal value of apoherm	km
$r_{a,max}$	Maximal value of apoherm	km
ω_{init}	Initial value of argument of periapsis	°
ω_{nom}	Nominal value of argument of periapsis	°
$\omega_{\sigma,min}$	Minimal value of argument of periapsis based on standard	°

	deviation	
$\omega_{\sigma,max}$	Maximal value of argument of periapsis based on standard deviation	°
ω_{min}	Minimal value of argument of periapsis	°
ω_{max}	Maximal value of argument of periapsis	°
$\Omega_{\,init}$	Initial value of longitude of ascending node	°
Ω_{nom}	Nominal value of longitude of ascending node	°
$\Omega_{\sigma,min}$	Minimal value of longitude of ascending node based on standard deviation	°
$\Omega_{\sigma,max}$	Maximal value of longitude of ascending node based on standard deviation	°
Ω_{min}	Minimal value of longitude of ascending node	°
Ω_{max}	Maximal value of longitude of ascending node	°
$\dot{\Omega}$	Change in longitude of ascending node	°/s
$\dot{\omega}$	Change in argument of periapsis	°/s
$\dot{\omega}_{min}$	Minimal value of change in argument of periapsis	°/s
$\dot{\omega}_{max}$	Maximal value of change in argument of periapsis	°/s
$\dot{e}_{min}$	Minimal value of change in eccentricity	1/s
$\dot{e}_{max}$	Maximal value of change in eccentricity	1/s
$\dot{e}$	Change in eccentricity	1/s
p	semi-latus rectus	km
n	mean motion	1/s
R_{planet}	Planet's radius	km
$r_{p,M,S}$	Periherm value based on consideration of the gravity field of Mercury and the gravity of the Sun	km
$e_{M,S}$	Eccentricity value based on consideration of the gravity field of Mercury and the gravity of the Sun	-
$r_{a,M,S}$	Apoherm value based on consideration of the gravity field of Mercury and the gravity of the Sun	km
$\Omega_{M,S}$	Value of longitude of ascending node based on consideration of the gravity field of Mercury and the gravity of the Sun	°
$\omega_{M,S}$	Value of argument of periapsis based on consideration of the gravity field of Mercury and the gravity of the Sun	°
$\Omega_{all\ pert}$	Value of longitude of ascending node based on consideration of all perturbations	°
$\omega_{all\ pert}$	Value of argument of periapsis based on consideration of all perturbations	°
$e_{all\ pert}$	Eccentricity value based on consideration of all perturbations	-

References

Acton C. (2019), The Spice Concept, https://naif.jpl.nasa.gov/naif/spiceconcept.html,

(access date: 27.02.2019).

Archinal B. A., C.H. Acton, M. F. A'Hearn, A. Conrad, G. J. Consolmagno, T. Duxbury, D. Hestroffer, J. L. Hilton, R. L. Kirk, S. A. Klioner, D. McCarthy, K. Meech, J. Oberst, J. Ping, P. K. Seidelmann, D. J. Tholen, P. C. Thomas, I. P. Williams (2018), Report of the IAU Working Group on Cartographic Coordinates and Rotational Elements: 2015, *Celestial Mechanics and Dynamical Astronomy, 130(3), doi: 10.1007/s10569-017-9805-5.*

Bahloul, S. (2013), Effect of planetary thermal radiation and reflected sunlight on spacecraft Trajectories: Application to Mercury and the BepiColombo Mission, *Master Thesis, Technische Universität Berlin.*

Balogh A., R. Grard, S.C. Solomon, R. Schulz, Y. Langevin, Y. Kasaba, M. Fujimoto (2007), Missions to Mercury, *Space Science Reviews 132: 611-645, doi: 10.1007/s11214-007-9212-4.*

Carvalho, J. P. S., J. Cardoso dos Santos, A. F. B. A. Prado, R. Vilhena de Morales, Some characteristics of orbit for a spacecraft around Mercury, *Computational and Applied Mathamatics, doi: 10.1007/s40314-017-0525-y.*

Carvalho, J.P.S. (2017), Analysis of the long and short-period terms due the nonsphericity of the central body: applications for Mercury, *Journal of Physics: Conference Series 911 012011, doi: 10.1088/1742-6596/911/1/012011.*

Damme F. (2011), Nummerische Bahnintegration am Beispiel eines künstlichen Satelliten im Orbit um den Jupitermond Ganymed, *Diplomarbeit, Martin Luther-Universität Halle-Wittenberg*.

European Space Agency (2019d), A pair of planetary explorers at Mercury,

http://sci.esa.int/bepicolombo/59934-spacecraft-duo/, (access date: 28.03.2019).

European Space Agency (2019e), Fact sheet,

http://sci.esa.int/bepicolombo/47346-fact-sheet/, (access date: 28.03.2019).

European Space Agency (2019g), Mercury Planetary Orbiter at Mercury,

http://sci.esa.int/bepicolombo/60077-mercury-planetary-orbiter-at-mercury/,

(access date: 29.03.2019)

European Space Agency (2019f), Mercury Planetary Orbiter – Spacecraft,

http://sci.esa.int/bepicolombo/48872-spacecraft/, (access date: 28.03.2019).

European Space Agency (2019a), Missions to Mercury,

http://sci.esa.int/bepicolombo/56015-missions-to-mercury/, (access date: 28.03.2019).

European Space Agency (2019c), Science with BepiColombo,

http://sci.esa.int/bepicolombo/59928-science-with-bepicolombo/, (access date: 28.03.2019).

European Space Agency (2019b), Summary,

http://sci.esa.int/bepicolombo/33022-summary/, (access date: 28.03.2019).

Fortescue, P., G. Swinerd, J. Stark (2011), Spacecraft system engineering, *4th edition, Chicester: Wiley.*

Genova A., S. Goossens, E. Mazarico, F. G. Lemoine, G. A. Neumann, W. Kuang, T. J. Sabaka, S.A. Hauck II, D. E. Smith, S.C. Solomon, M. T. Zuber (2018), Geodetic evidence that Mercury has a solid inner core, *Geophysical Research Letters, American Geophysical Union.*

Hauck II. S.A., J. L. Margot, S. C. Solomon, R. J. Phillips, C. L- Johnson, F. G. Lemoine, E. Mazarico, T. J. McCoy, S. Padovan, S. J. Peale, M. E. Perry, D. E. Smith, M. T. Zuber (2013), The curios case of Mercury's internal structure, *Journal of Geophysical Research: Planets, vol. 118, doi: 10.1002/jgre.20091.*

Johnson C.L., M. E. Purucker, H. Korth, B. J. Anderson, R. M. Winslow, M. M. H. Al Asad, J. A. Slavin, I. I. Alexeev, R. J. Phillips, M. T. Zuber, S. C. Solomon (2012), MESSENGER observations of Mercury's magnetic field structure, *Journal of Geophysical Research, vol. 117, E00L14, doi: 10.1029/2012JE004217.*

Kato, T., B. Rievers, J. C. van der Ha, C. Laemmerzahl (2012), Sensitivity analysis of the non-gravitational perturbations on a Mercury orbiter, *Advances in the Astronautical Sciences (AAS) 12-208.*

Kaula W.M. (2000), Theory of satellite geodesy: Applications of satellites to geodesy, *DOVER PUBLICATIONS, INC, Mineola, New York.*

Khan, M., A. Rocchi, BepiColombo Mercury Cornerstone Consolidated Report on Mission Analysis, *MAS Working Paper No. 525, BC-ESC-RP-05500, Issue 5.4.*

Ley W., K. Wittmann, W. Hallmann (2011), Handbuch der Raumfahrttechnik, *4., aktualisierte und erw. Aufl., München: Hanser.*

Lüdicke, F. (2008), Simulation der Bahnentwicklung des Mercury Planetary Orbiters (MPO) der Mission BepiColombo unter Berücksichtigung von Störbeschleunigungen und Auswirkungen auf die Datenaufnahme durch das Laser Altimeter BELA, *Diplomarbeit, Technische Universität Berlin.*

Lüdicke, F. (2019), Laseraltimeter BELA,

https://www.dlr.de/pf/desktopdefault.aspx/tabid-6445/10591_read-23854/,

(access date: 28.03.2019).

Margot J. L., S. A. Hauck, II, E. Mazarico, S. Padovan, S. J. Peale (2017), Mercury's internal structure, Mercury – The view after Messenger, S.C. Solomon, B. J. Anderson, L. R. Nittler (editors), *CUP.*

Mazarico E. (2018), GGMES_100V07_SHB,

http://pds-geosciences.wustl.edu/messenger/mess-h-rss_mla-5-sdp-v1/messrs_1001/data/shbdr/ggmes_100v07_shb.lbl/, (access date: 03.04.2019)

Mazarico, E., A. Genova, S. Goossens, F.G. Lemoine, G. A. Neumann, M. T. Zuber, D. E. Smith, S.C. Solomon (2014), The gravity field, orientation, and ephemeris of Mercury from MESSENGER observations after three years in orbit, *Journal of Geophysical Research: Planets, 119*

McNutt R. L., J. S. C. Solomon, P. D. Bedini, E. J. Finnegan, D. G. Grabt, the MESSENGER Team, The Messenger mission: Results from the first two Mercury flybys, *Acta Astronautica 67(2010) 681-687, doi: 10.1016/j.actaastro.2010.05.020.*

Montenbruck, O., E. Gill (2000), Satellite Orbits: Models, Methods, and Applications, *Springer-Verlag, Berlin, Heidelberg, New York.*

Perry M. E., G. A. Neumann, R. J. Phillips, O.S. Barnouin, C. M. Ernst, D. S. Kahan, S.C. Solomon, M. T. Zuber, D. E. Smith, S. A. Hauck II, S. J. Peale, J. L. Margot, E. Mazarico, C. L. Johnson, R. W. Gaskell, J. H. Roberts, R. L. McNutt Jr., J. Oberst (2015), The low-degree shape of Mercury, *Geophysical Research Letters, 42, 6951-6958, doi: 10.1002/2015GL065101.*

Rothery, D.A. (2015), Planet Mercury: From Pale Pink Dot to Dynamic World, *Springer International Publishing Switzerland.*

Schuster A., Jehn R. (2014), Influence of the Mercury gravity filed on the orbit insertion strategy of BepiColombo, *Aerospace Science and Technology 39 (2014) 546-551, doi: 10.1016/j.ast.2014.06.003*.

Seidelmann P.K., B.A. Archinal, M.F. A'hearn, A. Conrad, G.J. Consolmagno, D. Herstroffer, J. L. Hilton, G. A. Krasinsky, G. Neumann, J. Oberst, P. Stooke, E. F. Tedesco, D. J. Tholen, P.C. Thomas, I. P. Williams (2007), Report of the IAU/IAG Working Group on cartographic coordinates and rotational elements: 2006, *Celestial Mechanics and Dynamics Astronomy 98:155-180, doi: 10.1007/s10569-007-9072-y.*

Solomon S. C., R. L. McNutt, J. R. E. Gold, D. L. Domingue (2007), MESSENGER Mission Overview, *Space Science Reviews 131: 3-39, doi: 10.1007/s11214-007-9247-6.*

Stark, A. (2015), Observations of Mercury's rotational state form combined MESSENGER laser altimeter and image data, *Dissertation, Technische Universität Berlin.*

Strom, R.G. (1987), Mercury: The Elusive Planet, Cambridge University Press.

The SciPy community (2019), numpy.random.multivariate_normal,

https://docs.scipy.org/doc/numpy-1.15.1/reference/generated/numpy.random.multivariate_normal.html, (access date: 1.02.2019).

Tresaco, E., J. P. S. Carvalho, A. F. B. A. Prado, A. Elipe, R. Vilhena de Morales (2018), Averaged model to study long-term dynamics of a probe about Mercury, *Celestial Mechanics and Dynamics Astronomy, 130:9, doi: 10.1007/s40314-017-0525-y.*

Verma, A. K., J. L. Margot (2016), Mercury's gravity, tides, and spin from MESSENGER radio science data*, Journal of Geophysical Research: Planets, 121, doi: 10.1002/2016JEDO5037.*

Williams D.R. (2019), Moon Fact Sheet,

https://nssdc.gsfc.nasa.gov/planetary/factsheet/moonfact.html, (access date: 03.04.2019).

Appendix

Appendix 1 – Evolution of the orbital elements *e*, r_a, *a*, *i*, *Ω* and *ω* dependent on degree and order of the gravitational harmonic coefficients

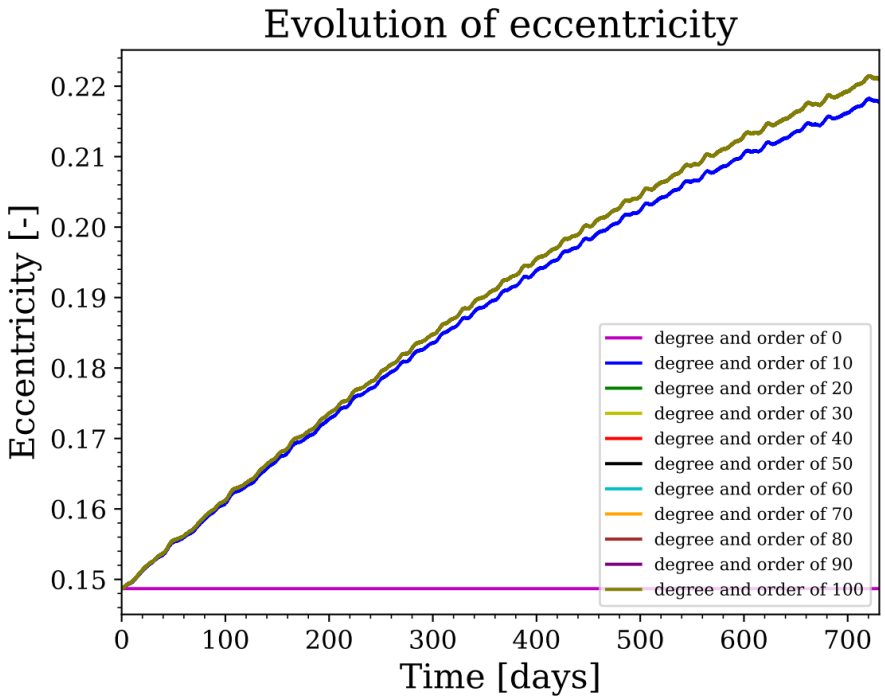

Figure 29. Evolution of the eccentricity dependent on the degree and order of gravitational harmonic coefficients over 2 years

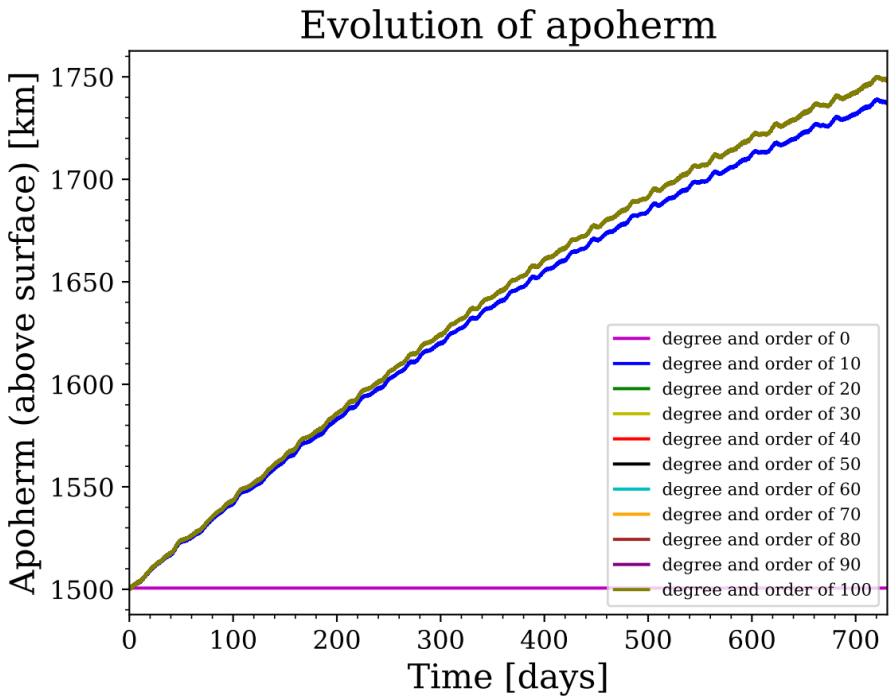

Figure 30. Evolution of the apoherm considering from the Mercury's center dependent on the degree and order of gravitational harmonic coefficients over 2 years

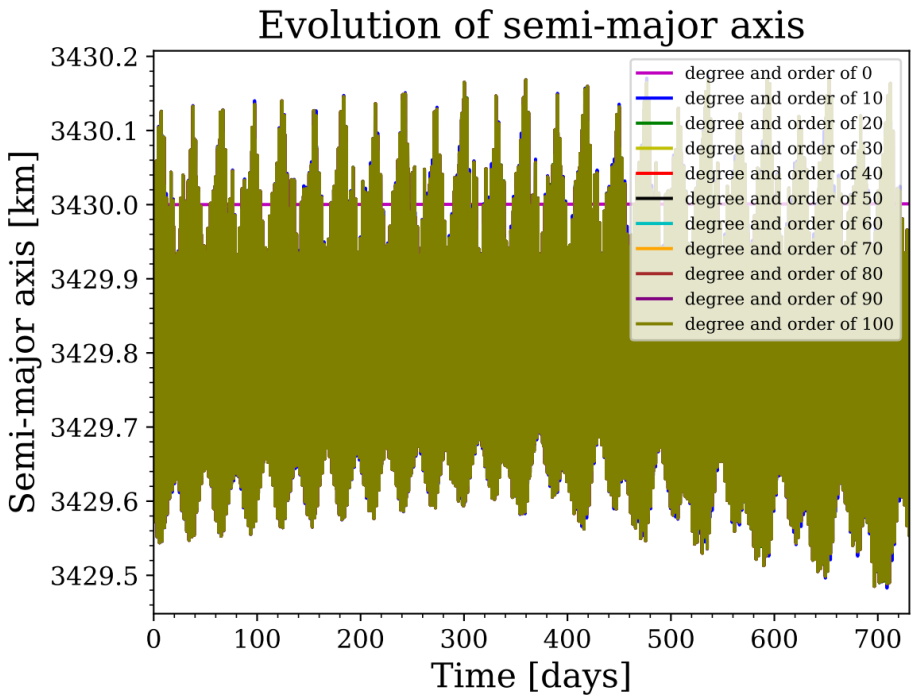

Figure 31. Evolution of the semi-major dependent on the degree and order of gravitational harmonic coefficients over 2 years

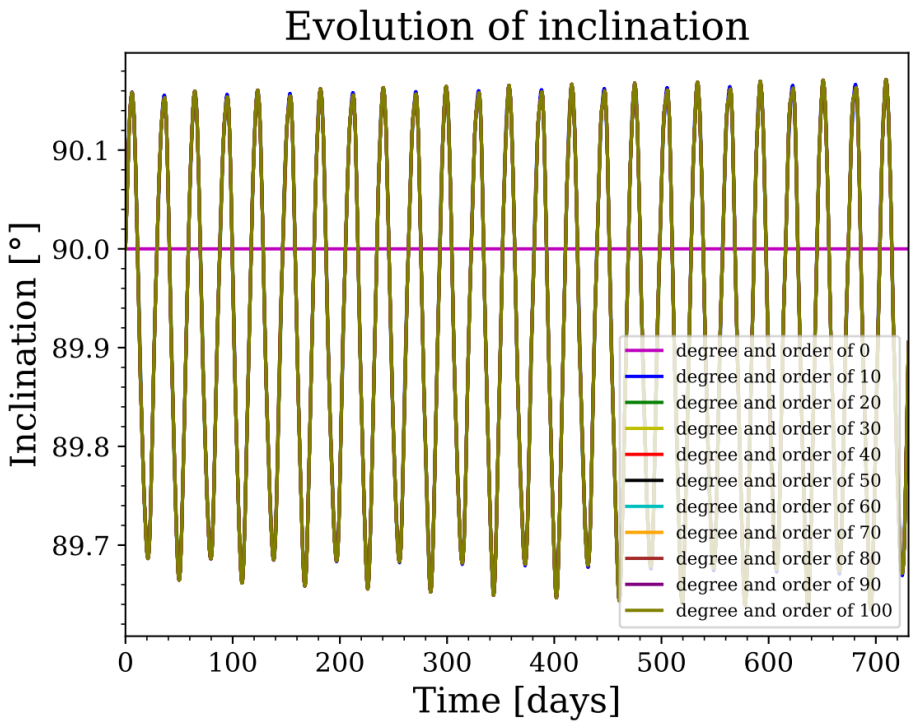

Figure 32. Evolution of the inclination dependent on the degree and order of gravitational harmonic coefficients over 2 years

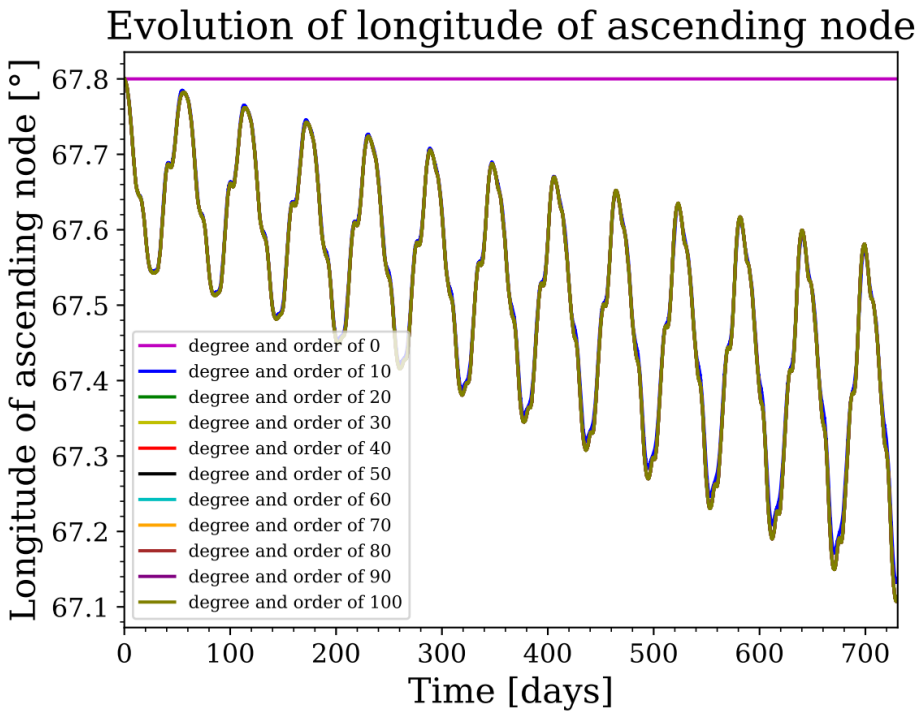

Figure 33. Evolution of the longitude of the ascending node dependent on the degree and order of gravitational harmonic coefficients over 2 years

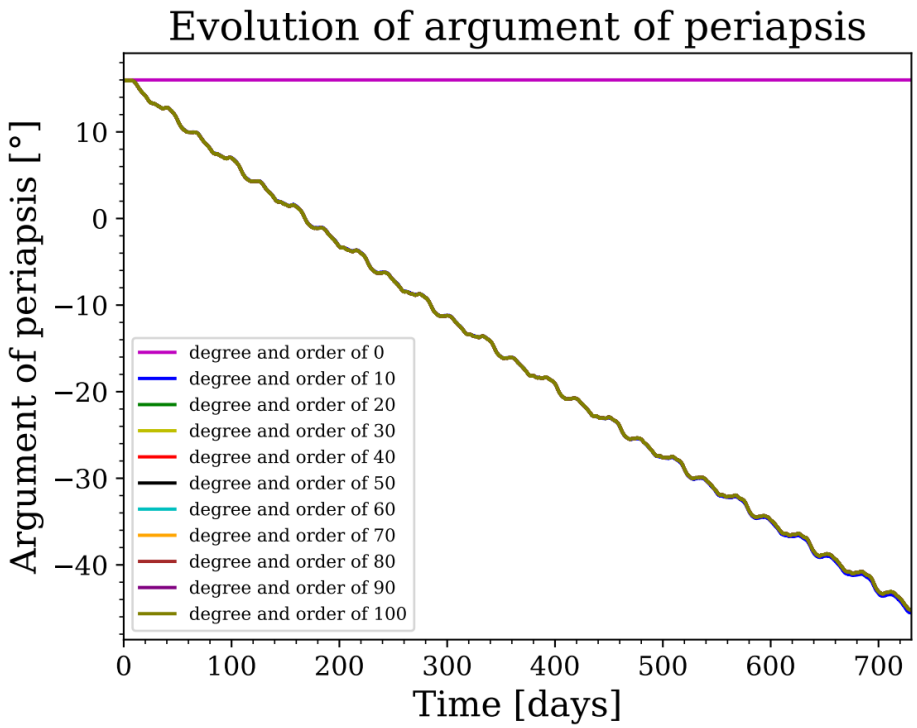

Figure 34. Evolution of the argument of periapsis dependent on the degree and order of gravitational harmonic coefficients over 2 years

Appendix 2 – Box plot for eccentricity of MPO and corresponded table

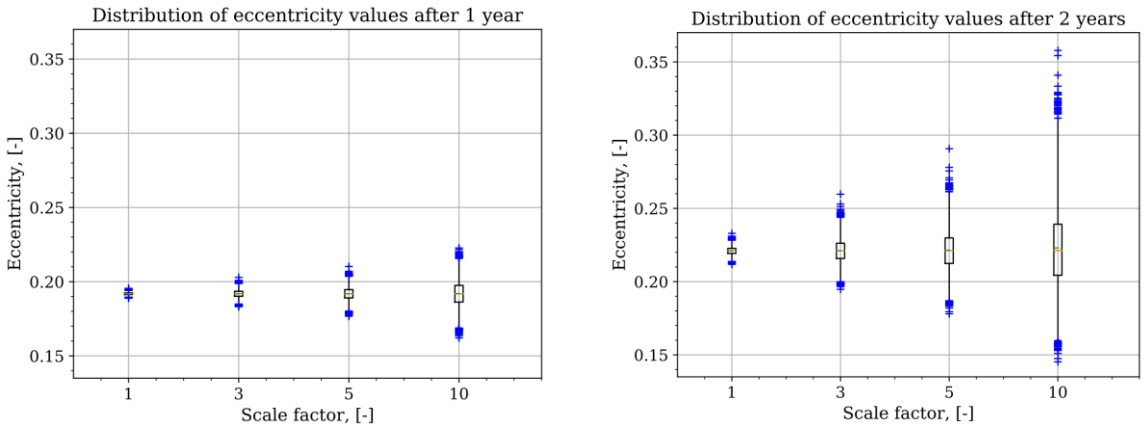

Figure 35. The box plots for the eccentricity after 1 and 2 years

	scale factor 1		scale factor 3		scale factor 5		scale factor 10	
	after 1 year	*after 2 years*	*after 1 year*	*after 2 years*	*after 1 year*	*after 2 years*	*after 1 year*	*after 2 years*
upper outliers	0.195496	0.232966	0.202869	0.2597	0.210266	0.290704	0.222702	0.357820
upper whisker	0.194207	0.228268	0.198937	0.243908	0.203658	0.26134	0.21569	0.311616
upper quartile	0.192418	0.222717	0.193531	0.226222	0.194659	0.229838	0.197495	0.239183
median	0.191868	0.221012	0.191879	0.221058	0.191871	0.221128	0.191891	0.221269
lower quartile	0.191301	0.219241	0.190182	0.215798	0.189052	0.212427	0.186289	0.204319
lower whisker	0.189513	0.213648	0.184854	0.199891	0.180134	0.186976	0.168767	0.159717
lower outliers	0.188929	0.21176	0.183126	0.194729	0.176711	0.178022	0.162107	0.145227

Table 47. The important parameter of the box plot for the eccentricity dependent on the scale factor after 1 and 2 years

Appendix 3 – Box plot for apoherm of MPO and corresponded table

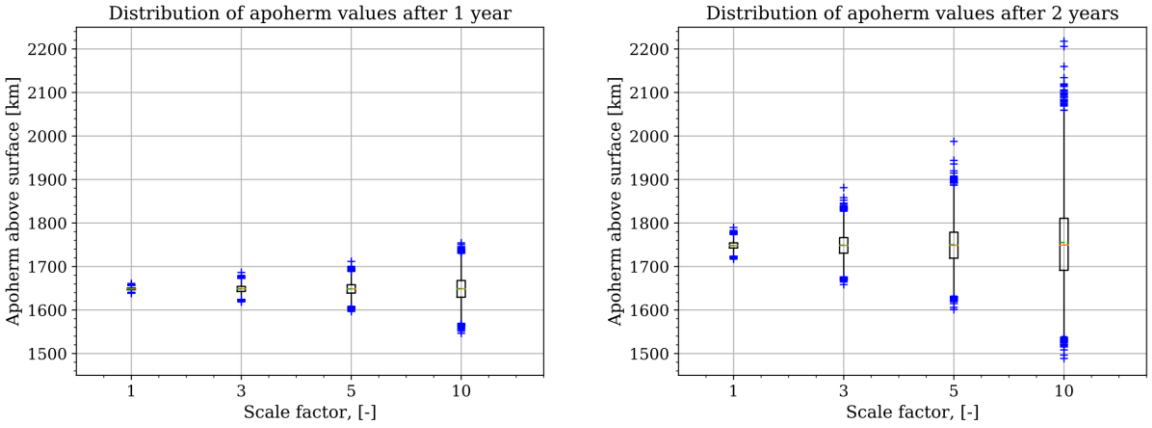

Figure 36. The box plots for the apoherm after 1 and 2 years

	scale factor 1		scale factor 3		scale factor 5		scale factor 10	
	after 1 year	*after 2 years*	*after 1 year*	*after 2 years*	*after 1 year*	*after 2 years*	*after 1 year*	*after 2 years*
upper outliers	1661.021	1789.586	1686.313	1881.278	1711.696	1987.615	1754.321	2217.755
upper whisker	1656.594	1773.474	1672.811	1827.113	1689.0	1886.9	1730.245	2059.325
upper quartile	1650.458	1754.434	1654.272	1766.458	1658.141	1778.861	1667.885	1810.911
median	1648.571	1748.588	1648.606	1748.747	1648.588	1748.984	1648.663	1749.467
lower quartile	1646.629	1742.512	1642.788	1730.705	1638.921	1719.144	1629.443	1691.330
lower whisker	1640.5	1723.33	1624.523	1676.148	1608.316	1631.849	1569.312	1538.354
lower outliers	1638.495	1716.848	1618.592	1658.441	1596.587	1601.137	1546.492	1488.652

Table 48. The important parameter of the box plot for the apoherm dependent on the scale factor after 1 and 2 years

Appendix 4 – Evolution of orbital elements of MPO considering the geopotential of Mercury, additionally gravity force of the Sun and all perturbations

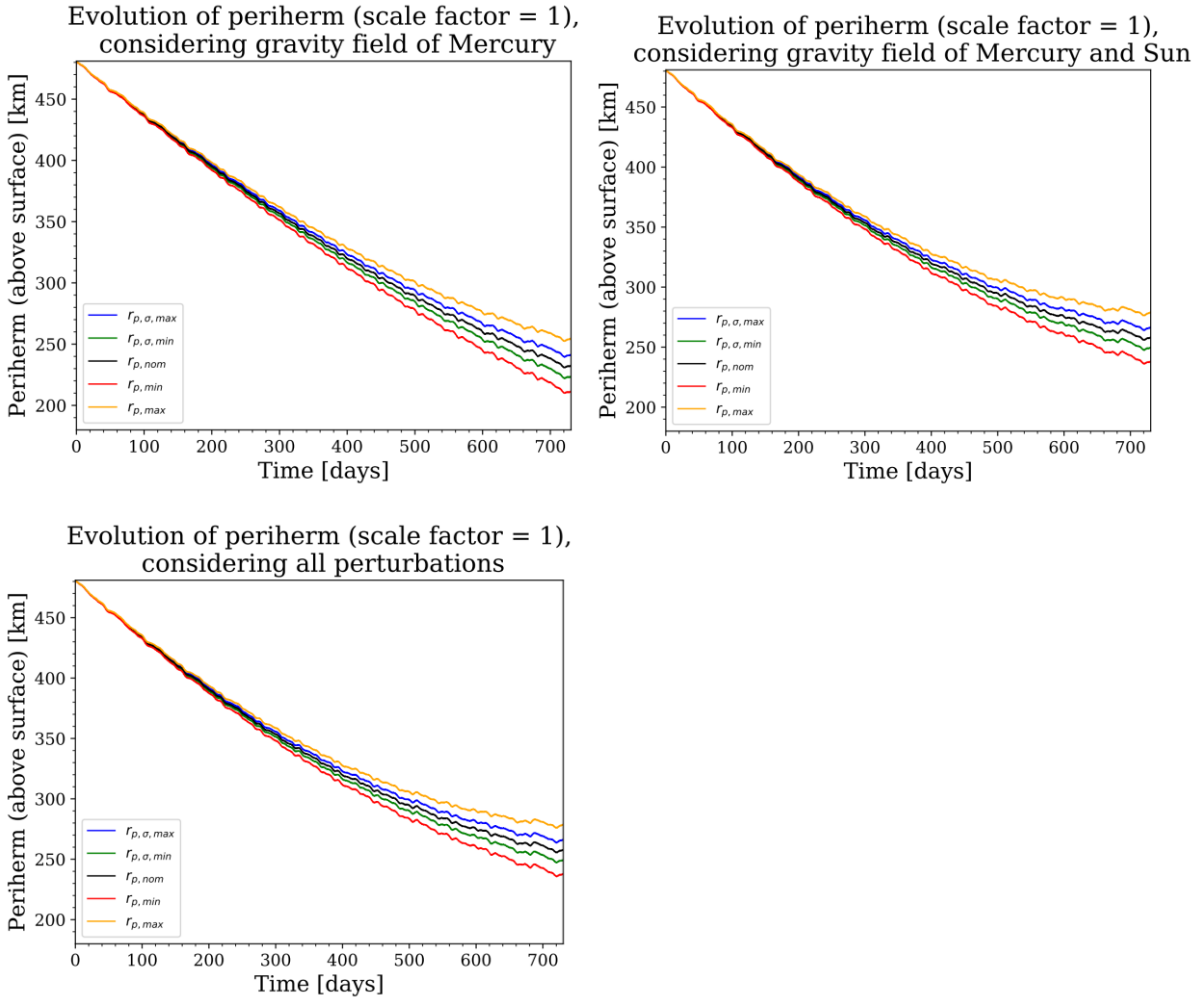

Figure 37. Evolution of the periherm of MPO dependent on the considered perturbing forces

$r_{p,all\ pert}$ [km]	after 1 year	after 2 years
$r_{p,nom}$	331.176	258.107
$r_{p,init}$ - $r_{p,nom}$	149.424	222.493
rate per day	0.409	0.305

Table 49. Nominal values for periherm considering all perturbations

r_p [km]	gravity field of Mercury	gravity field of Mercury and Sun	all perturbations
σ	2.874	2.830	2.828
$r_{p,\sigma,min}$	329.549	328.587	328.348
$r_{p,\sigma,max}$	335.296	334.247	334.004
$r_{p,min}$	325.455	324.543	324.306
$r_{p,max}$	339.456	338.330	338.084

Table 50. Periherm values above surface after 1 year

r_p [km]	gravity field of Mercury	gravity field of Mercury and Sun	all perturbations
σ	8.945	8.446	8.445
$r_{p,\sigma,min}$	223.61	249.861	249.661
$r_{p,\sigma,max}$	241.5	266.753	266.552
$r_{p,min}$	211.477	238.302	238.102
$r_{p,max}$	254.814	279.285	279.085

Table 51. Periherm values above surface after 2 year

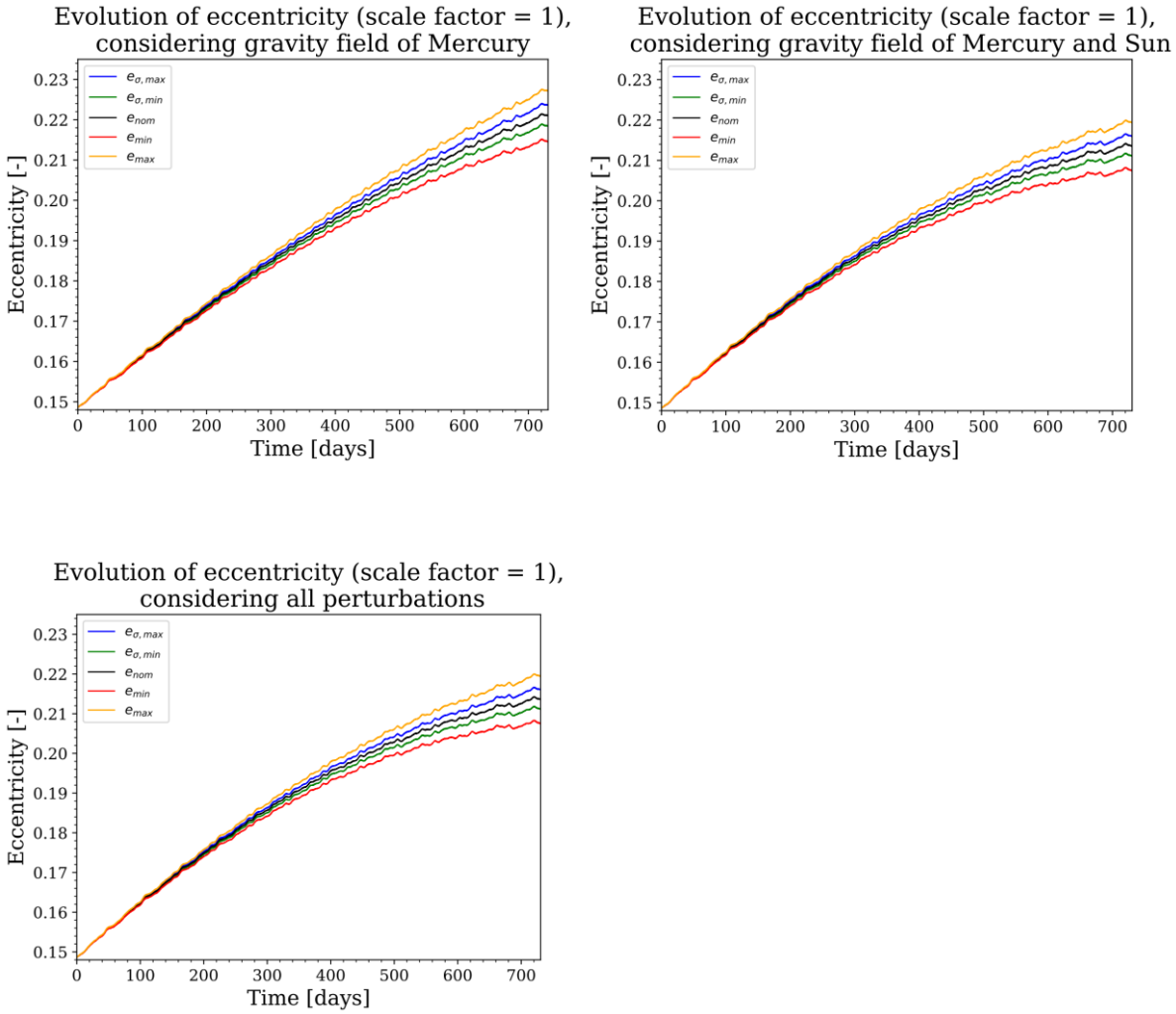

Figure 38. Evolution of the eccentricity of MPO dependent on the considered perturbing forces

$e_{all\ pert}$	after 1 year	after 2 years
e_{nom}	0.1922276	0.2135381
$e_{init} - e_{nom}$	-0.0435396	-0.0648501
rate per day	-0.00011920	-0.0000888

Table 52. Nominal values for eccentricity considering all perturbations

e **[-]**	**gravity field of Mercury**	**gravity field of Mercury and Sun**	**all perturbations**
σ	0.0008378	0.0008251	0.0008246
$e_{\sigma,min}$	0.1910242	0.1913311	0.191403
$e_{\sigma,max}$	0.1926999	0.1929813	0.1930521
e_{min}	0.1898111	0.1901404	0.1902135
e_{max}	0.193893	0.1941601	0.1942305

Table 53. Eccentricity values after 1 year

e **[-]**	**gravity field of Mercury**	**gravity field of Mercury and Sun**	**all perturbations**
σ	0.0026079	0.0024623	0.0024622
$e_{\sigma,min}$	0.2183809	0.2110196	0.211076
$e_{\sigma,max}$	0.2235967	0.2159442	0.2160003
e_{min}	0.2144993	0.2073660	0.2074224
e_{max}	0.2271340	0.2193144	0.2193702

Table 54. Eccentricity values after 2 year

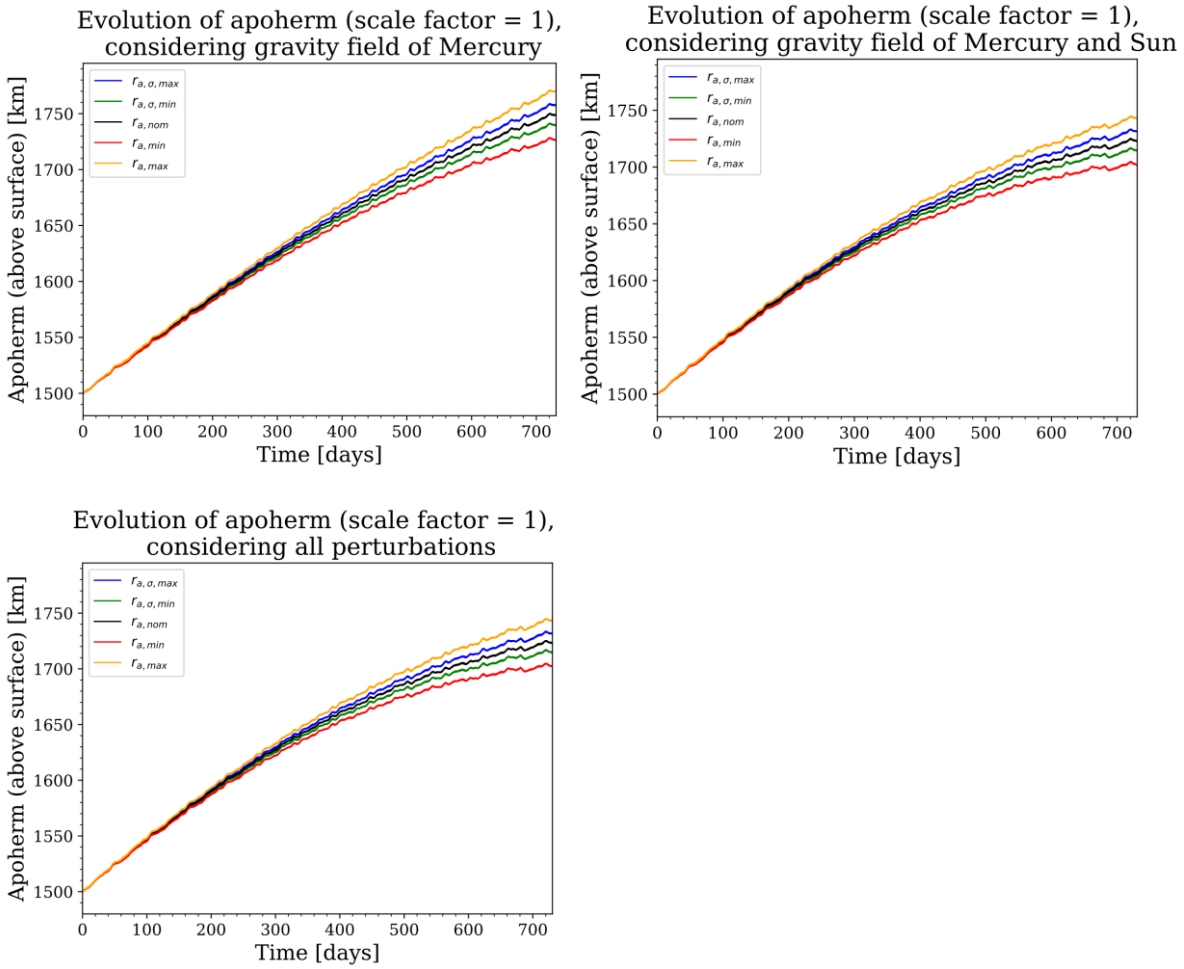

Figure 39. Evolution of the apoherm of MPO dependent on the considered perturbing forces

$r_{a,all\ pert}$ **[km]**	**after 1 year**	**after 2 years**
$r_{a,nom}$	1649.817	1722.947
$r_{a,init}$ - $r_{a,nom}$	-149.217	-222.347
rate per day	-0.409	-0.304

Table 55. Nominal values for apoherm above surface considering all perturbations

r_a [km]	gravity field of Mercury	gravity field of Mercury and Sun	all perturbations
σ	2.874	2.83	2.828
$r_{a,\sigma,min}$	1645.68	1646.737	1646.988
$r_{a,\sigma,max}$	1651.427	1652.397	1652.645
$r_{a,min}$	1641.517	1642.652	1642.909
$r_{a,max}$	1655.516	1656.438	1656.687

Table 56. Apoherm values above surface after 1 year

r_a [km]	gravity field of Mercury	gravity field of Mercury and Sun	all perturbations
σ	8.945	8.445	8.444
$r_{a,\sigma,min}$	1739.563	1714.321	1714.503
$r_{a,\sigma,max}$	1757.452	1731.211	1731.392
$r_{a,min}$	1726.25	1701.79	1701.973
$r_{a,max}$	1769.585	1742.771	1742.95

Table 57. Apoherm values above surface after 2 year

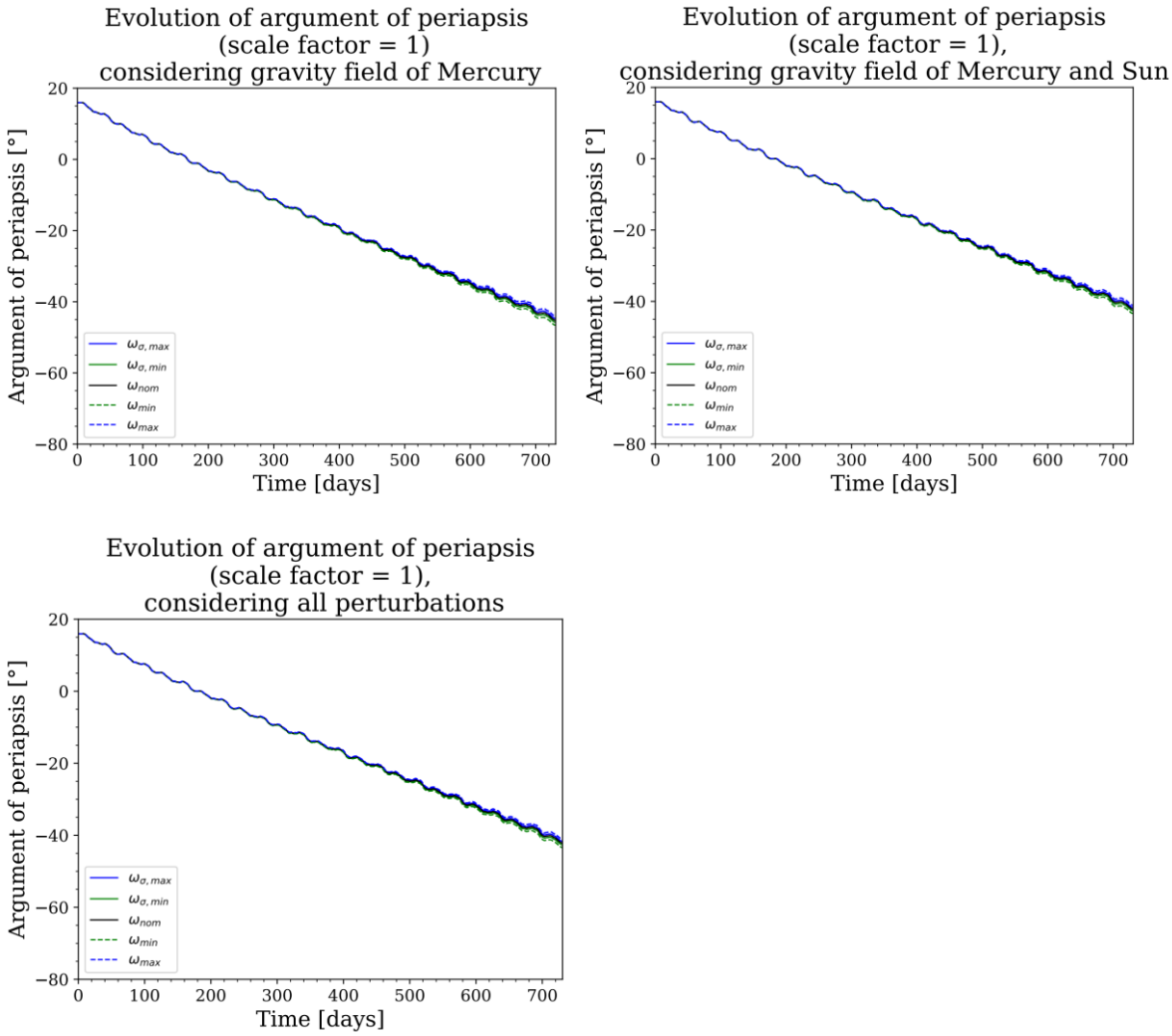

Figure 40. Evolution of the argument of periapsis of MPO dependent on the considered perturbing forces

$\omega_{all\ pert}$ [°]	after 1 year	after 2 years
ω_{nom}	-14.4343	-42.0789
ω_{init} - ω_{nom}	30.4343	58.0789
rate per day	0.08332	0.0795

Table 58. Nominal values for argument of periapsis considering all perturbations

ω [°]	gravity field of Mercury	gravity field of Mercury and Sun	all perturbations
σ	0.0947	0.0867	0.0865
$\omega_{\sigma,min}$	-16.6844	-14.5453	-14.5208
$\omega_{\sigma,max}$	-16.495	-14.3719	-14.3477
ω_{min}	-16.8262	-14.6745	-14.6497
ω_{max}	-16.3692	-14.2563	-14.2323

Table 59. Values for argument of periapsis after 1 year

ω [°]	gravity field of Mercury	gravity field of Mercury and Sun	all perturbations
σ	0.5309	0.483	0.4823
$\omega_{\sigma,min}$	-45.7260	-42.6061	-42.5612
$\omega_{\sigma,max}$	-44.6642	-41.6401	-41.5966
ω_{min}	-46.5742	-43.3738	-43.3279
ω_{max}	-44.0146	-41.0377	-40.9951

Table 60. Values for argument of periapsis after 2 year

$\Omega_{all\ pert}$ [km]	after 1 year	after 2 years
Ω_{nom}	67.5056	67.1486
Ω_{init} - Ω_{nom}	0.2944	0.6514

Table 61. Nominal values for longitude of ascending node considering all perturbations

Ω [km]	gravity field of Mercury	gravity field of Mercury and Sun	all perturbations
σ	0.0037	0.0036	0.0036
$\Omega_{\sigma,min}$	67.4906	67.5045	67.5021
$\Omega_{\sigma,max}$	67.4980	67.5116	67.5092
Ω_{min}	67.4858	67.5	67.4975
Ω_{max}	67.5015	67.5146	67.5122

Table 62. Values for longitude of ascending node after 1 year

Ω [km]	gravity field of Mercury	gravity field of Mercury and Sun	all perturbations
σ	0.0107	0.0097	0.0097
$\Omega_{\sigma,min}$	67.1027	67.1459	67.1389
$\Omega_{\sigma,max}$	67.1241	67.1653	67.1583
Ω_{min}	67.0809	67.1269	67.1199
Ω_{max}	67.1445	67.1839	67.1769

Table 63. Values for longitude of ascending node after 2 year

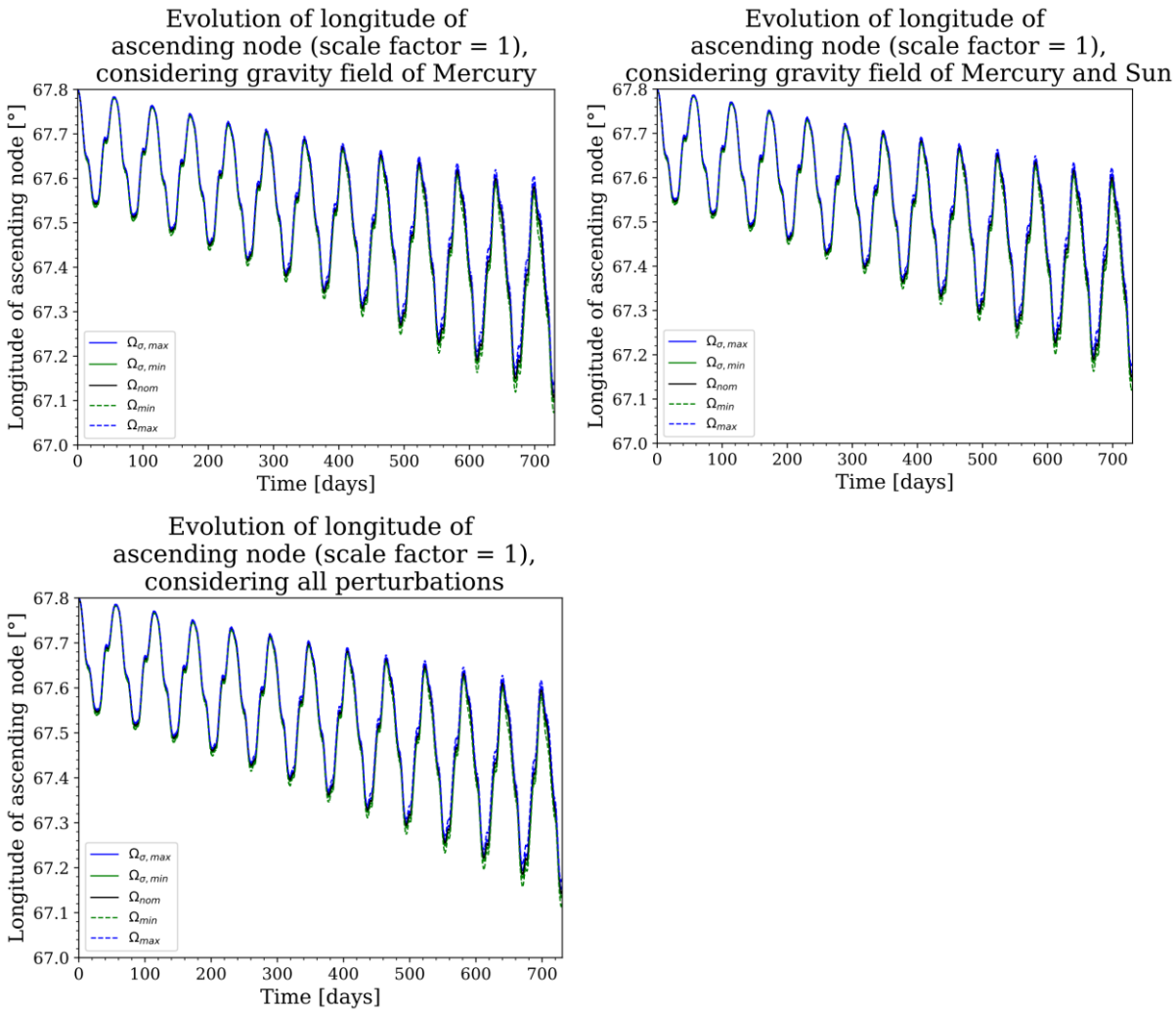

Figure 41. Evolution of the longitude of ascending node dependent on the considered perturbing forces

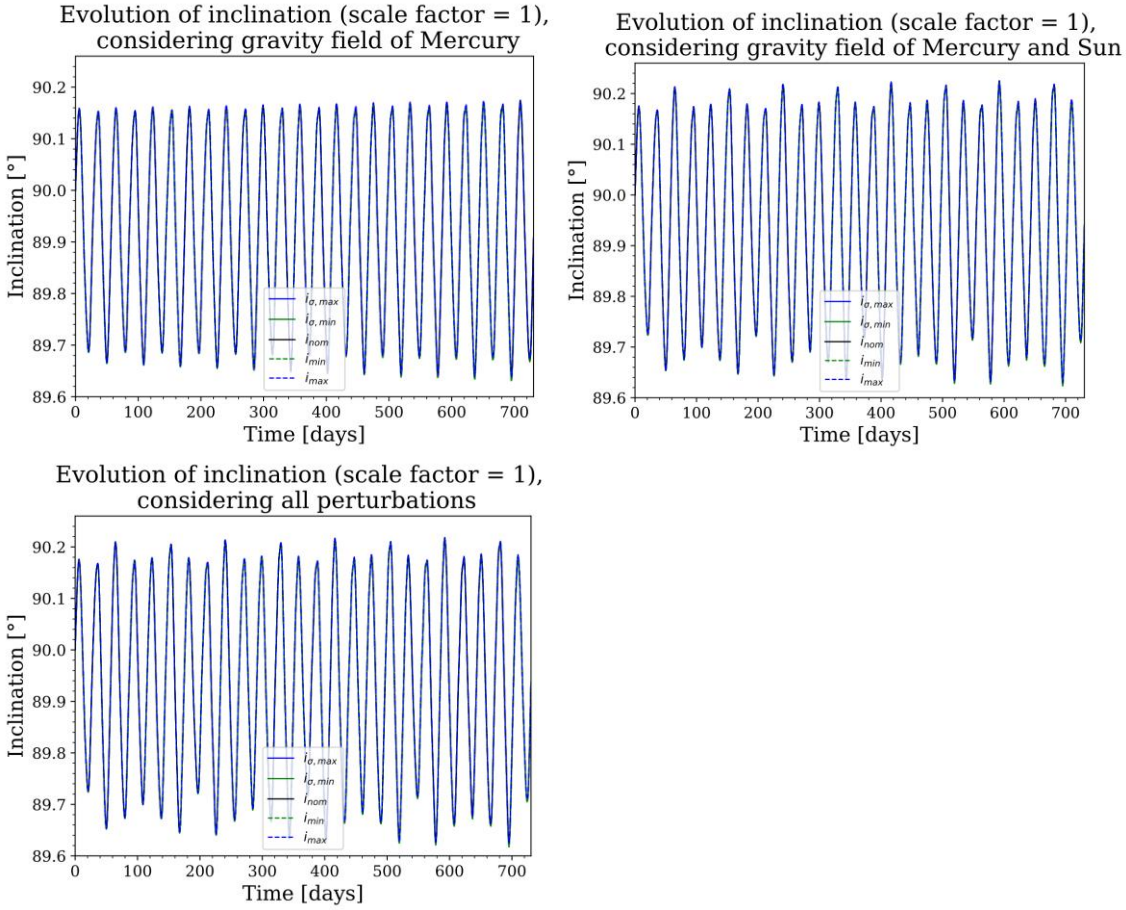

Figure 42. Evolution of the inclination of MPO dependent on the considered perturbing forces

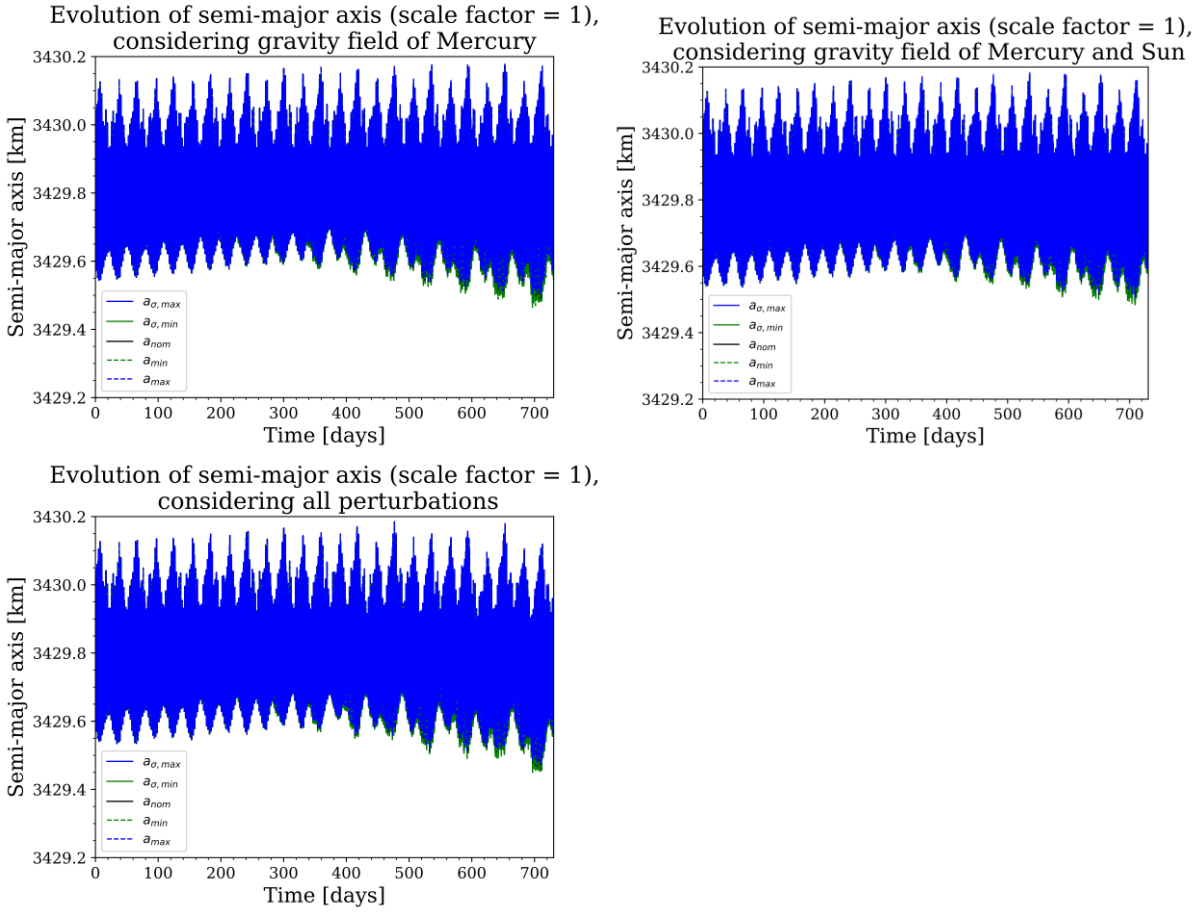

Figure 43. Evolution of the semi-major axis of MPO dependent on the considered perturbing force